

X-RAY STUDIES OF HOT ELECTRONS
IN THERMAL BARRIER OF GAMMA 10

MAFUMI HIRATA



X-ray Studies of Hot Electrons
in Thermal Barrier of GAMMA 10

by

Mafumi Hirata

Submitted in partial fulfillment of the requirements
for the degree of Doctor of Science in Doctoral
Program in University of Tsukuba

1990

Abstract

Tandem mirror devices are characterized by their drastically-improved plasma confinement properties due to electrostatic potential formation. In particular, thermal barrier potentials, ϕ_b , which are designed to reduce the electron heat flow between the central cell and the plug region, play a critical role in the efficient formation of ion confining potentials, ϕ_c . Together with direct observations of these potentials, detailed plasma parameter studies in these regions are of great importance. Using these investigated results, the studies of the production mechanism of the hot electrons as well as their effects on the plasma parameters in the central cell and the plug region are critical issues to be clarified, since there are almost no published experimental data on them.

In this thesis, the following investigations are made particularly by using various soft X-ray diagnostic techniques including X-ray energy pulse height analyses (PHA), X-ray absorption methods as well as X-ray tomographic reconstructions.

(1) The plasma parameters of hot electrons in the barrier region are studied temporally and spatially. Saturation of the hot electron temperature and a successive increase in the hot electron density are observed; these are desirable for creating a thermal barrier potential and for maintaining MHD stability. The temperature saturation is explained in terms of the wave-particle resonance

condition and the trajectory of the electron bounce motion using a new presentation method in the plane of electron pitch angle, θ , vs the magnetic field intensity, B . This representation explains the electron cyclotron heating (ECH) process, corrected for the effects of the relativistic mass variation and the Doppler shift. Also, an application of this representation for investigating the axial profile of soft X-rays clarifies the hot electron production mechanism using graphic display methods in this θ vs B -plane for solving the higher harmonic ECH conditions including the above-mentioned relativistic effects and the Doppler shift.

(2) The next issue is to clarify the thermal isolation effects due to the thermal barrier potential formation.

(a) For the central cell electron temperature, T_{ec} , its temporal and spatial increase has been observed for the first time during the thermal barrier period with $\phi_b/T_{ec} \geq (2-3)$ alone. This shows the improvement of the electron confinement due to the thermal barriers.

(b) For the plug electrons, clearly higher energies as compared with those for the central cell electrons are observed; this result along with (a) indicates the first clear observation of thermal isolation effect due to a kV-range thermal barrier formation. Here, it is noted that the plug electron distribution function is observed to be in a plateau shape; this shape is consistently explained by the height of an electrostatic plug electron confining potential, ϕ_{pb} ($= \phi_b + \phi_c$). This finding supports the result

predicted by Cohen's scaling theory in the strong ECH limit, as observed by the potential measurements.

(3) The above-described new findings have to be made using precisely calibrated data for the detectors. In this thesis, new detector efficiency data are represented for microchannel plates using synchrotron radiation ranging from 0.06 to 0.6 keV, as well as for silicon surface barrier detectors in the 0.06 to 0.9 keV region; these data are used for obtaining the above-described information of bulk electrons in the central cell and in the plug region.

Contents

Chapter 1. Introduction	1
Chapter 2. Theories	5
2-1 Tandem Mirror Plasma Confinement using Electrostatic Potentials	5
2-2 X-ray Radiation from Plasmas	8
Chapter 3. Experimental Apparatus	10
3-1 GAMMA 10	10
3-2 X-ray Detectors	12
3-2-1 Pulse Height Analysers	12
3-2-2 The X-ray Absorption Method	14
3-2-3 X-ray Imaging Systems	16
Chapter 4. Hot Electron Production in the Barrier Region	20
4-1 Experimental Results	20
4-1-1 Typical Data Set	20
4-1-2 Dependence of the Plasma Parameters on Various Operating Conditions	24
4-2 Physical Mechanism Studies of the Hot Electron Production Conditions	29
4-2-1 Electron Cyclotron Heating (ECH)	29
4-2-2 Heating Processes and T_e -Saturation Mechanism	31
4-2-3 Comparison between a New-Representation Method of ECH ($\theta - \Omega_e / \omega$ plane) and the Conventional Method Using Momentum Space	42

Chapter 5. Researches of MCP and SSB Detector Energy Response Using Synchrotron Radiations for Plasma Diagnostics	48
5-1 MCP Energy Response	52
5-2 SSB Energy Response	57
Chapter 6. Observation of the Thermal Barrier Effects on the Central Cell and Plug Electrons Using the X-ray Detectors	61
6-1 Observation of Thermally-Isolated Electron Distribution Functions in the Central Cell and the Plug Region due to the Thermal Barrier	61
6-2 Improvement of the Central Cell Electron Confinement due to the Thermal Barriers	68
Chapter 7. Summary	72
Acknowledgments	76
References	77
Figure Captions	81
Figures	94

Chapter 1. Introduction

Recently, electron cyclotron heating (ECH) has been applied to various types of plasma confinement devices.¹⁻¹³ Microwave plasma production near the electron cyclotron resonance (ECR, $\omega = \Omega_e$) has been used in stellarators and heliotrons,³ and for preionization of discharges in tokamaks.^{4,5} ECH-produced high-energy (hot) electrons play an important role as resonant particles in radio frequency (rf) current start-up without ohmic heating^{6,7} as well as for ECH current drive⁸ in tokamaks. For an ion confining potential formation, rf is also utilized in mirror devices.⁹ In tandem mirror devices, hot electrons produced by ECH at $\omega = 2\Omega_e$ contribute to the thermal barrier potential, ϕ_b , formation,¹⁰⁻¹² which aims to reducing the electron heat flow between the central cell and the plug region; also, the ion confining potential, ϕ_i , is formed by efficient local heating of plug electrons with ECH at $\omega = \Omega_e$.^{10,13}

In the first part of this thesis, the data characteristic of the ECH-produced plasma in the barrier region of the axisymmetrized tandem mirror GAMMA 10 and its production mechanism are discussed in terms of wave particle resonance conditions and trajectories of electron bounce motions in the θ vs Ω_e/ω plane. Here, θ is the pitch angle of an electron orbit. From an application viewpoint, a more general and detailed description of the θ vs Ω_e/ω plane is given. This explanation will be

useful for its application to the ECH mechanism studies in the various types of devices described above.

It is noteworthy that a recent paper on ECH in tokamaks predicts its heating effect, where a collimated microwave lobe is used (thereby producing a narrow spectrum of a parallel refractive index, N_{\parallel}).¹⁴ In contrast to ECH using a cavity mode with various values of N_{\parallel} , ECH with such a narrow N_{\parallel} spectrum leads to quite different experimental results; these aspects are discussed in this paper. Also, a recent theoretical paper on ECH current drive in tokamaks discusses harmonic overlap of the resonance conditions due to relativistic mass variation of hot electrons;¹⁵ this effect is also included in this paper so as to investigate the harmonic overlap mechanism from the viewpoint of the relativistic effect and the Doppler shift. The description of the resonance condition in the θ vs Ω_e/ω plane may be useful for applying ECH in various types of devices as well as for analysing and interpreting the ECH effects physically.

In the next part of the thesis is spent the description of the first calibration experimental data on the microchannel plates (MCPs) in the bulk electron temperature range (0.06-0.6 keV) for the use of X-ray spatial distribution observations. In particular, the X-ray axial profile in the barrier region gives information on the ECH mechanism studies as described above. Also, the dependence of the MCPs on incident photon energies as well as its incident angles is essential for analysing precise

electron temperature, T_e , and density, n_e . Therefore, such basic and quite important researches on the detector characteristics are described.

In the final part of the thesis is investigated the effect of the thermal barrier on the thermal isolation between the central cell and the plug region. In this research, these detailed calibration data on the MCPs are utilized for obtaining a T_e -profile in each region using a method of an X-ray tomographic reconstructions.¹⁶⁻¹⁸ These data are compared with plasma potential profiles, and hence, the relation between T_e and the potentials.

A theoretical research into the physical mechanism of ϕ_c formation has been reported by Cohen et al.^{19, 20} Recently, the scaling law of ϕ_c vs ϕ_b , which is one of the most important and critical issues in the future development and in the design of thermal barrier tandem mirrors, has been reported experimentally.¹³ The theoretical basis for this scaling law is set forth in the above-mentioned papers Cohen et al. These theories for the ϕ_c vs ϕ_b scalings are described in terms of the weak and the strong ECH theories. The difference between the two is based on the competition between the electron acceleration due to ECH and electron collisions. These reflected the final formation of the electron distribution function for the plug electrons; that is, a plateau-distribution-function formation in the strong ECH theory and a Maxwellian distribution-formation in the weak ECH theory.

Under the above-described thermal isolation condition

due to the thermal barrier, such a plug electron distribution function is investigated. Reports of the thermal barrier effects on the central cell electrons have been limited within few preliminary results; in particular, there are no papers on the temporal and spatial (radial position) information on the central cell temperature during the period of the formation of thermal barrier in hundreds volts.

In this paper, the first observation of both temporal and spatial electron temperature increase in the central cell due to the thermal barrier formation is reported; this would demonstrate the usefulness of the thermal barrier not only for the ϕ_e -enhancement but also for the improved electron confinement.

Chapter 2. Theories

2-1 Tandem Mirror Plasma Confinement using Electrostatic Potentials

The concept of tandem mirrors was proposed by Dimov et al.,²¹ in 1976 and by Fowler and Logan²² in 1977. Its essential point adding to simple mirror devices is the plugging of axial particle loss by using positive electrostatic potentials produced by high density mirror-confined plasmas in the plug regions.²³

For a uniform T_e , the value of ϕ_c is predicted by the Boltzmann relation as

$$\phi_c = T_e \ln(n_p/n_c) \quad (2-1),$$

where n_p and n_c are the densities at plug and in central cell, respectively. Axial ion confinement time τ_c can be approximated by Pastukhov's confinement time,^{19, 24}

$$\tau_c = \tau_{ii} g(R) \frac{\phi_c}{T_i} \exp \frac{\phi_c}{T_i} \quad (2-2),$$

$$g(R) = \frac{\sqrt{\pi} (R+1)}{2R} \ln(2R+2),$$

where R is mirror ratio of the plug region to the central cell, T_i is central cell ion temperature and τ_{ii} is ion-ion Coulomb collision time.

To achieve a strong ion plugging, the density ratio n_p/n_c requires a large value because ϕ_c depends on n_p/n_c weakly. In this conventional tandem mirror, a large amount of heating power is required to create the confinement

potential for a reactor.

A thermal barrier is an electrostatic potential dip to provide a thermal isolation between the central cell and the plug cell; it was proposed by Baldwin et al. in 1979.²⁵ Due to the thermal isolation, it can reduce not only the required power to produce plug potentials but also the density ratio n_p/n_c .

In the thermal barrier configuration, Cohen has derived ϕ_c in a modified Maxwell-Boltzmann relation¹⁹ as

$$\phi_c \doteq T_{ep} \ln\left\{\frac{n_p}{n_b}\left(\frac{T_{ec}}{T_{ep}}\right)^{1/2}\right\} - T_{ec} \ln\left\{\frac{n_c}{n_b}\right\} \quad (2-3),$$

where T_{ec} and T_{ep} are the electron temperatures in the central cell and in the plug region: n_b is the electron density in the barrier region.

In GAMMA 10, TMX-U^{26, 27} and TARA²⁸, the thermal barriers are created by mirror-trapped hot electrons produced by second harmonic ECH and sloshing neutral beam injection (NBI). When hot electrons are magnetically trapped in the barrier region, the population of collisional electrons that obeys the Boltzmann relation is reduced. Thus, the term of n_b in eq. (2-3) is replaced by $n_b - n_{bh}$, where n_{bh} is the mirror-trapped hot electron density.

In the case where low energy mirror trapped electrons can be approximated by bi-Maxwellian, the following formula for ϕ_b is obtained with a Fokker-Planck simulation,²⁹

$$\phi_b = T_{ec} \ln\{1.8n_c/(n_b - n_{bh})\} \quad (2-4).$$

This expression is valid for rather low ϕ_b -cases in the

GAMMA 10 experiments.¹⁰ Under the thermal barrier tandem mirror configuration, the scaling study between ϕ_c and ϕ_b is one of the most important issue for future development of tandem mirrors. This theoretically predicted relation was made by Cohen et al. in terms of the following weak ECH and the strong ECH theories:

(i) In the strong ECH case,²⁰ the distribution function of the plug electrons, f_p , tends to become a plateau shape in the perpendicular velocity component with respect to the magnetic field; this is based on much shorter heating time compared with the collision time. As a result, the relation of ϕ_c vs ϕ_b is written as

$$\phi_c = T_{ec} \left(\frac{0.665n_p}{n_c} \exp\left(\frac{1.19\phi_b}{T_{ec}}\right) \right)^{2/3} - \phi_b \quad (2-5).$$

(ii) On the other hand, in the weak ECH case,^{19, 30} f_p becomes Maxwellian due to collisions, and the relation is

$$\phi_c = T_{cp} \left(\ln\left\{ \left(\frac{T_{ec}}{T_{cp}}\right)^{1/2} \frac{n_p}{n_c} \right\} + \frac{\phi_b}{T_{ec}} \right) - \phi_b \quad (2-6),$$

where the magnetic field configuration with a mirror ratio of 0.5 for the plug region to the barrier midplane of GAMMA 10 is taken into account.³⁰

In view of different scalings on ϕ_c vs ϕ_b , it is of great importance to identify the electron distribution function directly from X-ray diagnostics along with the potential observations of ϕ_c and ϕ_b .

2-2 X-ray Radiation from Plasmas

An X-ray diagnostic is one of the most important methods to investigate high temperature plasmas. X-ray radiation, which arises from bremsstrahlung, recombination, line radiation and two photons decay, gives information on electron density, electron temperature, fraction of impurity abundance and other properties.³¹⁻³⁴

Bremsstrahlung arises from Coulomb scattering of free electron with ions.³⁵⁻³⁸ When the electron velocity distribution function is Maxwellian and ions of charge and density are Z_i and n_i , respectively, X-ray emissivity per unit volume and unit energy interval, as a function of photon energy k' is

$$\frac{dI_{ff}(k')}{dk'} \propto \frac{n_e}{\sqrt{kT_e}} \exp\left(-\frac{k'}{kT_e}\right) \sum_i n_i Z_i^2 g_{ff} \quad (2-7),$$

where k is Boltzmann constant and g_{ff} is the free-free Gaunt factor.

Recombination radiation is emitted when a free electron is trapped by an ion into a shell of principal quantum number n . The X-ray intensity by recombination radiation for Maxwellian electrons is given by

$$\frac{dI_{rb}(k')}{dk'} \propto \frac{n_e}{\sqrt{kT_e}} \sum_i \sum_{\substack{n \\ (E_n < k')}} n_i Z_i^2 \frac{2E_n}{nkT_e} \exp\left(\frac{E_n - k'}{kT_e}\right) g_{rb} \quad (2-8),$$

where E_n is the electron binding energy at the shell of n and g_{rb} is the free-bound Gaunt factor.

The line intensity from level l to m is given as

$$J_{lm} = n(l)A_{lm} \quad (2-9),$$

where $n(l)$ is population density of level l , which is calculated from excitation and recombination rates, and A_{lm} is radiative transition probability from level l to m .

Two Photons are emitted with a continuous spectrum from metastable 2S state of hydrogenic and helium-like ions. The X-ray intensity can be written as

$$\frac{dI_{2\gamma}(k')}{dk'} \propto P(2S-1S) \frac{k'^2 (E_T - k')}{E_T^3} \quad (2-10),$$

where E_T is the energy difference between 2S and 1S states and $P(2S-1S)$ is the photon emission rate in the two photon processes.

By summation over eqs. (2-7)-(2-10), total X-ray intensity $dI(k')/dk'$ is calculated.

Chapter 3. Experimental Apparatus

3-1 GAMMA 10

GAMMA 10 is a minimum-B anchored tandem mirror with outboard plug/barrier cells (Fig. 3-1); it has an axial length of 27.1 m and the total volume of the stainless steel vessel is 150 m³. The central cell has an axial length of 6 m and a stainless steel limiter of 36 cm in diameter; the magnetic field intensity at the midplane, B_m , is typically 0.405 T, and its mirror ratio, R_m , is 5.2. The anchor cells are the minimum-B mirrors produced by baseball coils and provide a magnetohydrodynamic (MHD) stability of GAMMA 10, ($B_m = 0.61$ T, $R_m = 3.3$). The plug/barrier cells are axisymmetric mirrors; they have a diameter of 1.5 m and the axial length of 2.5 m, ($B_m = 0.497$ T, $R_m = 6.2$). The base pressure is less than 5×10^{-8} torr; it is maintained by turbomolecular pumps (three pumps with $2.5 \text{ m}^3 \cdot \text{s}^{-1}$ and three pumps with $1.5 \text{ m}^3 \cdot \text{s}^{-1}$) and cryopumps (two pumps with $10 \text{ m}^3 \cdot \text{s}^{-1}$) in the plug/barrier cells as well as by helium cryopanel (two panels for anchor NBI injector tanks with $400 \text{ m}^3 \cdot \text{s}^{-1}$ and two panels for end-mirror tanks with $900 \text{ m}^3 \cdot \text{s}^{-1}$).

At each end of GAMMA 10, radially and azimuthally insulated segmented end plates are installed with resistors of 1 M Ω to ground.

Heating systems are as follows:

A magneto-plasma-dynamic (MPD) gun at each end initiates

the plasma. The neutral beams, which have a 20 kV, 60 A drain at an injection angle of 41° and a 35 kV, 70 A drain at 75° , produce sloshing ions in the plug/barrier cells (sloshing NBI) and hot ions in the anchor cells to improve MHD stability (anchor NBI). Ion cyclotron waves (ICH, 6.2 MHz, 100 kW) are employed to maintain and heat the plasma in the central cell; slow waves are excited by two double half turn antennas with Faraday shield, and are cyclotron-damped at the magnetic beach located near the central cell midplane.

The hot electrons in the barrier region are produced by microwaves generated by a pulsed gyrotron of frequency $\omega/2\pi = 28$ GHz and power $P_{ECH} \leq 140$ kW. The microwaves are transmitted through oversized circular waveguides in the TE_{02} mode; using a Vlasov-Nakajima reflector antenna, this mode is converted to the extraordinary mode (X-mode), and finally injected into the barrier region.^{11, 12} These collimated waves have $N_{\parallel} \approx 0.6$ and FWHM $\approx 11^\circ$. The incident microwave power is located in the region between $B = 0.5$ T and 0.55 T, and is cyclotron-damped at the second harmonic (barrier-ECH) (Fig. 3-2). The other gyrotron is utilized for producing warm electrons in the plug region due to fundamental ECH (plug-ECH).³⁹

3-2 X-ray Detectors

3-2-1 Pulse Height Analysers

The hot electron temperature T_{eh} in the barrier region is measured by two soft X-ray pulse height analysers (PHA) the lines of sight of which lie in the midplane of the barrier region, as shown in Fig. 3-3. A pure germanium detector with a diameter of 1.6 cm and a depletion layer of 1 cm is used to measure the photon spectrum from 1.8 to 260 keV (with more than a 10% detection efficiency (Fig. 3-4), including the photon absorption efficiency of the 0.125 mm beryllium window). A movable stainless steel collimator, 3.5 cm thick, with apertures of 1 mm, 2 mm and 4 mm, and a fixed lead collimator, 9.8 cm thick, with a 1.35 cm slit, are placed in the vacuum chamber. A sodium iodide (NaI(Tl)) detector, 5 cm thick, 2.5 cm in diameter, with a 2 mm aluminium entrance window, is employed to measure the photon spectrum from 20 to 750 keV (Fig. 3-5). In the vacuum chamber, the fixed lead collimator, 5 cm thick with a 12 mm slit, and the exchangeable lead collimator (9 cm thick) and soft iron collimator (2.5 cm thick), with apertures of 2 mm, 4 mm or 8 mm, are carefully aligned. The line of sight of the NaI system, which passes a 2 mm aluminium window, can be tilted to scan the plasma from the centre ($r = 0$) to $r = 18.5$ cm in the midplane of the barrier.

The main aim of the germanium detector is a detailed analysis of T_{eh} . The purpose of the sodium iodide detector

is to measure high energy photons and also to determine T_{eh} . To avoid exposure to background stray photons and to the magnetic field, the detectors are shielded coaxially by 4.5 cm lead, 1 cm soft iron and 0.8 mm Permalloy. Suppression of the background radiation is verified by plugging the front apertures of the detectors. The axial motion of the hot electrons is limited radially by 71 cm i.d. coils positioned in the vacuum vessel at $z = 3.9$ cm from the midplane, the inner edge of the coils being out of the line of sight and far from the vacuum vessel wall. Low-Z material (glass and beryllium) is used for windows in the walls opposite to the detector in order to avoid X-ray line radiation from the wall. Here, Z denotes an effective ion charge. Since no line radiation was in detectable level, its effect on the measurements can be neglected. The detected photon signals are amplified with a shaping time of $2 \mu s$ and analysed in 4096 channels. The channels are divided into 64 or 32 blocks, depending on the duration of the successive sample periods (1 or 2 ms). The temporal evolution of the X-ray spectra is determined by carefully choosing several shots with similar plasma parameters and adding up the spectra with the help of a data processing computer.

In the plug region, together with the pure germanium detector, a silicon lithium (Si(Li)) detector with a diameter of 0.4 cm and a depletion layer of 0.27 cm is used to measure the photon spectrum from 0.7 to 55 keV with a 0.008 mm beryllium window (Figs. 3-6, 3-7). The same system

as the pure germanium detector as described for the barrier X-ray observation is utilized for the Si(Li) detector as well as the pure germanium detector for the plug X-ray detection. These two data are combined, and then provide a wide X-ray energy spectrum from 0.7 keV to 150 keV.

3-2-2 The X-ray Absorption Method

Total X-ray emission from central cell is measured with silicon surface barrier (SSB) detectors with a depletion layer of 100 μm , an aluminium entrance window of 45 $\mu\text{g}/\text{cm}^2$ (the test data value), a silicon oxide dead layer of a nominal value of 100 \AA , and an active area of 300 mm^2 (Tennelec, CE-300-100-21-CB) set in the vacuum vessel (Fig.3-8). In order to avoid detecting fast neutral particles, polypropylene foil with 80 $\mu\text{g}/\text{cm}^2$ is set up in front of the detectors.

In order to analyse the X-ray emission data, various absorbers are used for changing the observed X-ray energy range: 0, 1.5, 2, 3, 3.5, 5 μm polyester combined with the polypropylene, 0, 1.5, 3 μm polyester and 5 μm aluminium combined with the polypropylene. Combination of these absorbers leads to the detectable energy range from 0.2 to 20 keV (Fig.3-9).

The observed X-ray signal is written as follows,

$$I_{sx} = \int_0^{\infty} \frac{dI(k')}{dk'} \exp(-\mu(k') \rho d) \eta_{ssB}(k') dk' \quad (3-1),$$

where μ , ρ and d are the mass absorption coefficient, density and thickness of the absorber, respectively; the SSB detection efficiency $\eta_{ssB}(k')$ for a unit incident photon flux is written as:

$$\eta_{ssB}(k') = c \cdot \exp(-\mu_e \rho_e d_e) \cdot \exp(-\mu_d \rho_d d_d) \times (1 - \exp(-\mu_{dep} \rho_{dep} d_{dep})) \cdot k' \quad (3-2),$$

where the subscripts of e , d , and dep indicate the electrode, the dead layer, and the depletion layer, respectively; c is a constant value. Figure 3-10 shows X-ray intensity as a function of Maxwellian electron temperature with various foils, which is calculated from eq. (3-1). T_e is estimated from the ratio of X-ray intensities with different absorbers. In Fig. 3-11, the calculated intensities with various T_e are normalized by the intensities with the polypropylene absorber alone as a function of the thickness of the polyester and the aluminium. The observed data are fitted on these curves, and then the best fit curve gives the value of T_e . Also, another method of the T_e evaluation is made using the temporal evolution of X-ray intensities of I_{sx} . Under the assumption of a low Z condition or a constant value of Z , I_{sx} is normalized by n_e and n_i , and then compared with the calculated curves in Fig. 3-10, since these curves are normalized by unit values of n_e , n_i and Z . Thus these depend on T_e alone.

3-2-3 X-ray Imaging Systems

A multi-anode Chevron type channel plate (50 channel MCP, Hamamatsu Photonics Type F1943-22MX) is installed for the observation of the radial and axial profiles of the hot electrons in the barrier region (Fig.3-12) as well as of the radial thermal isolation effect between the plug region (Fig.3-13) and the central cell (Fig.3-14).

The MCP has a tandem configuration and is coated with normal electrode materials (Fe and Cr), whose channel diameter is 15 μm , channel pitch 19 μm , length to diameter ratio 40, channel bias angle 13°, and open area ratio 0.57. The soft X-ray radiation is imaged on the MCP through a 1.9 cm thick lead collimator (aperture of 3 mm, spatial resolution in the plasma: 1.7 cm, 2.7 cm, 2.1 cm perpendicular to the line of sight in the barrier, plug, central cell regions, respectively). Lead shields of 0.4 cm and 1.8 cm thickness are placed between the collimator and the MCP. A 1 cm thick vacuum vessel of soft iron is used as magnetic shield. The MCP was calibrated with synchrotron radiation from the storage ring at the National Laboratory for High Energy Physics (KEK). (see §5-1)

To vary the energy range of photons admitted to the detector, the following absorbers are used: For the barrier X-ray, observation are made using 1.5 μm or 5.5 μm thick polyester absorbers (10% transmissivity at 0.17 keV or 1.0 keV), 7 μm or 50 μm aluminium absorbers (0.86 keV or 4.5 keV), and iron absorbers (43 keV). In the plug and central

cell regions, a polypropylene absorber ($80 \mu\text{g}/\text{cm}^2$) is placed at the exist of the collimator hole; another polypropylene filter or 1.5, 2, 4 μm thick polyester absorbers, or 7 μm thick aluminium absorber are inserted to analyse the data. The observed X-ray signals are also written as eq. (3-1) except the replacement of the MCP detection efficiency, $\eta_{\text{MCP}}(k')$ by $\eta_{\text{SSB}}(k')$. The signals are digitized every 80 μs and 40 μs for the central cell and the plug X-rays, respectively, and then transferred to the data processing computer.

The data analyses to reconstruct a two-dimensional X-ray emissivity in the plasma cross section are carried out by using a computer tomography technique. We have used the Cormack inversion,¹⁶ and its procedure including the response characteristics of the MCPs is briefly summarized as follows:

The X-ray brightness, $f(\kappa, \psi)$, measured by each channel of MCPs is a line integral of the X-ray emissivity, $g(r, \chi)$, along the viewing chord, L . Here, (r, χ) represent the polar coordinates, κ is the chord radius and ψ is the angle between the normal to the chord L and the axis given by $\chi = 0$. The brightness $f(\kappa, \psi)$ is written as,

$$f(\kappa, \psi) = \frac{S_e S_d \cos \chi_e \cos \chi_d}{4\pi d^2} \int_L g(r, \chi) dl \quad (3-3),$$

where s_e and s_d are the area of the aperture and the effective area of the MCPs, respectively. The length, d , is the distance from the collimator to the MCPs; χ_e is the angle between the normal to the aperture cross section, l_e ,

and the chord L ; χ_d is the angle between the normal to each detection channel surface of the MCPs, l_d , and the chord L . In our experimental setup, the 50 channel MCPs are assembled in a flat surface, and hence the line l_c , is parallel to the lines l_d . Thus, χ_d equals to χ_c . Therefore, we can rewrite eq. (3-3) to eq. (3-4).

$$f(\kappa, \psi) = \frac{S_c S_d (\cos \chi_c)^4}{4\pi d_0^2} \int_L g(r, \chi) dl \quad (3-4),$$

where d_0 is the distance from the aperture to the center of the MCPs.

Here, it is noted that, in order to obtain the values of $g(r, \chi)$ in eq. (3-4), corrections for the detected MCP currents are made by using the calibration data of the MCPs as well as the X-ray absorber characteristics.

Next, $f(\kappa, \psi)$ and $g(r, \chi)$ are expanded in Fourier harmonics in terms of ψ and χ ;

$$f(\kappa, \psi) = \sum_{m=0}^{\infty} \{f_m^c(\kappa) \cos m\psi + f_m^s(\kappa) \sin m\psi\} \quad (3-5),$$

$$g(r, \chi) = \sum_{m=0}^{\infty} \{g_m^c(r) \cos m\chi + g_m^s(r) \sin m\chi\} \quad (3-6),$$

where $f_m(\kappa)$, and $g_m(r)$ are the expansion coefficients, and for simplicity, the constant value on the right hand side of eq. (3-4) is replaced by unity. If $f_m(\kappa)$ is expanded in the following form,

$$f_m^{c,s}(\kappa) = 2 \sum_{l=0}^{\infty} a^{(c,s)}_{ml} \sin\{(m+2l+1)\cos^{-1}\kappa\} \quad (3-7),$$

then the function $g_m(r)$ is

$$g_m^{c,s}(r) = \sum_{l=0}^{\infty} (m+2l+1) a^{(c,s)}_{ml} R_m^{-1}(r) \quad (3-8),$$

and

$$R_m^l(r) = \sum_{n=0}^l \frac{(-1)^n (m+2l-n)! r^{m+2l-2n}}{n! (m+l-n)! (l-n)!} \quad (3-9),$$

where $R_m^l(r)$ is the Zernicke polynomial. In our data analyses, we take into account angular harmonics of $m = 0$, $\cos \chi$, $\sin \chi$ and $\cos 2\chi$ as well as radial harmonics from $l = 0$ to L_0 , L_1^c , L_1^s and L_2^c , respectively. The coefficients of $a^{(c,s)}_{m,l}$ are determined by the least squares fit, that is, the following value is minimized:

$$\begin{aligned} & \sum_{i=1}^N (u_i - 2 \sum_{l=0}^{L_0} a_0^l \sin\{(2l+1)\cos^{-1} \kappa_i\} \\ & - 2 \sum_{l=0}^{L_1^c} a_1^l \cos \phi_i \sin\{(2l+1)\cos^{-1} \kappa_i\} \\ & - 2 \sum_{l=0}^{L_1^s} a_1^l \sin \phi_i \sin\{(2l+1)\cos^{-1} \kappa_i\} \\ & - 2 \sum_{l=0}^{L_2^c} a_2^l \cos 2\phi_i \sin\{(2l+3)\cos^{-1} \kappa_i\})^2 \end{aligned} \quad (3-10),$$

where u_i is i -th data and N is a number of detectors.

Chapter 4. Hot Electron Production in the Barrier Region

4-1 Experimental Results

4-1-1 Typical Data Set

In Fig. 4-1, typical soft X-ray spectra, detected with the pure germanium detector and the NaI detector, are plotted as a function of the emitted photon energy $h\nu$. The solid and dashed curves are calculated by using single-component relativistic Maxwellian distributions, $f = \alpha \cdot \exp(-\sqrt{p^2 c^2 + m_0^2 c^4} / T_{eh})$, with the hot electron temperature T_{eh} of 50 keV. Here, p and $m_0 c^2$ are the electron momentum and rest energy, respectively; the factor α normalizes f . The observed X-ray intensity per unit of solid angle, $dI/d\Omega$, is written as;

$$\frac{dI(k', \theta') \Delta \Omega}{d\Omega} = k' n_e n_i \int \frac{p(E_{max})}{p(k')} p^2 dp \int_{\theta_0}^{\pi - \theta_0} \sin \theta d\theta$$

$$\times f v \int_0^{2\pi} d\phi \frac{d^2 \sigma}{dk' d\Omega} \Delta \Omega \quad (4-1),$$

where $I(k', \theta')$ is the emitted X-ray intensity per unit volume, unit time and unit energy interval, as functions of the photon energy k' and the angle θ' between B and the emitted photons. $\Delta \Omega$ is the solid angle viewed by the detector, and v is relativistic velocity. Here, the angular anisotropy of the ECH-produced hot electrons is taken into account; that is, the θ -integration is carried out from θ

$= 55^\circ$ to $\theta = 125^\circ$, ($\theta_0 = 55^\circ$). This value of θ_0 is obtained by the X-ray axial profile measurement using the bounce motion formula as functions of θ and B (see §4-2-3). (The angular distribution is represented in terms of θ_0 .) The angular dependence of the Bremsstrahlung cross section is $d^2\sigma/dk'd\Omega$, where Ω is the solid angle between the observed photon momentum and p . For the value of the Bremsstrahlung cross-section,^{40, 41} the relativistic Born approximation is used, corrected by the Elwert factor⁴² in order to improve the tip region of the photon emission spectrum. For example, several cases with various electron temperatures as well as various angular distributions are shown in Figs. 4-2(a), (b).

In the following, a data set in the barrier region for a typical discharge with a thermal barrier is presented. Figures 4-3(a)-(e) show the temporal evolution of soft X-ray spectra measured with the NaI detector. The dotted curves are calculated by using eq. (4-1). In Fig. 4-4, the X-ray spectra from 6 to 9 ms after the microwave is switched on are plotted (corresponding to Fig. 4-3(c)); these spectra are obtained for a total of 5 shots, 10 shots and 40 shots. In this Figure, the X-ray intensities for a total of 10 and 40 shots can be fitted to the curves, whose intensities are 2 and 8 times as large as that for a total of 5 shots, respectively. It is noteworthy that the maximum energy of the three spectra is the same value ($E_{\max} = 250$ keV). This suggests the existence of a physical mechanism for limiting the electron acceleration. This mechanism is

discussed in §4-2-2.

Figure 4-5 shows a typical data set with a thermal barrier. After the barrier ECH is switched on, T_{eh} , obtained by the soft X-ray spectra, increases up to $t \approx 10$ ms ($T_{eh} \approx 60$ keV) and reaches saturation thereafter (Fig. 4-5(a)). The diamagnetic signals, $\Delta\Phi_{dia}$, increases during ECH and decays slowly after the power is switched off (Fig. 4-5(b)). The hot electron density at the magnetic axis, n_{eh0} , increases steadily, even after the saturation of T_{eh} (Fig. 4-5(c)). At $t \geq 3$ ms, the line density $n_b \cdot l_b$ is constant (Fig. 4-5(d)), and the ion density on axis, n_{b0} , is constant as well (Fig. 4-5(e)). The ratio of the hot electron density to the total density on the magnetic axis, n_{eh0}/n_{b0} , is calculated as follows: Radial profiles of soft X-rays using the MCP with $1.5 \mu m$ or $5.5 \mu m$ thick polyester absorbers and a $50 \mu m$ thick aluminium absorber are obtained with the same ratio of relative intensities radially. This shows that the electron temperature (or the electron distribution function) is radially uniform. The radial profiles of the square root of the Abel inverted soft X-ray signals, $\sqrt{I_{SX-Abel}}$, using the $1.5 \mu m$ polyester absorber correspond to the bulk electron density profile under our low-Z experimental condition.¹² (In fact, this X-ray profile shows a similar radial profile compared to the central cell density profile and the ion-end-loss profile for an unplugged operation measured with multi-gridded electrostatic end-loss-ion energy analysers (hereafter referred to as ELAs).) Along with the data on

$n_b \cdot l_b$, n_{b0} is obtained. Similarly, n_{eh} is obtained using the X-ray signal with the 50 μ m aluminium absorber along with $\Delta\Phi_{dia}$. This X-ray energy range above 4.5 keV is confirmed to radiate from the hot electron component (see the hot electron energy spectra in Figs. 4-3 and 4-4). Using these experimental results, the ratio of n_{eh0}/n_{b0} is obtained; this ratio increases linearly with time (Fig. 4-5(f)). It is noteworthy that the different dependence of T_{eh} and n_{eh} as a function of time is important to obtain a high density of n_{eh} without increasing T_{eh} ; since a large density ratio of n_{eh0}/n_{b0} contributes to the thermal barrier potential formation, the saturation of T_{eh} is desirable for MHD stability so as to maintain a low beta value in the axisymmetric barrier region. Figure 4-5(g) shows that E_{max} obtained in Fig. 4-4 reaches 250 keV at $t = 6-9$ ms, and thereafter it increases slowly. The FWHM of the RMS of the Abel inverted soft X-ray signal slowly increases towards a value of 40 cm (Fig. 4-5(h)).

It is noted that the thermal barrier potential at $r = 0$ is observed to be 150 V at $t = 10$ ms; this value is consistently interpreted by eq. (2-4). At $r = 0$, the experimental values of $T_{ec} = 100$ eV, $n_e = 6.3 \times 10^{11} \text{ cm}^{-3}$, $n_b = 3 \times 10^{11} \text{ cm}^{-3}$ and $n_{eh}/n_b = 0.17$ lead to $\phi_b = 152$ V, which agrees well with the observed value.

4-1-2 Dependence of the Plasma Parameters on Various Operating Conditions

The dependence of the plasma parameters on the hydrogen filling pressure, p_b , n_b , and P_{ECH} is now discussed in connection with the production mechanism of hot electrons in the barrier region.

Figure 4-6 presents a comparison of the data sets at $p_b = 8.0 \times 10^{-8}$ and $p_b = 2.0 \times 10^{-6}$ torr ($t = 10$ ms) with the data sets at $p_b = 1.1 \times 10^{-7}$ torr as presented in Fig. 4-5. The values for n_{b0} are $0.6 \times 10^{11} \text{ cm}^{-3}$ and $1.5 \times 10^{12} \text{ cm}^{-3}$ at $t = 10$ ms after the barrier ECH is switched on. In all three data sets, the rise time of T_{eh} becomes shorter with decreasing p_b or n_b ; this can be interpreted as follows⁷: The electrons are accelerated by ECH and decelerated by e-n, e-e and e-i collisions. To become hot, the electrons must at first surpass the critical velocity $v = v_{cr}$ derived in ref. 43 from

$$\frac{dp}{dt} = -\frac{e^4 n_e \ln \Lambda}{2\pi \epsilon_0^2 m_0 \gamma v^3} + e(E + \frac{p}{m_0 \gamma} \times B_0) = 0 \quad (4-2),$$

where $\gamma = (1 + (p/m_0 c)^2)^{1/2}$. Equation (4-2) gives the acquired energy in eV;

$$W_{cr} = \frac{mv_{cr}^2}{2e} \propto \frac{n_i}{E_{cr}} \quad (4-3),$$

where it is assumed that the relativistic phase detuning effect⁴³ is negligible in this energy range. The electrons are accelerated to higher energies when they cross the resonance locations during the bounce motion. When the

heating time interval becomes long, the probability of Coulomb collisions during the bounce motion becomes high. Since before crossing the resonance zones the energies of the electrons are constant, this probability is proportional to the density. Thus, not only W_{cr} as given by eq. (4-3) but also the disturbance of the accelerating electrons due to the collisions during the bounce motion depend on the density. A high value of the density thus prevents the production of hot electrons. Furthermore, a high p_b also prevents the acceleration process of hot electrons through the process of e-n collisions, thereby further increasing the rise time of T_{eh} .

Figure 4-7(a) is a plot of n_{b0} and $\Delta\Phi_{dia}$ as a function of p_b ; n_{b0} has its maximum value at $p_{b\max} = 2.7 \times 10^{-6}$ torr. With p_b increasing from 0.12×10^{-6} torr to 2×10^{-6} torr, n_{b0} increases by a factor of 4, but $\Delta\Phi_{dia}$ and T_{eh} decrease only by factors of 1.3 and 1.2, respectively, resulting in a decrease of n_{eh0}/n_{b0} by a factor of 1.7 (see Fig. 4-7(b)). This suggests that the number of neutral particles, n_0 , is an essential particle source for the production of n_b when n_0 is nearly constant, as shown in Fig. 4-7(c). Hot electrons can easily be produced under the conditions of low p_b and low n_b because of the low collision frequency, as mentioned above. After the production of the hot electrons it is convenient to confine them under the condition of a low probability of pitch angle scattering. As p_b increases from 10^{-6} torr to 3×10^{-6} torr, n_{b0} also increases and the production of hot electrons is prevented

owing to the high collision frequency which results in the decrease of $\Delta\Phi_{dia}$. When we compare the data at $p_b = 2$ and 2.7×10^{-6} torr, n_{b0} increases by a factor of 1.4 and $\Delta\Phi_{dia}$ decreases by a factor of 2.1, the value of T_{eh} remaining unchanged; this suggests that the decrease of $\Delta\Phi_{dia}$ is due mainly to collisions during the acceleration process. Pitch angle scattering does not seem to play a major role here since the end loss of hot electrons is negligible (as observed with the ELA, at an ion repeller voltage higher than the highest potential in the plasma); besides, this loss is the same for the two pressures.

In the region beyond $p_{b\max}$, n_{b0} decreases with increasing p_b . In comparing the discharges at $p_b = 0.27 \times 10^{-6}$ torr and 1.6×10^{-5} torr, the line density in the central cell $n_e \cdot l_e$ and n_{b0} decrease by factors of 2.5 and 2.9, respectively, while the ion end loss current I_{ELA} decreases only by a factor of <1.5 (Fig. 4-7(c)), indicating an increase of axial particle loss. This may be explained by a reduction of the trapping efficiency η_t of the produced plasma. This is particularly important for the cold plasma component which is the dominant component in this pressure range as shown in Fig. 4-7(b). η_t depends on the probability of pitch angle scattering, which is higher for the cold plasma electrons than for the hot electrons. This results in a decrease of n_{b0} for $p_b > 2.7 \times 10^{-6}$ torr (under the condition of $\phi_b \approx 0$) and in a reduction of $\Delta\Phi_{dia}$ because of the loss of source electrons which are in the process of being accelerated to become hot electrons.

Figure 4-8 shows $\Delta\Phi_{dia}$ and T_{eh} as a function of n_{b0} , observed at $t = 6.5$ ms and $t = 15$ ms after switching on the barrier ECH; the maximum value of $\Delta\Phi_{dia}$ is reached at $n_{b0} \approx 1 \times 10^{12} \text{ cm}^{-3}$. This n_{b0} dependence is explained as follows: The open circles and triangles in Fig. 4-8(a) are the data for $p_b < 3 \times 10^{-6}$ torr; they indicate that electron acceleration may be easy in the range of $n_{b0} < 3 \times 10^{11} \text{ cm}^{-3}$ because of the low collision frequency, but the number of electrons fuelled by neutral particles is small, which results in a small number of n_{eh} being produced. On the other hand, the effect of frequent collisions and the reduction of η_i make $\Delta\Phi_{dia}$ small in the range $n_{b0} > 1 \times 10^{12} \text{ cm}^{-3}$. In the intermediate region of n_{b0} , the competition between these effects may cause a gradual increase of $\Delta\Phi_{dia}$. The solid circles and triangles in Fig. 4-8(a) are for $p_b > 7 \times 10^{-6}$ torr; they indicate that $\Delta\Phi_{dia}$ is reduced by several times ten per cent compared with the lower pressure even at the same value of n_{b0} . This may be ascribed to the reduction of η_i as was discussed in connection with Fig. 4-7. The comparison of T_{eh} at different times in Fig. 4-8(b) shows a slow increase of T_{eh} with increasing n_{b0} , which can be ascribed to collisions that prevent the acceleration of electrons. It is noted that the values of T_{eh} at $t = 15$ ms, which are almost saturated (see Figs. 4-5 and 4-6), become slightly larger with increasing n_{b0} ; this mechanism is discussed in §4-2-2.

Figures 4-9(a), (b) show the temporal evolution of T_{eh} and $n_b \cdot l_b$ for three different values of P_{ECH} . The values of

$n_b \cdot l_b$ are nearly the same for the three power levels, showing that the rise time of T_{eh} increases with increasing P_{ECH} . This is explained as follows: The electron acceleration becomes large with increasing P_{ECH} , but the background plasma density does not change. This results in strong acceleration of the electrons during one collision time, which leads to efficient production of hot electrons, as shown in Fig. 4-9(c). Once p has become large and the Coulomb collisions can no longer compete with the acceleration by the wave, the electrons are accelerated to become hot electrons (until the relativistic mass variation limits the acceleration); this results in the fast rise of T_{eh} as shown in Fig. 4-9(a).

Figures 4-5, 4-6 and 4-9(a) show the saturation of T_{eh} both as a function of time and as a function of P_{ECH} (as discussed earlier), whereas n_{eh} continues to increase. The different dependence of T_{eh} and n_{eh} on P_{ECH} is important to obtain a high value of n_{eh} without increasing T_{eh} , since a high value of n_{eh0}/n_{b0} contributes to the formation of the thermal barrier. The saturation of T_{eh} is desirable for MHD stability in order to maintain a low beta value in the axisymmetric barrier region.

4-2 Physical Mechanism Studies of the Hot Electron Production Conditions

4-2-1 Electron Cyclotron Heating (ECH)

The n -th harmonic resonance condition for ECH is written in terms of k_{\parallel} , θ , and a relativistic kinetic energy W :^{1,2}

$$\omega = \frac{n \cdot \Omega_e}{\gamma} + k_{\parallel} \cdot v_{\parallel} \quad (4-4),$$

where

$$\gamma = 1 + \frac{W}{m_0 c^2} \quad (4-5),$$

and

$$\frac{v_{\parallel}}{c} = \frac{v}{c} \cdot \cos \theta = (1 - \gamma^{-2})^{1/2} \cdot \cos \theta \quad (4-6).$$

Here, the parallel wave number k_{\parallel} is described as $k_{\parallel} = N_{\parallel} \omega / c$ and $\Omega_e = eB/m_0$. On the right-hand side of eq. (4-4), the first term represents the cyclotron frequency taking account of the relativistic mass variation. The second term corresponds to the Doppler shift.

In Fig. 4-10, the resonance conditions from eq. (4-4) with $n = 2$ are shown by solid curves in the θ vs Ω_e / ω plane for various values of W . Figures 4-10(a) and 4-10(b) correspond to $k_{\parallel} \cdot v_{\parallel} < 0$ and $k_{\parallel} \cdot v_{\parallel} > 0$, respectively. Here, the values of $k_{\parallel} \cdot v_{\parallel}$ are negative when the electron movements are antiparallel to the direction of wave propagation and positive when the movements are parallel. The dashed curves show the electron bounce motions in the

case without ECH. The electron heating occurs at the points where the dashed curves cross the solid curves. Here, ECH characteristic features for the electrons with $k_{\parallel} \cdot v_{\parallel} > 0$ and with $k_{\parallel} \cdot v_{\parallel} < 0$ are compared from Figs. 4-10(a) and 4-10(b). The value of θ in Fig. 4-10(a) increases with increasing W ; this is convenient for successive ECH to higher energies since ECH results in increasing θ . Thus, the electron heating can easily take place, and high energy electrons are produced. On the other hand, for the resonance conditions in Fig. 4-10(b), θ decreases with increasing W . In contrast to case Fig. 4-10(a), this characteristic in Fig. 4-10(b) is not advantageous for ongoing ECH.

Under the experimental conditions described in §3-1 and Fig. 3-2, the incident microwave lobe is limited to the region of $\Omega_e/\omega = 0.5-0.55$ and the cavity field is observed to be much smaller than the incident microwave intensity in the lobe.^{11, 12} Thus, ECH occurs in the region of $0.5 \leq \Omega_e/\omega \leq 0.55$, and electron bounce motions are limited in the region of $\Omega_e/\omega \gtrsim 0.5$ in Fig. 4-10. (For example, along the bounce trajectory of A-B in Fig. 4-10(a), the resonance conditions for the 0-16.5 keV electrons alone are satisfied.) The value of N_{\parallel} does not change through the plasma, since the ray bending effect is negligible under our low density condition.

4-2-2 Heating Processes and T_e -Saturation Mechanism

In §4-2-1, the solutions of eqs. (4-4)-(4-6) are obtained graphically; they show the values of θ and Ω_e/ω at each resonance point individually. The next problem is how to represent the resonance conditions which are successively satisfied during the electron heating processes, since the values of θ and W before and after ECH are closely related to each other. Such a curve showing the electron heating process in the velocity space is often known as the heating characteristic;⁴⁴ along this heating characteristic curve, electrons are accelerated or decelerated according to the phase relation between the electrons and the incident wave field.

Like these heating characteristics, a thick curve in the θ vs Ω_e/ω plane (Fig. 4-11) schematically represents a heating process for an electron moving along the bounce orbit of the dashed line (a) (towards the higher field side) starting with $W = 2$ keV and $\theta = 50^\circ$ at the midplane. Here, we assume that the electron is kept in the acceleration phase. However, even if a deceleration process due to the phase mismatching is included in this representation, a similar curve is traced as shown in Fig. 4-13 (see below). The electron is accelerated at the point (a) of intersection with the resonance condition for $W = 2$ keV (solid thin line). Suppose the electron attains the perpendicular energy increase of $\Delta W = 2$ keV at this point, the value of θ increases and the orbit of the

electron motion changes into the dashed line (b). Next, the electron with 4 keV on (b) is accelerated to 6 keV at the point of intersection between (b) and the resonance condition for $W = 4$ keV. It then moves along the orbit (c) until the next resonance condition is satisfied. Using this method, we can obtain the electron heating characteristic curve in the θ vs Ω_e/ω plane. It is noted that, in Fig. 4-11, any initial energy, even below 2 keV, gives essentially the same result.

In Fig. 4-12, more realistic cases are represented. It is noted that the maximum energy gain, ΔW_{\max} , due to ECH is limited by the phase detuning between the electron gyration and the wave field; ΔW_{\max} is written by^{7, 43}

$$\Delta W_{\max} \text{ (eV)} = \frac{2mc^2}{e} \left(\frac{e|E|}{m\omega c} \right)^{2/3} \quad (4-7).$$

Using $|E| = 100 \text{ V}\cdot\text{cm}^{-1}$ which is estimated from a ray tracing calculation, we obtain $\Delta W_{\max} \approx 1 \text{ keV}$; thus, ΔW in Fig. 4-12 ranges within this limited value. Assuming the initial kinetic energy of the electron, W_i , its pitch angle at the midplane, θ_i , and $\Delta W = 0.2 \text{ keV}$, we successively carry out the calculation until the resonance condition cannot be satisfied on the electron bounce orbit. If we use $\Delta W = 0.5 \text{ keV}$ or 1 keV in the calculation, we obtain nearly the same results.

Heating processes labelled (A)-(E) in Figs. 4-12(a)-(c) start at $\theta_i = 44^\circ, 70^\circ, 0^\circ, 38^\circ, 38.5^\circ$ with $W_i = 2 \text{ keV}$; dashed lines are the final bounce orbits for the heated electrons. The curve labelled (A) shows a typical ECH

process for producing high energy electrons. The electron begins to satisfy the resonance condition at $\Omega_e/\omega = 0.521$, and then it reaches $W \approx 50$ keV at $\Omega_e/\omega = 0.55$ and $\theta \approx 90^\circ$ (the turning point). In this heating process, the resonance conditions with $k_{\parallel} \cdot v_{\parallel} < 0$ alone are satisfied. However, even after the electron heating takes place near the turning point, a further heating process is expected when we take account of the resonance conditions with $k_{\parallel} \cdot v_{\parallel} > 0$ in eq. (4-4). The electron reaches the final values of the energy $W_f = 61$ keV; thereafter, it moves along the dashed line (a bounce motion) without heating (see the curve (A') in Fig. 4-12(a)). For its further acceleration from $W_f = 61$ keV, its pitch angle changes due to collisions are indispensable. In this case, a resonance condition must exist with $k_{\parallel} \cdot v_{\parallel} > 0$ for the electron motion along the new bounce orbit with 61 keV. As we can see from Fig. 4-10(b), this value of θ satisfying the requirement for the further ECH is limited within a narrow region (see the hatched region in Fig. 4-10(b)).

The heating curve labelled (B) is calculated from the resonance conditions with $k_{\parallel} \cdot v_{\parallel} < 0$ until the acceleration occurs at $\theta = 90^\circ$. The electron satisfies the resonance conditions with $k_{\parallel} \cdot v_{\parallel} > 0$, and finally reaches $W_f = 26.2$ keV and $\theta_f = 78.4^\circ$. For the curve (C), the electron satisfies the resonance conditions with $k_{\parallel} \cdot v_{\parallel} < 0$ alone. At the point of $\Omega_e/\omega = 0.55$ on curve (C), the electron acceleration finishes at $W_f = 26$ keV and $\theta_f = 67.3^\circ$ since the electron bounce motion cannot intersect either

resonance condition with $k_{\parallel} \cdot v_{\parallel} > 0$ or $k_{\parallel} \cdot v_{\parallel} < 0$ thereafter. The values of W_r for (B) and (C) are smaller than that for (A), therefore these electrons have a higher probability of pitch angle scattering, compared with (A). If these electrons on (B) and (C) are scattered, for example, by pitch angle change of -6.4° and $+4.7^\circ$ at $B = 0.5$ T, they satisfy the resonance conditions with $k_{\parallel} \cdot v_{\parallel} < 0$ on curve (A) during the bounce motion; thereafter, these electrons follow the ECH process of (A) up to $W_r = 61$ keV.

The difference in θ_i between (D) and (E) is 0.5° , whereas a large difference in W_r is resulted; (W_r, θ_r) is $(38.2$ keV, $71.5^\circ)$ and $(61.2$ keV, $72.5^\circ)$, respectively. This large difference of W_r is determined by whether the resonance conditions with $k_{\parallel} \cdot v_{\parallel} > 0$ are satisfied or not after the accelerations under the resonance conditions with $k_{\parallel} \cdot v_{\parallel} < 0$ are completed. Curve (D) is calculated from the resonance conditions with $k_{\parallel} \cdot v_{\parallel} < 0$ alone, whereas curve (E) is calculated from the resonance conditions with $k_{\parallel} \cdot v_{\parallel} < 0$ as well as from the resonance conditions with $k_{\parallel} \cdot v_{\parallel} > 0$. Actually, the electrons located above curve (D) ($\theta < 38.1^\circ$ at 0.5 T) are heated due to the resonance conditions with $k_{\parallel} \cdot v_{\parallel} < 0$ alone, where they cannot satisfy the resonance conditions with $k_{\parallel} \cdot v_{\parallel} > 0$. However, the electrons located below curve (E) ($\theta \geq 38.1^\circ$ at 0.5 T) may be coupled with both resonance conditions with $k_{\parallel} \cdot v_{\parallel} > 0$ and $k_{\parallel} \cdot v_{\parallel} < 0$. Therefore, curve (D) gives a boundary for these different characteristic features of resonance conditions in the θ vs Ω_e/ω plane. It is noted that if an electron

accelerated along curve (D) happens to have a pitch angle change of $\Delta\theta < 0$ due to a collision, then this electron cannot satisfy the resonance conditions with $k_{\parallel} \cdot v_{\parallel} > 0$ (as far as this electron does not experience another larger scattering with $\Delta\theta > 0$ beyond this boundary curve (D)).

Thus, these characteristic features of the representation on the θ vs Ω_e/ω plane have the advantage of showing the electron acceleration process visually in the real space; namely, the spatial location of the accelerated electron is given by Ω_e/ω or B, and the electron orbit variation is represented by θ during acceleration (the orbit does not depend on W but on θ and Ω_e/ω alone). Therefore, we can easily obtain the image of the wave-particle interaction process in the mirror field. Furthermore, W during the heating process is immediately obtained by superposing Fig.4-10 on this heating curve. For instance, W at the point M on curve (A) is directly obtained by superposing Fig.4-10 on Fig.4-12(a); namely, W = 4 keV (for reference, this is also shown by point M in Fig.4-10).

It is noted that in Fig.4-12, the most efficient heating curves are assumed so as to trace the heating characteristics. In Fig.4-13, we demonstrate the case of the reduction of ΔW during the heating process in the θ vs Ω_e/ω plane. This may occur, for instance, due to the phase mismatching between an electron cyclotron motion and the microwave. For this purpose, the following heating process is depicted. The initial condition in Fig.4-13 is

the same as the case labelled (A) in Fig. 4-12. Fifty acceleration processes ($\Delta W = 0.2$ keV) and one deceleration process ($\Delta W = -2$ keV) are repeated until the resonance condition is lost. Here, to emphasize the deceleration effect, we employ a larger deceleration energy than the acceleration energy. However, this calculation leads to $W_r = 60.4$ keV; this value is nearly the same as W_r of curve (A) in Fig. 4-12. Furthermore, nearly the same heating curve is calculated, compared with (A), except for the additional curves due to the deceleration. Similar calculations are carried out using several different values of the deceleration energy and probability; all of them trace the same curve labelled (A). Thus, these features indicate that the presentation of the heating process on the θ vs Ω_e/ω plane behaves similarly to the heating characteristics⁴⁴ on the velocity space (which are also employed for Fokker-Planck simulation using the diffusion coefficients of wave heatings). In this paper, our treatment of the heating processes is based on a wave-particle interaction. To determine the whole distribution function of electrons resulting from ECH, it is necessary to give their initial energies and phases. (The probabilities of the acceleration and the deceleration are determined according to these initial conditions as well as the wave field intensity and its phase.) As a future plan, this method on the θ vs Ω_e/ω plane will be developed and applied to particle simulation of ECH by determining the whole electron distribution function in the initial stage.

From these results in the θ vs Ω_e/ω plane, we discuss the mechanism of T_{eh} -saturation. In Fig. 4-14, W_r for $W_i = 1, 2, 4$ and 20 keV is shown as a function of θ_i . The points (A)-(E) correspond to W_r for the heating processes labelled (A)-(E) in Fig. 4-12, respectively. For the electrons with $W_i = 1$ keV, both of the resonance conditions with $k_{\parallel} \cdot v_{\parallel} > 0$ and $k_{\parallel} \cdot v_{\parallel} < 0$ are satisfied along their heating curves. As seen in Fig. 4-14, for electrons with $W_i = 1$ keV, W_r increases with decreasing θ_i . For $W_i = 2$ keV, both resonance conditions are satisfied from $\theta_i = 90^\circ$ to $\theta_i = 38^\circ$ (point(E)). However, it is noted that a remarkable jump in W_r is seen from the point (E) to the point (D). As described earlier, this is explained from the fact that the resonance conditions with $k_{\parallel} \cdot v_{\parallel} < 0$ alone are satisfied during the heating in the case of (D). Therefore, this jump corresponding to the boundary curve (D) in Fig. 4-12(b) is characterized by the change of the resonance conditions. Similar jumps are seen for $W_i = 4$ and 20 keV. Furthermore, it is noteworthy that in any case of Fig. 4-14, W_r is limited to about 60 keV; this value is nearly the same as the observed saturation temperature. Further numerical calculation with changing W_i and θ_i shows that the maximum value of $W_r \approx 60$ keV is maintained in the region of $W_i \leq 43$ keV. This indicates that for the electron acceleration to the region of more than 60 keV, a pitch angle scattering for the electrons with $W \geq 43$ keV into a narrow region of θ_i is required (for instance, $69^\circ \leq \theta_i \leq 74^\circ$ for $W = 50$ keV); for these values of θ_i , the resonance

conditions are satisfied with these scattered electrons, but Coulomb collisions are infrequent in this high energy region. However, frequent collisions below a few tens of keV can be expected; this leads to the electron heating up to 60 keV for the majority of the hot electrons. Taking into account the facts that the electrons accelerated up to W_r cannot be further accelerated or decelerated without collisions, and that the collisions are infrequent, we can expect that the electrons have an average temperature of around $W_r = 60$ keV, which is the observed value with the soft X-ray diagnostics (see Fig. 4-5).

Now, we discuss the acceleration process of the electron with $E_{\max} \approx 250$ keV in the θ vs Ω_e/ω plane. As described above, the acceleration of electrons with an initial energy of a few tens of keV is limited to less than 60 keV; therefore, such a value of E_{\max} cannot be obtained without pitch angle scattering. In order to satisfy the resonance conditions over 60 keV, smaller values of θ are required (see Fig. 4-10(b)). This feature is demonstrated in Fig. 4-15. Here, the production of an electron with $W_r = 250$ keV is shown. The dot-dashed curve in Fig. 4-15 is the final bounce orbit of (A) in Fig. 4-12 (in which the resonance condition is lost at $W_r = 61$ keV). If this electron is scattered to the bounce orbit with $\theta = 67^\circ$ at $\Omega_e/\omega = 0.5$, then the resonance condition for $W = 61$ keV is satisfied along this bounce orbit. (Note that this value of θ leads to the maximum value of W_r compared with the other values of θ .) Consequently, the electron acceleration

occurs again at $W_i = 61$ keV and $\theta_i = 67^\circ$, and finishes at $\Omega_e/\omega = 0.55$, $W_f = 86.8$ keV and $\theta_f = 69.3^\circ$ (curve (a)). It is noted that for satisfying this new resonance condition for $W = 61$ keV, a limited range of pitch angles ($67^\circ \leq \theta_i \leq 72.5^\circ$) is required; that is, the resonance condition does not exist beyond this region. The minimum scattering time, τ_m , for satisfying this resonance condition results from the smallest pitch angle change, $\Delta\theta_m$, into this orbit, because of $\tau_m = \tau_\perp \cdot (\Delta\theta_m/90^\circ)^2$, where τ_\perp is a 90° -scattering time for electrons. For an electron transition from one bounce orbit to another, $\Delta\theta$ becomes larger with increasing B (see Fig. 4-10(b)). Thus, the scattering with τ_m is expected to occur at the location of the smallest value of Ω_e/ω ($= 0.5$).

Therefore, in Fig. 4-15, for estimating the shortest scattering time to reach $W_f = 250$ keV, we assume the next scattering at $\Omega_e/\omega = 0.5$ to the orbit (b) with $\theta = 62.5^\circ$ after the resonance conditions are lost; in this case, the values of W_i , θ_i , W_f and θ_f are 86.8 keV, 62.5° , 119.2 keV and 65.1° , respectively. Similarly, for the most efficient successive electron heating to $W_f = 250$ keV, three further pitch angle scatterings are assumed at $\Omega_e/\omega = 0.5$. For each scattering, W_f becomes 157.8, 202, and 251.6 keV as shown by the heating curves labelled (c)-(e) in Fig. 4-15. This figure demonstrates the importance of the pitch angle scattering for ECH taking account of the relativistic mass variation and the Doppler effect. It is also noted that this representation in the θ vs Ω_e/ω plane gives a

rather simple method for estimating its acceleration time to $W_f = 250$ keV. In this example, we assume the most efficient case; thus, the summation of each small pitch angle scattering time gives the minimum value of this acceleration time. In this case, through these five scatterings, it takes 20-30 ms to obtain $W = 250$ keV; here, we use the above-mentioned formula for τ_m , into which we substitute the changes in θ at $\Omega_e/\omega = 0.5$ and the values of τ_\perp corresponding to W at each pitch angle scattering. This time is equal to the experimental value within a factor 2-3. Such a long collision time prevents formation of a Maxwellian distribution in the region beyond a few hundred keV; this may result in the existence of E_{\max} as shown in Fig. 4-4.

With regard to the relation between these collisions and T_{eh} , it is noteworthy that the electrons can be accelerated to 60 keV in the case where pitch angle scattering in the range above a few keV is not essential. For instance, curve (A) of Fig. 4-12(a) shows that the value of 60 keV can be obtained without any pitch angle scattering during the heating process above 2 keV. This suggests that such a process may occur even for the cases of low n_b or high T_{eh} (where pitch angle scatterings are infrequent). This mechanism leads to the T_{eh} -saturation in the range of 50-60 keV. On the other hand, with higher n_b , the processes of pitch angle scatterings become important even for high energy electrons. These pitch angle scatterings lead to smaller values of θ . For these

scattered electrons, new resonance conditions may be satisfied, and these electrons are accelerated to more than 60 keV; this may lead to an increase of T_{eh} . This may be consistent with the experimental data presented in Figs. 4-6, 4-7(b) and 4-8(b), where T_{eh} and E_{max} increase with increasing n_{b0} , suggesting a correlation with pitch angle scattering. This feature is qualitatively consistent with the results discussed above, namely, the increased probability of pitch angle scattering into the smaller θ leads to the production of higher energy electrons.

4-2-3 Comparison between a New-Representation Method of ECH ($\theta - \Omega_e/\omega$ plane) and the Conventional Method Using Momentum Space

The representation method of resonance conditions in the θ vs Ω_e/ω plane and a conventional method in the momentum (or velocity) space (Fig. 4-16) are compared in the following. In Fig. 4-16, the distance from the origin to each point in the momentum space indicates the relativistic momentum p normalized by $m_0 \gamma c$ and its angle Θ from the horizontal axis indicates the electron pitch angle mapped on the midplane. Thus, each point on the straight line from the origin with $\Theta = a^\circ$ corresponds to an electron with $\theta = a^\circ$ at $\Omega_e/\omega = 0.5$. Therefore, each point also represents electron bounce motion which is mapped onto the midplane. It is noteworthy that this feature of Fig. 4-16 has a disadvantage; that is, we cannot distinguish the difference of spatial locations along a bounce motion which is mapped onto and represented by only one point in Fig. 4-16. In Fig. 4-16, the resonance conditions are satisfied within the area bounded by solid curves (the resonance conditions with $k_{\parallel} \cdot v_{\parallel} < 0$) and by dashed curves (those with $k_{\parallel} \cdot v_{\parallel} > 0$). Here, resonance conditions for $n = 2$ and 3 within the microwave lobe region are shown in the form of the mapping on the midplane. The relation between Fig. 4-16 and Fig. 4-10 is as follows: the energy range satisfying the resonance conditions for electrons with $\theta = a^\circ$ at $\Omega_e/\omega = 0.5$ during their bounce motions corresponds to the intersected

region between the straight line from the origin with $\Theta = a^\circ$ and the area satisfying the resonance conditions in Fig. 4-16. One advantage of Fig. 4-10 over Fig. 4-16 is the following: when two different locations (with different values of B) along a bounce orbit are satisfied by the resonance condition for an energy of W (for instance, see points C and D in Fig. 4-10(b)), this information is lost as there is only one degenerated point, E, in Fig. 4-16. Thus, as noted above, these two spatially separated locations satisfying the resonance condition for W along a bounce orbit cannot be distinguished in this momentum space (Fig. 4-16).

Another comparison between the two planes is made in the following. Figure 4-17 shows the heating characteristic paths in the momentum space; the solid curves labelled (A)-(E) correspond to those in Fig. 4-12. The difference of the curves labelled (A), (D) and (E) in Fig. 4-17 is not so large; however, in Fig. 4-12, we can see the different heating mechanism for (A), (D) and (E) (namely, the resonance conditions with $k_{\parallel} \cdot v_{\parallel} > 0$ and $k_{\parallel} \cdot v_{\parallel} < 0$) as well as their particle motions in the real space.

Now, as one of the applications of Fig. 4-10, we analyze the axial profile of hot electrons as follows:

(1) In Figs. 4-18(a) and (b), soft X-ray axial profiles with various energy ranges are shown. (Using these X-ray signals in the midplane, the same value of T_{eh} as compared with the X-ray PHA (see Fig. 4-4) is obtained.¹²) The ratio of the signal intensity obtained with a thick absorber to

the signal intensity obtained with a thin absorber becomes large as B increases along the axis (compare a solid curve with a dotted curve in Fig. 4-18(a) or (b)). This energy dependence in the axial direction, namely the higher energy electrons produced at the higher field side, is consistent with the graphic prediction in the θ vs Ω_e/ω plane (Fig. 4-10(b)); that is, the higher energy electrons couple the resonance conditions with the smaller values of θ . This allows the higher energy electrons to reach the higher magnetic field side along their bounce orbits.

(2) The temporal evolution of soft X-ray signals with a 1 mm iron absorber which has its 90% transmissivity at 250 keV (Fig. 4-18(c)) shows that they begin to be observed at the lower field side and thereafter they appear at the higher field side. This feature is explained in Fig. 4-10(b): in order to satisfy the second harmonic resonance conditions continuously, it is necessary to decrease the θ -value due to pitch angle scattering to values suitable for wave-particle interaction as described earlier (Fig. 4-10(b)). To satisfy the electron acceleration conditions for producing the higher energies (a few hundred keV), smaller values of θ are required. Such a temporal expansion of θ to the smaller values results in the expansion of the X-ray signals in the axial direction according to the relation between θ and B (electron bounce motion formula). This is consistent with the data in Fig. 4-18(c).

(3) The above mechanism effected by pitch angle

scattering also explains the temporal evolution of E_{\max} in Fig. 4-5(g), where the increment of E_{\max} tends to become small as E_{\max} increases.

(4) For the electrons with a maximum energy of 250 keV at $t = 6-9$ ms (Fig. 4-5(g)), the resonance condition is satisfied in the range $\theta = 42^\circ$ (at $\Omega_e/\omega = 0.5$) to $\theta = 54^\circ$ (at $\Omega_e/\omega = 0.55$) (see Fig. 4-10(b)). Electrons with these values return at the turning points at $B = 1.1$ T and 0.84 T. However, as shown in Fig. 4-18(c), the soft X-rays with a 1 mm iron absorber appear at $t \approx 7$ ms when viewing at the region where $B = 0.91$ T. At that time, soft X-ray emission from the regions where $B = 0.96$ T and 1.06 T is still undetectable. This suggests that the maximum value of θ ranges $49^\circ-51^\circ$ at $B = 0.55$ T from the formula for bounce motions, and hence these θ -values are in the region described by Fig. 4-10(b) as explained above (namely, from $\theta = 42^\circ$ to 54°). Therefore, the values of θ estimated from these two X-ray detection methods in Figs. 4-5(g) and 4-18(c) may be explained consistently by using Fig. 4-10(b).

Next, we discuss the possibility of third harmonic ECH using the θ vs Ω_e/ω plane. The resonance conditions in eq. (4-4) for both $n = 2$ and 3 along the same bounce motion are satisfied in the region of $51.5^\circ \leq \Theta \leq 66.3^\circ$ and $128 \text{ keV} \leq W \leq 192 \text{ keV}$, as shown by the hatched region in Fig. 4-16. To satisfy the resonance conditions successively with increasing W in this overlapped region, a different direction of Θ between $n = 2$ and 3 is seen in Fig. 4-16; for increasing W , Θ should become small under second

harmonic resonance conditions, while θ should become large under third harmonic resonance conditions. This difference between $n = 2$ and 3 is easily seen from the θ vs Ω_e/ω plane. The resonance conditions for $n = 3$ within the microwave lobe is shown in Fig. 4-19 by using eqs. (4-4)-(4-6). For the overlapped resonance region of $128 \text{ keV} \leq W \leq 192 \text{ keV}$, the different coupling behaviors between $n = 2$ and 3 are seen: second harmonic resonance conditions in this region are characterized by negative slopes of solid curves in the θ vs Ω_e/ω plane (resonance conditions with $k_{\parallel} \cdot v_{\parallel} > 0$ in Fig. 4-10(b)), while third harmonic resonance conditions are characterized by positive slope solid curves (resonance conditions with $k_{\parallel} \cdot v_{\parallel} < 0$ in Fig. 4-19(a)). These different characteristics result in the important difference in the electron energy dependence on θ for satisfying the resonance conditions. Thus, similar to the discussions of the axial X-ray profiles, a different axial electron energy dependence is expected. The third harmonic resonance conditions with $k_{\parallel} \cdot v_{\parallel} > 0$ are satisfied only when $W \geq 250 \text{ keV}$; this energy range is higher than the values obtained by X-ray measurement (see Fig. 4-5(g)). For $n = 3$, Fig. 4-19(a) ($k_{\parallel} \cdot v_{\parallel} < 0$) predicts locations of higher energy electrons to be in the lower field side. As described above, the experimental result of the axial X-ray energy distribution in Fig. 4-18 reflects the characteristic features of the resonance conditions with $k_{\parallel} \cdot v_{\parallel} > 0$; that is, if the third harmonic resonance condition with $k_{\parallel} \cdot v_{\parallel} < 0$ becomes the dominant heating mechanism, the higher energy

electrons should exist at the lower field side. This contradicts the experimental results on the axial intensity ratio of X-rays in Figs. 4-18(a) and (b).

Furthermore, the delay of the appearance of X-rays at the higher field side (Fig. 4-18(c)) as well as the temporal increase of E_{\max} indicates a temporal decrease of θ . This is contrary to the prediction for $n = 3$, since the higher energy electrons at $n = 3$ should be accelerated at the lower field side, as described earlier.

Under these experimental conditions, these results confirm that the dominant heating mechanism for the production of hot electrons is the second harmonic heating.

Finally, it is noted that the representation on the θ vs Ω_e/ω plane is also applicable to the other types of the magnetic field configurations. The resonance conditions in Figs. 4-10 and 4-19 (solid curves) are the same in any type of plasma devices; the only modification in this figure is the change of electron motion (dashed curves) according to each magnetic field configuration of the devices.

Chapter 5. Researches of MCP and SSB Detector Energy Response Using Synchrotron Radiations for Plasma Diagnostics

In tandem mirror devices, X-ray studies in the energy range from a few tens eV to a few keV are indispensably useful for clarifying essential roles of a thermal barrier^{11, 12, 45} in its thermal isolation effect between the central cell and the plug cell plasmas.¹³

In order to clarify these important issues, precise calibration experiments of X-ray detectors in this energy range are indispensable. Observations of X-ray detection characteristics of MCPs have been carried out in the 0.6 to 82 keV energy range.⁴⁶⁻⁴⁸ However, in spite of the importance of the energy range below 0.6 keV, data only at some discrete photon energies are currently available.⁴⁹ Even if we use these useful data points, it is difficult to interpolate the MCP response characteristics throughout this region without ambiguity. Therefore, it is of great importance to add detailed response data to those previous works. Also, it would give useful information for application of MCPs as the detector of a grazing incidence spectrometer⁵⁰ or a crystal spectrometer.^{51, 52}

In §5-1-1, we report the current response of MCPs (η_{MCP}) as a function of X-ray energy and incident angle for the energy range from 0.06 to 0.6 keV. In this section, the MCP response for the wide X-ray energy range from 0.06-80 keV would be completed (also see ref.10-13); this

range may cover most of the interesting region for plasma experiments.

Furthermore, the energy response of the SSB detector (η_{SSB}) is studied as well. Its theoretical calculation using thicknesses of a silicon depletion layer, a dead layer, and an electrode is the only way to estimate the efficiency. In this estimation, we cannot help including ambiguity from numbers of different published data on the mass absorption coefficients of the detector materials⁵³⁻⁵⁵ as well as from a nominal value of the dead layer thickness. Also, in our recent paper, a complicated response characteristic of an extended X-ray absorption fine structure (EXAFS) near the absorption edge of the SSB detector composition was reported.⁴⁷ Furthermore, a recent paper has pointed out a serious result that the depletion layer thickness is not the critical parameter in determining the X-ray sensitive region of SSB detectors; in particular, for photons above several keV.⁵⁶

Under these complicated situations, it would be useful to demonstrate experimentally obtained detection efficiency of an SSB detector along with the comparison with the theoretically calculated efficiency. For this purpose, our experiments and analyses have been carried out. The experiments for the SSB detector have been made using continuous X-ray radiation in the energy range from 0.056 to 0.9 keV.⁵⁷

In order to clarify our computation processes, the mass absorption coefficient data used for the analyses are

shown.

The calibration experiment has been carried out by using synchrotron radiation at the Photon Factory of National Laboratory for High Energy Physics. Radiation in XUV and soft X-ray energy region is supplied at the beam line having a 2-m grasshopper monochromator (BL-11A).⁵⁷ The beam line consists of a deflecting mirror, a pre-focusing mirror, a grasshopper grazing incidence monochromator with a fixed incident angle of 88° , a refocusing mirror, a beam monitor and X-ray filters (Fig.5-1). The pre-mirror system has a grazing incident angle of 2° ; this eliminates the radiation above 2 keV because of its low reflectivity. The concave grating of 1200 grooves/mm, whose blaze wavelength is 33.3 \AA , has been used. The energy of output beam is 50 eV to 1 keV. The energy resolution is 0.5 to 1 eV at 250 eV for the nominal slit width in our experiment. The beam monitor is a gold mesh-type photodiode. In order to suppress stray and higher order radiation, four different thin filters (Cu, Ag, C and Be) have been used. A Cu filter is used for X-rays of 400 eV to 950 eV energy, a Ag filter for 180 eV to 420 eV, a C filter for 100 eV to 290 eV and a Be filter for 60 eV to 115 eV. Radiation from the beam line has been fed to the detector chamber where MCPs, SSB, or a gold photodiode is set. Each photo-current from these detectors as well as the beam monitor has been measured by using an electrometer, and the output voltage has been converted into digital pulses by a V/F converter. Then the output pulses have been counted by a scaler with 1 s of

accumulation and processed by a microcomputer. This computer is also used for automated control of the monochromator so as to change photon energies.

The MCPs have been mounted on a rotatable stage to change the incident angle of X-rays. The MCPs have been operated under the condition of the unsaturated current-detection mode. The gold photocathode (more than 1 μm thick) is mounted in an NBS-type diode with a cylindrical anode.^{47, 58} This is placed at the end of the chamber, and utilized for calibration of the incident photon flux.

The photon beam size at the detector position is 1 mm \times 4 mm; this size is small enough as compared with each detector size. Thus, all of the beam is incident on the active surfaces of the detectors.

The detector chamber is pumped down to 1×10^{-6} torr by using a turbomolecular pump. The pressure of the storage ring is maintained below 1×10^{-9} torr during the operation.

5-1 MCP Energy Response

In Fig. 5-2 is shown the bias voltage dependence of output currents of the MCPs at the 800 eV photon energy. The output current increases exponentially with the bias voltage increasing up to 10 nA. The MCP current of 10 nA under this experimental condition corresponds to the current density of 250 nA/cm² which is 10% of the strip current. For this type of MCPs, the output current which is less than 7% of the strip current is guaranteed for the linear response. This characteristic is explained by potential disturbances near the end of MCP output due to an increase of the strip current which supplies the electrons released from the channel wall. In other words this indicates that the MCP gain increases exponentially with increasing the bias voltage in the unsaturated region. During this experiment the bias voltage or the slit width of the beam-line spectrometer has been controlled so as to maintain the MCP current under a 10 nA level.

The experimental results of the normalized detection current of I_{MCP}/I_0 and I_{Au}/I_0 give the energy response of I_{MCP}/I_{Au} for the normalized incident photon intensity. Here, I_{MCP} denotes the detection current of the MCPs. Also, I_{Au} and I_0 are photocurrents from the gold photodiode and the gold-mesh beam monitor, respectively. The current response of the MCPs has been calculated from I_{MCP}/I_{Au} multiplied by the gold photoelectric yield data.

In Fig. 5-3 are shown the quantum yield data of $QE(E)$

for gold photocathodes, which are based on the Day et al. data.⁵⁸ Here, it is noted that no data are available for the 0.3-0.5 keV region in their paper. They, however, have recommended the use of the formula of $QE(E) = \mu(E) \times E \times f(E)$ ^{47, 59}; here, $f(E)$ is a slowly varying function, which is related to the efficiency of converting primary photon energy into secondary electrons, as introduced by Henke et al.⁵⁹ The values of $\mu(E) \times E$, which are the incident photon energy deposition near the photocathode surface, are given by the Henke et al. data.⁵⁵ According to the recommended curve of $f(E)$ by Day et al.,⁵⁸ the $QE(E)$ data used here are completed as shown by the solid curve in Fig.5-3. It is noteworthy that $QE(E)$ in Fig.5-3 has also been used for analyzing the quantum efficiency of the SSB detectors. The experimental data and the theoretical calculation on SSB agree well (see §5-1-2).

Using these data, the current response of MCPs has been obtained as shown in Fig.5-4 for the photon energy from 60 eV to 600 eV. The data have been taken for the case of normal incidence to the MCP surface; therefore, the incident angle of photons to the channel axis is 13° (the bias angle of the MCPs). The general feature of the MCP current response curve is summarized as follows: there is a maximum around 100 eV. The response decreases with increasing the photon energy beyond 150 eV as a whole, except the structures originated from the absorption edges of constituent elements of MCP glass material. In particular, the O K-edge structure is very clear

accompanying an EXAFS-like oscillatory structure similar to the Si K-edge structure reported previously.^{47, 48} The penetration length of photons in this energy range is estimated to be in the order of 1000 Å for the MCP glass. The range of electrons produced through absorption of X-rays is less than 1000 Å in the glass material. Therefore, the surface composition of the MCP glass throughout a channel wall would strongly affect the MCP response. It is considered that the surface of channel wall consists of a SiO₂ layer of 100 Å thick, whose bulk side composition is lead glass.^{49, 60} The measured MCP response might be qualitatively explained from the surface composition in a channel wall, that is, there are a small jump above Si L_{2,3}-edge (100.6 eV), a strong jump near the O K-edge energy (531.7 eV) and a hump around 400 eV which is considered to correspond to the Pb N-edge (413 eV).

It should be mentioned about a jump near C K-edge (283.8 eV) energy because carbon is not the explicit ingredient of MCP glass. A possible origin of carbon is a rare impurity included in anode material or some contamination on the MCP channel wall.⁴⁹ In this energy range the surface composition of a channel wall is sensitive for the response of MCP. Provided that the surface of channel wall which consists of a SiO₂ layer of 100 Å thick is covered with a thin carbon layer,⁶⁰ one can estimate the thickness of carbon layer from the experimental response curve. The response is considered to be nearly proportional to the absorption of X-rays in the

surface region, where X-rays impinge on a channel wall with the grazing angle of 13° . From the absorption characteristics below and just above C K-edge, a 30 Å thick carbon layer on the SiO_2 layer can explain the jump ratio of 1.6 at the edge. The incident angle dependence of the MCP response has also been investigated in this energy range. The $\cot \theta$ dependence has been confirmed. Here, θ is an incident angle to the channel axis. This dependence agrees with the photoelectric response of a cylindrical photocathode at large angles ($|\theta| > \theta_c$), where θ_c is a critical angle of reflection of X-rays from the surface of the channel.⁴⁶ The surface layer of a channel wall is essential to X-ray detection by MCPs in the energy range from 60 eV to 600 eV.

The precise current response curve has been completed for the wide X-ray energy range from 0.06 keV to 82 keV (Fig.5-5), combined with the previously reported data.⁴⁶⁻⁴⁸ It is clarified that MCPs are sensitive to X-rays in this wide energy range; that is, the variation in the MCP response remains within about one order of magnitude. A brief summary of the response characteristic is described as follows: In hard X-ray region a rather large hump is observed around 20 to 30 keV; in XUV and X-ray region the response decreases as a whole with photon energy from 0.1 keV to 5 keV, except jumps and humps at the edge energies of C, O, Si, Ba and Pb.

In addition to these data, the response would decrease and vanish finally with decreasing the photon energy from

XUV to VUV region (about 2000 Å),⁶¹ since the MCP response is based on a secondary electron emission process. Thus, it is required to investigate the MCP response for continuous spectrum of photon energy below 0.06 keV so as to clarify the low energy limit of the MCP response.

From a viewpoint of a practical use of the MCPs, their high gain and good sensitivity in such a wide energy range is quite attractive and suitable for measuring X-rays from high-temperature plasmas or from electrons having a broad energy distribution function.

From these experimental results, absorption methods using MCPs in a wide energy range are expected to be quite attractive because of the above-mentioned characteristics. Figures 5-5 and 5-6 show the detection efficiency of MCPs as a function of photon energy and a Maxwellian electron temperature, respectively; these are calculated from eq. (3-1) (η_{SSB} being replaced by η_{MCP}) using various absorbers as explained in §3-2-3. Similarly to the SSB detector (as described §3-2-2), T_e is estimated with MCP by changing the absorbers. The MCP detectors in the central cell and the plug region are utilized for temperature measurements as well as their spatial profile observation using tomographic reconstructions.

5-2 SSB Energy Response

The detection efficiency data of the SSB detector for a unit incident photon flux, η_{SSB} , are plotted by the dots in Fig. 5-7 (see eq. (3-2)). Also, the result from theoretical calculations is depicted by a dashed curve. Here, the relative values of the data are normalized to the theoretical curve at $E = 0.07$ keV. These experimental data are obtained from a similar method to the η_{MCP} -observation. The relative value of η_{SSB} is calculated from I_{SSB}/I_{Au} multiplied by $QE(E)$ of gold. Here, I_{SSB} denotes the detection current of the SSB detector, and the $QE(E)$ data we used are shown in Fig. 5-3.

In addition to the above notice of $QE(E)$ for the 0.28-0.53 keV region, we carefully compare the two values of $QE(E)$ from Day et al.⁵⁸ and Henke et al.⁶² for the 0.20-0.28 keV region; the former curve has a sharp curvature change near 0.22 keV but the latter shows a smoothly increasing feature. In Fig. 5-7, two values of η_{SSB} in the 0.20-0.28 keV region are presented with the labels of D and H; these correspond to the data from Day et al. and from Henke et al., respectively. Therefore, in our paper, the $QE(E)$ values of gold are based on the Day et al. data from 0.05 keV to 0.9 keV; also, the $QE(E)$ data from Henke et al. are utilized for the 0.20-0.28 keV region as well.

A theoretical model for the detection efficiency of SSB detectors is briefly described in the following:
Incident photons onto an SSB active area are partially

absorbed by its aluminium electrode as well as the dead layer; the transmitted photons through these layers are absorbed in the Si depletion layer and create electron-hole pairs depending on the photon energy. These charged particles are biased and detected in a form of electric currents. Equation (3-2) has been widely used in calculations of η_{SSB} .^{17, 47, 56, 63} Therefore, it is useful to compare the experimental data with the theoretical results from eq. (3-2).

The calculated values from eq. (3-2) are found to be quite sensitive to the substituted values of μ . Therefore, it is necessary to depict the values of μ used in our calculations (Fig. 5-8). The data from Biggs and Lighthill⁵³ are used for Si (0.05-0.9 keV) as well as for Al (0.05-0.1 keV). Also, the data on Al (0.1-0.9 keV) including detailed structures are supplied from a large amount of database which are carefully collected by Saloman, Hubbell and Scofield⁵⁴; from the database, the semiempirical values of Henke et al. are used here. The Henke et al. data for O (0.05-0.9 keV) are also utilized.^{54, 55}

Using these data on μ as well as the parameters of the SSB detector, η_{SSB} in eq. (3-2) is calculated and shown by a dashed curve in Fig. 5-9 as well as in Fig. 5-7 for comparison with the experimental data. In Fig. 5-9, the solid curve labelled A is calculated using the silicon depletion layer parameter alone (under the assumptions of no dead layer and no electrode). The curve A is plotted as a straight line; this means no transmission of incident

photons through the depletion layer for the 0.05-1 keV energy range. The solid curve labelled B is obtained by the use of the parameters of the 100 Å dead layer and the depletion layer. Here, no electrode is assumed. This curve B shows the effects of the dead layer on the incident photon absorption for the energies below 0.3 keV as well as for the energies near the oxygen K edge (581.7 eV). These three curves indicate that a dominant contribution to η_{SSB} comes from the Al data (the electrode thickness data as well as the μ database for Al.)

Now, we proceed the comparison between the experimental results and the theoretical calculations (see again Fig.5-7). As a whole, the experimental data points agree well with the theoretical curve except a detailed structure near the Al absorption edges. For the 0.01-0.17 keV region, an oscillatory behaviour in μ for Al (Fig.5-8) seems to be reflected in the general feature of the data but some absolute value-deviations.

One of the most interesting behaviours in η_{SSB} may be found for the 0.07-0.10 keV region: Near the Al L_{II} (73 eV) and L_{III} (72 eV) absorption edges, a sharp edge structure of η_{SSB} is seen, and the height of the jump in η_{SSB} agrees quite well with the theoretical estimation. The next sharp jump near the Al L_I absorption edge (87 eV), however, is not expected by the calculations. Also, it is noted that this sharp edge is accompanied by an oscillatory structure.

This behaviour in the energy range from 80 eV to 110 eV is expanded in Fig.5-10. In our previous paper, similar

structure in the SSB detection currents has been reported near the Si K edge (1.838 keV)⁴⁷; in that case, the oscillatory structure continues for more than a few hundreds eV. Therefore, that structure may be classified as an EXAFS. In this case of Al L₁ edge, however, the oscillatory structure exists from E = 87 eV to about 100 eV (or at most up to E = 150 eV). This oscillatory behaviour in the energy range just above the absorption edge (Fig. 5-10) would rather be classified as an X-ray absorption near edge structure (XANES). This structure implies that the following phenomena may occur within the thin Al electrode regime: Low energy wave functions which represent ejected photoelectrons are easily multi-scattered by their surrounding electrons or atoms because of low transmissivity of these low energy photoelectron waves. Thus, such an oscillatory behaviour in η_{SSB} may be interpreted by the interference between the photoexcited wave function and the scattered wave function including the multi-reflection effects.

From these complicated phenomena near absorption edges, it is noted that a careful notice for selecting a detector should be necessary for detailed X-ray experiments; the ingredients of the detector materials should be carefully chosen so as not to have its absorption edges within an important energy range for the experiments.

Chapter 6. Observation of the Thermal Barrier Effects on the Central Cell and Plug Electrons Using the X-ray Detectors

6-1 Observation of Thermally-Isolated Electron Distribution Functions in the Central Cell and the Plug Region due to the Thermal Barrier

In this section, we report (i) the first observation of the formation of a plateau electron distribution function in the plug using the Si(Li) detector, the pure Ge detector as well as the 50 channel MCP. In addition, (ii) our previous experiments merely suggested a transition tendency from the weak to the strong ECH scaling with increasing ϕ_b , since the two theories did not provide the values with clear differences for the limited range of the ϕ_c vs ϕ_b -data¹³ (most data being at $\phi_b \leq 0.7$ kV). Here, we report a wider range of the data ($\phi_b \leq 1.2$ kV), which show a clear discrepancy from the weak ECH scaling in the high ϕ_b -region. These potential data again support the strong ECH scaling as observed with the X-ray diagnostics. Furthermore, (iii) the first direct observation of the thermal isolation effect³⁹ due to a kV-range thermal barrier is reported by showing a large difference in X-ray spectra between the central cell and the plug. These new findings give a clear picture of the thermal isolation effect due to ϕ_b as well as the plug electron heating process according to the strong ECH theory for a kV-range ϕ_c -formation. ϕ_c ,

ϕ_b and the plug electron confining potential ϕ_{pb} ($= \phi_c + \phi_b$) are measured with ELAs¹³ and a E||B end-loss-ion spectrometer (ELIS) from TMX-U¹³ as well as heavy ion (Au^0)-beam probes.^{13, 64}

In Fig. 6-1 are plotted the scaling data on ϕ_c vs ϕ_b with the ratio of the plug to the central cell densities $n_p/n_c = 0.30-0.55$ using ELAs (●) and ELIS (○). The data are now compared with the calculated results from the weak (dotted curves) and the strong (solid curves) ECH theories. As compared with our previous results,¹³ Fig. 6-1 clearly shows a transition from the weak through the intermediate,⁶⁵ and then to the strong ECH prediction with increasing ϕ_b . From these ECH theories, this transition is accompanied by the change in f_p from Maxwellian to the plateau distributions, since a remarkable thermal isolation effect due to the ϕ_b -increase causes an efficient heating of plug-localized electrons with drastically reduced collisions. Therefore, our next important issue is the observation of f_p in this high ϕ_b region. The axial configuration of ϕ_b , ϕ_c and ϕ_{pb} is depicted in Fig. 3-1(c). In Fig. 6-2 is shown a schematic drawing of f_p resulting from the strong ECH theory.²⁰ This velocity space is divided into three regions: the ϕ_{pb} -trapped electrons are confined in the regime P, where the plateau electrons are bounded by an ellipsoidal separatrix.²⁰ The Maxwellian electrons trapped by the plug/barrier mirror with a temperature $T_{p,m}$ are located in the region M; these electrons are heated by both plug and barrier ECH. The

electrons in the region L are lost from the plug/barrier cell through the loss-cone with an angle $\theta_0 = 35^\circ$.

The X-ray PHA data in the plug are presented with the Si(Li) detector (Fig. 6-3(a)). The data are taken during plug-ECH (potentials are formed as shown in Fig. 3-1(c)), as well as at 5 ms after plug-ECH is switched off (ϕ_{pb} has already decayed to be 0, but the other heating systems are still being injected). A remarkable feature is a quick decay of the X-rays at $h\nu \leq 5$ keV (in this case, $2\phi_{pb} = 5.4$ kV) as compared with $\phi_{pb} = 0$. However, a higher energy component continued to at least 7 keV does not change in each case. The data with the pure Ge detector are shown in Fig. 6-3(b) for the observation of such higher energy X-rays ($h\nu \geq 5$ keV). Almost the same spectra in each case of ϕ_{pb} are again obtained (for simplicity, a spectrum for $2\phi_{pb} = 5.4$ kV alone is presented there). Also, these spectra from the high energy electron component observed with both detectors consistently show the same electron temperature of 60 keV.

For the X-ray spectrum analyses, using eq. (4-1), the X-rays emitted to the detector angle^{4,1} are calculated using various plateau distribution functions depending on ϕ_{pb} (see Fig. 6-2) as well as relativistic Maxwellians^{1,2} with various T_{em} and θ_0 . Line radiation from both K and L shells^{6,6} is not observed in Fig. 6-3(a); hence, impurities in the plasmas are ignored for the analyses (see more detail in ref. 18).

X-ray observations with an NaI(Tl) detector in the

barrier region^{1,2} show an electron temperature of 60 keV as comparable to $T_{p,m}$. These 60-keV electrons observed in both barrier and plug regions support the existence of the plug/barrier mirror-trapped electrons as predicted in the region M (Fig. 6-2). Even after the ϕ_{pb} -decay, such mirror-trapped high energy electrons are maintained because of their low collisionality as seen in Figs. 6-3(a) and (b).

While, intense X-rays from the lower energy component below 5 keV are observed only when ϕ_{pb} is formed (Fig. 6-3(a)). The spectrum is fitted using the calculated results from relativistic Maxwellian distributions; however, dotted curves with 2 keV and 1 keV can fit the data ranging up to 2.5 keV alone, and exceeding 2.5 keV alone, respectively. Also, any Maxwellian combinations can never fit the spectrum with $d(\ln\{h\nu \cdot dn/d(h\nu)\})/d(h\nu) (= \xi) < 0$, since Maxwellian electrons always emit the photon spectra with $\xi > 0$ as seen by these dotted curves. While, such a spectrum with $\xi < 0$ is one of the remarkable X-ray characteristics from plateau electron distribution functions. A solid curve in Fig. 6-3(a) is calculated using f_p in Fig. 6-2; here, we use the data of $2\phi_{pb} = 5.4$ kV for the potential-trapped plateau electrons along with the mirror-trapped Maxwellian with a 35° loss-cone ($T_{p,m} = 60$ keV and its density ratio is 3% to the total n_p). (The intensity of electron-electron Bremsstrahlung is less than two-orders of magnitude as compared with electron-ion Bremsstrahlung (Fig. 6-4).) This fitting is based on the fact that dominant X-rays come from hot core plasmas. More

detailed analyses taking account of $\phi_{pb}(r)$ are carried out using f_p in Fig.6-2: A line integrated intensity at $h\nu$ with the X-ray PHA, $I_{XP}(h\nu)$, is written as

$$I_{XP}(h\nu) = \int [n_e \cdot n_i \cdot Z^2](r) \cdot I_{XC}(h\nu, r) dr.$$

Here, $I_{XC}(h\nu, r)$ denotes the calculated result at a radius r for an X-ray energy $h\nu$ using the ϕ_{pb} -profile in Fig.6-5(a). The product of $n_e \cdot n_i \cdot Z^2$ at r is obtained from tomographic reconstructed X-ray emissivity at r , $I_{XT}(r)$, which is corrected by the absorber transmissivity and the MCP-response, $10^{-4.6} - 10^{-4.8}$, 67 divided by $\int I_{XC}(h\nu, r) d(h\nu)$, since $I_{XC}(h\nu, r)$ is normalized for unit values of n_e , n_i and Z . Thus, $I_{XP}(h\nu)$ is described by

$$I_{XP}(h\nu) = \int \left\{ \frac{I_{XT}(r)}{\int I_{XC}(h\nu, r) d(h\nu)} \right\} \times I_{XC}(h\nu, r) dr.$$

The data from X-ray tomography for $I_{XT}(r)$ as well as the data on $\phi_{pb}(r)$ for calculating $I_{XC}(h\nu, r)$ (see Figs.6-5 and 6-6), therefore, predict the spectrum of $I_{XP}(h\nu)$ (the broken curve in Fig.6-3(a)). Good agreement between the data and the calculation in Fig.6-3(a) indicates the validity of the strong ECH theory, which predicts the model in Fig.6-2. Here, the individual values of n_e , n_i and Z are not necessary for the above analyses, since they are replaced by the tomography data.

Another independent method of comparing the X-ray data with the calculated X-rays from the plateau distributions requires the assumptions of a low- Z (or a radially uniform- Z) condition and of a small contribution of high energy electrons to the total X-rays (thereby, $n_e = n_i$ is

used); these are satisfied as described above. Now, we can calculate the X-ray profiles with various thickness absorbers from $\int [n_e \cdot n_i \cdot Z^2](r) \cdot I_{xc}(h\nu, r) d(h\nu)$ (solid curves in Fig. 6-5(b)). Here, we use $\phi_{pb}(r)$ and the model in Fig. 6-2 as well as n_e -profile deduced from X-ray data with a 1.8- μ m polypropylene absorber (sensitive to $n_e \cdot n_i \cdot Z^2$ but insensitive to ϕ_{pb} ; see ref. 12 and Fig. 6-7); this profile is consistent with those with microwave interferometers in the barrier and the central cell mapped along magnetic lines of force to the plug). Good agreement between the X-ray profile data and the calculations in Fig. 6-5(b) again proves the validity of the strong ECH-plateau formation theory.

The final issue in studying this model is whether these plateau electrons are isolated by the thermal barrier and trapped in the plug (also, see §6-2). In Fig. 6-8 are compared the absorption characteristics of the central cell X-rays (●) with those of the plug X-rays (○) at $r = 0$ in Fig. 6-5(b). The central cell data are fitted by the 0.15-keV Maxwellian bulk electrons along with high energy electrons (4 keV and 5% to the total n_e). Here, the bulk electron-collision time of 30 μ s and no-ECH power in the central cell may form this Maxwellian distribution. Also, the high energy electrons are detected with ELAs; they may be explained by ECH-driven loss-electrons through the loss-cone in the plug region,⁶⁵ since they appear during the plug-ECH injection period only.

Such a remarkable electron energy difference between

the two regions has shown the first demonstration of the thermal isolation effect due to a 1-kV range thermal barrier (see more detail in the next section). Furthermore, different shapes of distribution functions are separated by the thermal barrier; these difference include the information on the isolation of the ϕ_{pb} -trapped plug electrons as well.

6-2 Improvement of the Central Cell Electron Confinement due to the Thermal Barriers

In this section, the first observation of both temporal and spatial increase in T_e due to the ϕ_b -formation is reported; this would demonstrate the usefulness of the thermal barrier^{13, 23, 68} not only for the ϕ_e -enhancement but for the improved electron confinement.

In this section, the temporal and spatial evolution of T_{ec} is measured with the 50 channel MCP using X-ray tomographic reconstruction techniques.¹⁸ The values of T_{ec} are estimated from the X-ray absorption method^{7, 12, 45} using polypropylene and polyester absorbers. While, plug electron energies are observed using X-ray PHA with the Si(Li) detector and the pure Ge detector as well as the X-ray tomography with the 50 channel MCP. As shown in §6-1, the plug electrons form the plateau-shaped distribution function. For giving information on the averaged plug electron energy, we employ a parameter, E/N , where E is the total energy of the plateau electrons and N is the total electron number. This value of E/N becomes $1.5 \cdot T$ for purely Maxwellian electrons without any boundaries. In the case of a flat distribution within such a ellipsoidal boundary for the plug electrons, E/N becomes ϕ_{pb} . Therefore, we define an effective plug temperature $\langle T_{ep} \rangle$ as $\phi_{pb} / 1.5$ for the convenience of comparing it with T_{ec} . We also use the results of the measurements of end-loss-ion currents, $I_{ELA-ion}$, and end-loss-electron currents, I_{ELA-e} , detected

with the above-described ELAs.

In Fig.6-9 is shown the temporal evolution of the plasma parameters; during the period of thermal barrier formation ($5 \text{ ms} \leq t < 30 \text{ ms}$), the ϕ_c -formation results in the reduction of $I_{\text{ELA-ion}}$ and thereby the associated increase in n_e .¹³ A remarkable feature during the thermal barrier period is the temporal increase in T_{ec} as well as the contrary decrease in $\langle T_{ep} \rangle$ as similarly behaved to ϕ_{pb} . This behaviour of $\langle T_{ep} \rangle$ may be explained as follows: These potential trapped plug electrons are confined within the boundary as determined by ϕ_{pb} ;²⁰ that is, the maximum velocity for the ϕ_{pb} -trapped electrons equals to $2(\phi_{pb}/m)^{1/2}$. Therefore, the sustainment of these plug electrons is strongly affected by the ongoing variation of the ϕ_{pb} -value, and thereby $\langle T_{ep} \rangle$ immediately follows the ϕ_{pb} -evolution as seen in Fig.6-9.

On the other hand, the central cell electrons may be controlled by the thermal isolation effect due to ϕ_b . The electron confinement characteristics are estimated from the ratio of the confined electrons due to ϕ_b to the total. If we assume the validity of the similar treatment for these ϕ_b -confined electrons as compared to the ϕ_c -confined ions,¹³ then the Pastukhov theory²⁴ becomes a guiding principle to discuss the central cell electron confinement under our experimental condition without the ECH injection in the central cell. In Fig.6-9, the value of ϕ_b/T_{ec} ranges more than 2-3 during the thermal barrier period. Under this condition, most electrons are estimated to be confined due

to ϕ_b .²⁴ Therefore, central cell electrons may bounce between the thermal barriers. During their transitions through the central cell, there is a possibility to be heated through an energy relaxation process from the ICH-produced hot ions (~ 1 keV); also, a plug-ECH driven warm electron component (~ 4 keV) falling into the loss cone connected to the central cell is another candidate to heat the electrons. Such an increase in T_{ec} through these energy relaxation processes during the ϕ_b -formed period alone is expected only when the improvement of these electron confinement is achieved.

In Fig. 6-10 is shown the change in the radial profile of T_{ec} ; here, T_{ec} is compared in the cases with (\circ) and without (\bullet) the ϕ_b -formation. In these data, we again observe the T_{ec} -increase in the region with $\phi_b/T_{ec} \gtrsim (2-3)$ alone. It is noted that the plug-ECH driven warm electrons continue to exist beyond this region down to the outer radii (Fig. 6-10), hence a heating source may exist at broader radial positions as compared with the electron heated region. Also, end-loss-ions at these broader radii are heated due to ICH even when a simple mirror period;¹³ this suggests the ICH power is not localized in the T_{ec} -increased region.

Such a temporal and spatial increase of T_{ec} in the region with $\phi_b/T_{ec} \gtrsim (2-3)$ alone may also suggest the improvement of the central cell electron confinement due to the thermal barriers.

In Fig. 6-11, a data set under non-thermal barrier

(unplugged) operational conditions is shown for comparison with the thermal barrier shot data in Fig.6-9. A remarkable difference between the two data is characterized by the fact that the temporal evolution of T_{ec} in Fig.6-11 follows the T_{ep} -variation. This behaviour of T_{ec} shows a good thermal connection from the central cell through the barrier region to the plug location under the non-thermal barrier conditions. (A little temperature difference between the two (less than a hundred eV) may be due to the effect of the mirror trapped electrons in the plug/barrier mirrors, where ECH power is being injected, since this difference is lost within their collision time after the ECH power is switched off.) Thus, the data comparison between the two different conditions for ϕ_b supports the improvement of the central cell electron confinement due to the ϕ_b -formation.

These data in Figs.6-9 - 6-11 have consistently shown the first demonstration of a temporal and spatial T_{ec} - increase during the thermal barrier period ($\phi_b/T_{ec} \geq (2-3)$). This gives important information on the improvement of the electron confinement due to the thermal barriers.

Chapter 7. Summary

(I) *Experimental results on hot electron production in the barrier region and its physical mechanism studies are summarized as follows.*

(1) The characteristic properties of the hot electrons are T_{eh} -saturation at about 60 keV with $E_{max} \approx 250$ keV ($t = 10 - 20$ ms) under typical operational conditions, and a successive increase of n_{eh} even after the T_{eh} -saturation. These properties indicate this hot electron production method is desirable for the thermal barrier formation along with maintaining MHD stability, since thermal barrier potential formation requires a large fraction of n_{eh} to the total density^{11, 12, 29} and the T_{eh} -saturation maintains a low beta value in the axisymmetric barrier mirror configuration.

(2) The electron heating process is depicted in the newly introduced θ vs Ω_e/ω plane; the T_{eh} -saturation is explained by the spatially localized microwave absorption with a finite $N_{||}$ on the basis of second harmonic resonance conditions, corrected for the effects of relativistic mass variation and Doppler shift.

The figures in the θ vs Ω_e/ω plane clearly show the difference of the resonance conditions affected by the parallel and the antiparallel electron motions with respect to the direction of $k_{||}$ of the incident microwave.

These figures indicate the dominant mechanism of the T_{eh} -saturation is due to the resonance conditions with

$k_{\parallel} \cdot v_{\parallel} < 0$, while E_{\max} is limited by the resonance conditions with $k_{\parallel} \cdot v_{\parallel} > 0$ for the pitch angle scattering of high energy electrons (Figs. 4-10 - 4-15).

(3) The axial energy distribution of the X-rays is investigated. An increasing fraction of the higher energy electron population is observed towards the higher field side. This is explained by Fig. 4-10(b) for $n = 2$; this also shows that the resonance conditions for $n = 3$ are not a dominant process for the high energy electron production.

(4) The representation in the θ vs Ω_e/ω has an advantage to know the electron behaviours in a real space which is characterized by the magnetic field intensity of Ω_e/ω or B , as compared with a usual momentum space representation. For instance, degenerated resonance conditions in the momentum space are clearly distinguishable in this θ vs Ω_e/ω plane, which gives information on the spatially distributed (real space) electrons particularly for their diagnostics. Also, this representation plane is widely applicable to the other types of devices by replacing the bounce motion by the electron motions in their magnetic field configurations.

(III) Detailed X-ray energy responses of MCP and SSB detectors are studied for the precise electron energy measurements in the central cell and plug region. Widely applicable new data are obtained as follows:

(1) The characteristics of MCPs for X-ray detection have been investigated with continuous X-ray energy variation using synchrotron radiation in the XUV and soft

X-ray region (from 60 eV to 600 eV). The current response data have shown EXAFS near the oxygen K absorption edge as well as a jump structure near the silicon L-edge; these structures are explained by the surface composition of channel walls (SiO_2). Also, the incident angle dependence of current response has been found to agree with the cylindrical photocathode model. The precise current response curve has been completed for the wide X-ray energy range from 0.06 keV to 82 keV combined with our previously reported data. These data show that MCPs have quite suitable characteristics particularly for the bulk electron (< 1 keV) measurements.

(2) Using synchrotron radiation from 0.056 to 0.900 keV, the detection efficiency of SSB detector, η_{SSB} , has been investigated. The experimental data are compared with the theoretically calculated results using the detector parameters of the depletion layer, the dead layer and the electrode. As a whole, the data points agree well with the theoretical results except an oscillatory structure for the 0.07-0.17 keV region. In this energy region, sharp edge structures in η_{SSB} are observed near the Al L_{II} and L_{III} absorption edges as well as the Al L_I edge. In particular, this structure in η_{SSB} near the Al L_I edge is accompanied by an oscillatory behaviour like an XANES on the high energy side of the edge.

/// Thermal isolation effects due to the thermal barriers are investigated.

(1) The data in Figs. 6-5 - 6-7 have consistently shown

the first demonstration of a temporal and spatial T_{ec} - increase during the thermal barrier period alone ($\phi_b/T_{ec} \geq (2-3)$). This gives important information on the improvement of the electron confinement due to the thermal barriers.

(2) The first observation of a plateau-shaped plug electron distribution function for the potential (ϕ_{pb})-trapped electron energy regime has been obtained using the X-ray PHA and tomography data. Also, mirror-trapped hot electrons in the same energy level as the 60-keV barrier electrons have been observed. These data along with the scaling relation between ϕ_c and ϕ_b for a kV-range have shown the validity of Cohen's strong ECH theory for the ion confining potential enhancement.

(3) From these X-ray data, the first clarified observation of the thermal isolation effect due to the kV-range thermal barrier has been obtained along with the differences of the electron distribution functions in the thermally isolated regions of the central cell and plug location separated by the thermal barrier.

Acknowledgments

The author would like to express her sincere gratitude to Prof. S.Miyoshi for his continuous encouragement as well as important discussions and suggestions.

Special thanks to Dr. T.Cho for his valuable discussion and kind suggestion.

The author wishes to thank the members of the GAMMA 10 group for their collaboration, especially Profs. K.Yatsu, D.Tsubouchi and Drs. Y.Kiwamoto, A.Mase, M.Inutake, H.Hojo, N.Yamaguchi, T.Saito, A.Itakura, K.Ishii, M.Ichimura, I.Katanuma and Y.Nakashima.

The author also thanks Drs. T.Kato and K.Masai at Nagoya University, and Dr. K.Ogura at Niigata University as well as Dr. T.Kondoh at Japan Atomic Energy Research Institute for their useful discussions.

The author would like to acknowledge the staff of the Photon Factory for the operation of the storage ring in the calibration experiment of X-ray detectors. This experiment has been performed under the approval of the Photon Factory Advisory Committee (Proposal No.87-164).

Finally, the author's sincere thanks are expressed to Ms. H.Hirata and Messrs K.Okawa, A.Sugiyama, Y.Washo, H.Itoh and Y.Endoh for their supports as well as to Messrs E.Takahashi, A.Osawa, H.Sugawara, K.Hayashi and K.Koganezawa for their collaboration.

References

1. V. V. Alikaev et al. ; Sov. J. Plasma Phys. 2 (1976) 212.
2. R. M. Gilgenbach et al. ; Phys. Rev. Lett. 44 (1980) 647.
3. M. Sato et al. ; Nucl. Fusion 23 (1983) 1333.
4. T. Cho et al. ; J. Phys. Soc. Jpn. 53 (1984) 187.
5. R. M. Gilgenbach et al. ; Nucl. Fusion 21 (1981) 319.
6. S. Kubo et al. ; Phys. Rev. Lett. 50 (1983) 1994.
7. T. Cho et al. ; Nucl. Fusion 26 (1986) 349.
8. A. Ando et al. ; Phys. Rev. Lett. 56 (1986) 2180.
9. T. Sato et al. ; in Plasma Phys. and Controlled Nucl. Fusion Research 1986 (Proc. 11th Int. Conf. Kyoto, 1986), Vol. 2, IAEA, Vienna (1987) 343.
10. M. Inutake et al. ; Phys. Rev. Lett. 55 (1985) 939.
11. Y. Kiwamoto et al. ; Phys. Fluids 29 (1986) 2781;
12. T. Cho, N. Yamaguchi, T. Kondoh, M. Hirata, A. Mase, Y. Kiwamoto, A. Hirose and S. Miyoshi; in Plasma Science (Proc. 13th IEEE Int. Conf. Saskatoon, 1986), IEEE, New York (1986) 83;
T. Cho, T. Kondoh, M. Hirata, A. Sakasai, N. Yamaguchi, A. Mase, Y. Kiwamoto, A. Hirose, K. Ogura, S. Tanaka and S. Miyoshi; Nucl. Fusion 27 (1987) 1421.
13. T. Cho et al. ; J. Phys. Soc. Jpn. 56 (1987) 3775;
T. Cho, M. Inutake, K. Ishii, I. Katanuma, Y. Kiwamoto, A. Mase, Y. Nakashima, T. Saito, N. Yamaguchi, K. Yatsu, M. Hirata, T. Kondoh, H. Sugawara, J. H. Foote and S. Miyoshi, Nucl. Fusion 28 (1988) 2187.
14. G. E. Guest et al. ; Nucl. Fusion 27 (1987) 1245.

15. G. R. Smith et al. ; Phys. Fluids 30 (1987) 3633.
16. A. M. Cormack; J. Appl. Phys. 34 (1963) 2722;
35 (1964) 2908.
17. S. Tsuji et al. ; Nucl. Fusion 22 (1982) 1082;
25 (1985) 305.
18. T. Kondoh, T. Cho, M. Hirata, N. Yamaguchi, T. Saito,
Y. Kiwamoto and S. Miyoshi; submitted to J. Appl. Phys.
19. R. H. Cohen et al. ; Nucl. Fusion 20 (1980) 1421;
23 (1983) 1301.
20. R. H. Cohen; Phys. Fluids 26 (1983) 2774.
21. G. I. Dimov et al. ; Sov. J. Plasma Phys. 2 (1976) 326.
22. T. K. Fowler et al. ; Comments on Plasma Phys. and
Controlled Fusion 2 (1977) 167.
23. R. F. Post; Nucl. Fusion 27 (1987) 1579.
24. V. P. Pastukhov; Nucl. Fusion 14 (1974) 3.
25. D. E. Baldwin et al. ; Phys. Rev. Lett. 43 (1979) 1318.
26. T. C. Simonen et al. ; in Plasma Phys. and Controlled Nucl.
Fusion Research 1984 (Proc. 10th Int. Conf. London, 1984),
Vol. 2, IAEA, Vienna (1985) 255.
27. D. P. Grubb et al. ; Phys. Rev. Lett. 53 (1984) 783.
28. R. S. Post et al. ; in Plasma Phys. and Controlled Nucl.
Fusion Research 1986 (Proc. 11th Int. Conf. Kyoto, 1986),
Vol. 2, IAEA, Vienna (1987) 251.
29. I. Katanuma et al. ; Phys. Fluids 29 (1986) 4138.
30. P. J. Catto et al. ; Phys. Fluids 26 (1983) 2161.
31. T. F. Straton; "X-ray Spectroscopy" in *Plasma Diagnostics*,
edited by W. Lochte; (North-Holland, 1968).

32. S. von Goeler et al. ; "X-ray Diagnostic for TFTR" in *Diagnostic for Fusion Reactor Conditions*, edited by P. E. Stott et al. ; (International School of Plasma Physics, Varenna, Italy, 1, 1982).
33. T. Kato; IPPJ-AM-4 (1978).
34. K Masai; *Astro Physics and Space Science* 98 (1984) 367.
35. W. Heitler; in *The Quantum Theory of Radiation*, (The Oxford Univ. Press, 1954)
36. W. J. Karzas et al. ; *J. Suppl.* VI (1961) 167.
37. P. J. Brussaard et al. ; *Rev. Mod. Phys.* 34 (1962) 507.
38. T. Yuyama et al. ; *J. Phys. Soc. Jpn.* 53 (1986) 2027.
39. T. Cho et al. ; in *Plasma Phys. and Controlled Nucl. Fusion Research 1986* (Proc. 11th Int. Conf. Kyoto, 1986), Vol. 2, IAEA, Vienna (1987) 243.
40. H. Bethe et al. ; *Proc. R. Soc. (London)*, Ser. A146 (1934) 83.
41. R. L. Gluckstern et al. ; *Phys. Rev.* 90 (1953) 1026; 1030.
42. G. Elwert; *Ann. Phys.* 34 (1939) 178.
43. A. Hakkenberg et al. ; *Physica* 30 (1964) 2147.
44. T. D. Rognlien; *Phys. Fluids* 26 (1983) 1545.
45. M. Hirata, T. Cho, T. Kondoh, N. Yamaguchi and S. Miyoshi; *Jpn. J. Appl. Phys.* 28 (1989) 96.
46. T. Kondoh, N. Yamaguchi, T. Cho, M. Hirata, S. Miyoshi, S. Aoki, H. Maezawa and M. Nomura; *Rev. Sci. Instrum.* 59 (1988) 252.
47. T. Cho, N. Yamaguchi, T. Kondoh, M. Hirata, S. Miyoshi, S. Aoki, H. Maezawa and M. Nomura; *Rev. Sci. Instrum.* 59 (1988) 2453; 60 (1989) 2337.

48. N. Yamaguchi, T. Cho, T. Kondoh, M. Hirata, S. Miyoshi,
et al.; Rev. Sci. Instrum. 60 (1989) 368; 2307.
49. G. W. Fraser; Nucl. Instrum. Methods 195 (1982) 523.
50. J. L. Schwob et al.; Rev. Sci. Instrum. 58 (1987) 1601.
51. B. P. Duval et al.; Rev. Sci. Instrum. 57 (1986) 2156.
52. Z. M. Koenig; Rev. Sci. Instrum. 59 (1988) 1813.
53. F. Biggs et al.; *Analytical Approximations for X-ray
Cross Sections III* (Sandia Report)
SAND 87-0070 UC-34 (1988).
54. E. B. Saloman et al.; At. Data Nucl. Data Tables 38 (1988)
1.
55. B. L. Henke et al.; At. Data Nucl. Data Tables 27 (1982) 1.
56. K. W. Wenzel et al.; Rev. Sci. Instrum. 59 (1988) 1380.
57. M. Yanagihara et al.; KEK Report 84-17 (1984).
58. R. H. Day et al.; J. Appl. Phys. 52 (1981) 6965.
59. B. L. Henke et al.; J. Appl. Phys. 48 (1977) 1852.
60. P. J. Bjorkholm et al.; Proc. SPIE 106 (1977) 189.
61. C. Martin et al.; Appl. Opt. 21 (1982) 4206.
62. B. L. Henke et al.; J. Appl. Phys. 52 (1981) 1509.
63. E. D. Fredrickson et al.; Rev. Sci. Instrum. 59 (1988) 1797.
64. K. Ishii et al.; Rev. Sci. Instrum. 56 (1985) 1053.
65. R. H. Cohen et al.; in Proceedings of International School
of Plasma Physics (Varenna, 1987) 1187.
66. K. Masai et al.; Nature 330 (1987) 235; 335 (1988) 804.
67. M. Hirata et al.; submitted to Rev. Sci. Instrum.
68. N. Hershkowitz et al.; Nucl. Fusion 28 (1988) 1333.

Figure Captions

Fig. 3-1 Schematic view of tandem mirror GAMMA 10;

(a) magnet coil set; (b) magnetic flux tube with heating systems; (c) axial magnetic field and potential profiles.

Fig. 3-2 Schematic view of the barrier region with magnetic field lines and mod-B surfaces. Thick solid curves and thick dashed curves denote the surfaces with $B = 5$ kG and 5.5 kG, respectively. The microwave lobe is bounded by the dotted lines.

Fig. 3-3 Schematic view of soft X-ray pulse height analysis systems in the barrier region; (a) with a pure germanium (Ge) detector; (b) with a sodium iodide (NaI(Tl)) detector.

Fig. 3-4 Efficiency of the pure Ge detector as a function of incident X-ray energy.

Fig. 3-5 Efficiency of the NaI(Tl) detector as a function of incident X-ray energy.

Fig. 3-6 Schematic view of soft X-ray pulse height analysis system with a pure Ge detector and a Silicon (Lithium) (Si(Li)) detector in the plug region.

Fig. 3-7 Efficiency of the Si(Li) detector as a function of incident X-ray energy.

Fig. 3-8 Schematic view of a silicon surface barrier detector system in the central cell.

Fig. 3-9 Efficiency of the SSB detector with various X-ray absorbers as a function of incident X-ray energy.

Fig. 3-10 Output intensities of the SSB detector are shown as a function of Maxwellian electron temperature T_e for the use of various X-ray absorbers noted in the figure.

Fig. 3-11 Relative intensity versus thickness of polyester absorber calculating from various Maxwellian distribution functions with T_e .

Fig. 3-12 Schematic view of temporally and spatially resolved soft X-ray detection system with the microchannel plate (50 channels) for observation of the radial and axial profiles in barrier region.

Fig. 3-13 Schematic view of the 50 channel MCP system in the plug region.

Fig. 3-14 Schematic view of the 50 channel MCP system in the central cell.

Fig. 4-1 Comparison of soft X-ray spectra obtained with the pure Ge detector (a) and the NaI(Tl) detector (b), fitted by curves of a Maxwellian distribution function taking into account the relativistic mass variation, with $T_{eh} = 50$ keV and $55^\circ \leq \theta \leq 125^\circ$; the relativistic Born approximation corrected by the Elwert factor is used.

Fig. 4-2 Calculated curves from eq. (4-1) as a function of (a) T_e and of (b) θ_0 .

Fig. 4-3 Temporal evolution of soft X-ray energy spectra with the NaI(Tl) detector. The fitted curves are similar to those shown in Fig. 4-1. The plasma parameters are summarized in Fig. 4-5.

Fig. 4-4 X-ray spectra for a total of 5, 10, 40 shots obtained with the NaI(Tl) detector. Dashed curves are calculated from the Maxwellian distribution function with $T_{eh} = 50$ keV; the relativistic Born approximation corrected by the Elwert factor is used.

Fig. 4-5 Typical data set in the barrier region; (a) hot electron temperature from Fig. 4-3; (b) data obtained with a diamagnetic loop; (c) calculated density results for (a) and (b), taking into account the soft X-ray radial profile obtained

with the 50 channel MCP; (d) line density measured with the microwave interferometer; (e) n_{b0} obtained by using the measured line density and the radial profile data; (f) calculated ratio of n_{eh0} to n_{b0} ; (g) observed maximum photon energy as shown in Fig. 4-4; (h) l_b as obtained with the 50 channel MCP, showing FWHM of $\sqrt{I_{sx} - A_{b0} l_b}$. $p_b = 1.1 \times 10^{-7}$ torr, in H_2 at $t = 10$ ms.

Fig. 4-6 Comparison of data sets for (a) $p_b = 8.0 \times 10^{-8}$ torr and (b) $p_b = 2.0 \times 10^{-6}$ torr; in H_2 at $t = 10$ ms.

Fig. 4-7 Pressure dependence of; (a) n_{b0} (\circ) and $\Delta\Phi_{dia}$ (\bullet), (b) T_{eh} (\circ) and n_{eh}/n_{b0} (\bullet), and (c) I_{ELA} from the core plasma (\circ) and $n_e \cdot l_e$ (\bullet), at $t = 15$ ms.

Fig. 4-8 (a) $\Delta\Phi_{dia}$ and (b) T_{eh} plotted as a function of n_{b0} at $t = 6.5$ ms (Δ) and $t = 15$ ms (\circ), in the range of $p_b < 3 \times 10^{-6}$ torr; \bullet and \blacktriangle in (a) are the data for $p_b > 7 \times 10^{-6}$ torr.

Fig. 4-9 Temporal evolution of (a) T_{eh} , (b) $n_b \cdot l_b$, and (c) $\Delta\Phi_{dia}$, for $P_{ECH} = 130$ kW (solid curve), $P_{ECH} = 70$ kW (dash-dotted curve), and $P_{ECH} = 40$ kW (dotted curve).

Fig. 4-10 Solid curves indicate the second harmonic resonance

conditions, taking into account the Doppler shift due to (a) $k_{\parallel} \cdot v_{\parallel} < 0$ and (b) $k_{\parallel} \cdot v_{\parallel} > 0$ for various values of W in the θ vs Ω_e/ω plane. Dashed curves indicate electron bounce motions for various values of θ in the case without ECH. The intersections of the solid curves with the dashed curves satisfy the resonance conditions of eq. (4-4). For instance, the electrons with $W = 61$ keV satisfy their resonance conditions in the hatched region alone in (b). It is noted that two different values of Ω_e/ω (points C and D in (b)) satisfy the resonance condition for $W = 40$ keV along the bounce motion labelled p-q.

Fig. 4-11 An example of the calculation process of ECH; an electron (2 keV, $\theta = 50^\circ$ at the midplane) moving along the bounce motion labelled (a) is accelerated to $W = 4$ keV with increasing θ ; it then moves along the bounce motion (b) until the solid curve of the resonance condition for $W = 4$ keV intersects the curve (b). At the intersection, the electron is accelerated again and then moves along the bounce orbit (c) until the next resonance condition for $W = 6$ keV is satisfied.

Fig. 4-12 Examples of electron heating process (heating characteristic curve) in the θ vs Ω_e/ω plane, according to eq. (4-4). Electrons with initial

conditions of $W_i = 2$ keV and $\theta_i = 44^\circ, 70^\circ, 0^\circ, 38^\circ, 38.5^\circ$ at $\Omega_e/\omega = 0.5$, are heated to final states of $(W_f, \theta_f) = (61.0$ keV, $72.6^\circ)$, $(26.2$ keV, $78.4^\circ)$, $(26.0$ keV, $67.3^\circ)$, $(38.2$ keV, $71.5^\circ)$, $(61.2$ keV, $72.5^\circ)$ along the curves labelled (A)-(E). The dashed curves show the final bounce orbits after the resonance conditions disappear. (The dashed curve (A') shows the bounce orbit after the electron heating along curve (A) is finished.) In (c), the resonance conditions with $k_{\parallel} \cdot v_{\parallel} > 0$ and $k_{\parallel} \cdot v_{\parallel} < 0$ are satisfied several times in the lower part (depicted by a black region). Electron energies during the heating processes are easily obtained by superposing Fig. 4-10 on Fig. 4-12. The point M during the heating process (A) is an example; its corresponding point M in Fig. 4-10 gives the electron energy of 4 keV as well as its angular information of $\theta = 60.1^\circ$.

Fig. 4-13 Example of the heating process including the deceleration process. Here, this process is emphasized by $\Delta W = -2$ keV, whereas the acceleration with $\Delta W = 0.2$ keV is assumed. The same initial condition for the curve (A) in Fig. 4-12 is used. Nearly the same values of W_f and θ_f are obtained, compared with the curve (A).

Fig. 4-14 W_f as a function of θ_i with $W_i = 1$ keV (\circ), 2 keV (\bullet), 4 keV (\triangle) and 20 keV (\square). The points (A)-(E) correspond to W_f of the curves (A)-(E) in Fig. 4-12, respectively.

Fig. 4-15 An example of the heating processes to produce the electron with 250 keV. The dot-dashed curve is the final bounce orbit of the case (A) in Fig. 4-12. The successive electron heating occurs if pitch angle scatterings result in the following new initial conditions; the initial conditions and final values due to ECH for each heating process ($W_i, \theta_i; W_f, \theta_f$) are (a) (61 keV, 67° ; 86.8 keV, 69.3°); (b) (86.8 keV, 62.5° ; 119.2 keV, 65.1°); (c) (119.2 keV, 57.5° ; 157.8 keV, 60.3°); (d) (157.8 keV, 52.5° ; 202 keV, 55.3°); (e) (202 keV, 47.5° ; 251.6 keV, 50.3°). Along the curves (a)-(e), no pitch angle scattering is assumed until the resonance conditions disappear along each heating process, since longer pitch angle scattering time is expected compared with the heating time.

Fig. 4-16 The second and third harmonic resonance conditions within the microwave lobe ($\Omega_e/\omega = 0.5-0.55$), mapped on the normalized momentum space by $m_0 \gamma c$ at $\Omega_e/\omega = 0.5$. The regions bounded by the solid and dashed curves satisfy the resonance conditions with $\mathbf{k}_\parallel \cdot \mathbf{v}_\parallel < 0$ and $\mathbf{k}_\parallel \cdot \mathbf{v}_\parallel > 0$, respectively. A

hatched region shows the overlapped regime between second and third harmonic resonance conditions. $p_{\parallel} = p \cdot \cos\Theta$ and $p_{\perp} = p \cdot \sin\Theta$. It is noted that the two resonance locations for $W = 40$ keV (points C and D in Fig. 4-10(b)) are mapped on the single degraded point labelled E.

Fig. 4-17 The projection of heating processes of the curves (A)-(E) in Fig. 4-12 to the momentum space at $\Omega_e/\omega = 0.5$. W_r as a function of θ_r with $W_i = 2$ KeV (dot-dashed line) and 20 keV (dashed line).

Fig. 4-18 Axial profiles of X-ray intensities observed with the 50 channel MCP at (a) $t = 10$ ms and (b) $t = 20$ ms. The open circles are the data using the $50 \mu\text{m}$ aluminum absorber and the filled circles are the data using the $7 \mu\text{m}$ aluminum absorber. (c) Temporal evolution of X-ray emission obtained with the 1 mm iron absorber, at $B = 0.91$ T (\circ), 0.96 T (\bullet) and 1.06 T (\square). $n_b \cdot l_b = 1.1 \times 10^{13} \text{ cm}^{-2}$. The temporal evolution of E_{max} is similar to that in Fig. 4-5. No plug ECH is injected in order to highlight the effect of the barrier ECH.

Fig. 4-19 Conditions for third harmonic resonance taking account of the Doppler shift of (a) $k_{\parallel} \cdot v_{\parallel} < 0$ and (b) $k_{\parallel} \cdot v_{\parallel} > 0$. The notation used is the same as in Fig. 4-10.

Fig. 5-1 Experimental setup with a 2-m grasshopper monochromator for the detection efficiency investigation of the MCPs and SSB detector.

Fig. 5-2 Bias voltage dependence of output currents of the MCPs. Bias voltage was applied between the input and output surfaces of the tandem MCP.

Fig. 5-3 The quantum efficiency of gold, $QE(E)$, used in this thesis. The data from Day et al.⁵⁸ are plotted by a solid curve from 0.05 to 0.9 keV; also, the data from Henke et al.⁶² is compared using a dashed curve for the 0.20-0.28 keV region.

Fig. 5-4 Current response of the MCPs as a function of the incident photon energy from 60 eV to 600 eV.

Fig. 5-5 Current response of the MCPs and the detection efficiency with various absorbers as a function of incident photon energy from 0.06 keV to 82 keV, combined with the previously reported data⁴⁶⁻⁴⁸ and Fig. 5-4.

Fig. 5-6 Output intensities of the MCPs are shown as a function of Maxwellian electron temperature T_e for the use of various X-ray absorbers noted in the figure.

Fig. 5-7 The detection efficiency data of the SSB detector (dots), η_{SSB} , as a function of the incident photon energy of E . The dashed curve is theoretically calculated values of η_{SSB} . The data points marked by D and H (0.20-0.28 keV) are calculated using the QE(E) data from Day et al. and from Henke et al., respectively (see fig. 5-3).

Fig. 5-8 The mass absorption coefficients of silicon, μ_{Si} , aluminium, μ_{Al} , and oxygen, μ_O ,⁵³⁻⁵⁵ used in the thesis for the calculations of the SSB detector efficiency.

Fig. 5-9 The results from the theoretical calculations for the SSB detection efficiency. A dashed curve is calculated using the parameters of the SSB detector (see eq. 3-2). The solid curve labelled A is a calculated result using the parameter of the Si depletion layer alone; also, the solid curve labelled B is calculated using both parameters of the depletion layer and the dead layer. The Al electrode thickness is not taken into account in these solid curves.

Fig. 5-10 The detection efficiency, η_{SSB} , ranging from 80 eV to 110 eV is expanded. A sharp jump of η_{SSB} at the Al L₁ absorption edge (87 eV) is accompanied by an oscillatory structure like an XANES.

Fig. 6-1 Scaling data on ϕ_c vs ϕ_b as compared with the ECH theories. These data are observed by the ELA and the Beam-Probe Groups.

Fig. 6-2 A model of an electron velocity distribution function due to the strong ECH theory (velocity space at the plug).

Fig. 6-3 (a) X-ray spectra for $2\phi_{pb} = 5.4$ kV and 0. Data are fitted by the plateau electron distribution function having $2\phi_{pb} = 5.4$ kV on axis with the ϕ_{pb} -profile data in Fig. 6-5(a) along with Maxwellian electrons (3% to the total n_p , 60 keV with a loss-cone angle of 35°) (the dashed curve). The contribution of the on-axis core electrons are shown by the solid curve. Also, the 60-keV Maxwellian electrons are observed in (b). For comparison, X-rays from Maxwellian electrons with 1 or 2 keV are shown by the dotted curves in (a).

Fig. 6-4 X-ray spectra calculated from the plateau electron distribution function having $2\phi_{pb} = 5.4$ kV. Both of the intensities of electron-ion Bremsstrahlung and electron-electron Bremsstrahlung are shown by the solid curve and the dashed curve, respectively.

Fig. 6-5 (a) Radial profile data on ϕ_{pb} . (b) X-ray radial profile data with two pieces of a $0.9\text{-}\mu\text{m}$

polypropylene (p.p) absorber (\circ), p.p. + 1.5- μ m polyester (p.e.) (\bullet), p.p. + 2- μ m p.e. (\square), and p.p. + 4- μ m p.e. (\blacksquare) are compared with the calculated X-ray profiles from the plateau electron distribution functions using the ϕ_{pb} - data in (a) (solid curves). The plasma radius in the plug denotes r_p .

Fig. 6-6 Tomographic reconstructed X-ray emissivity using two pieces of 0.9- μ m polypropylene absorber ($h\nu \geq 80$ eV). (The total thickness is 1.8- μ m.)

Fig. 6-7 The relative X-ray intensities taking account of the response of the 50 channel MCP are shown as a function of ϕ_{pb} for the use of various X-ray absorbers noted in the figure. Here, p.p. and p.e. mean the polypropylene and the polyester absorbers, respectively.

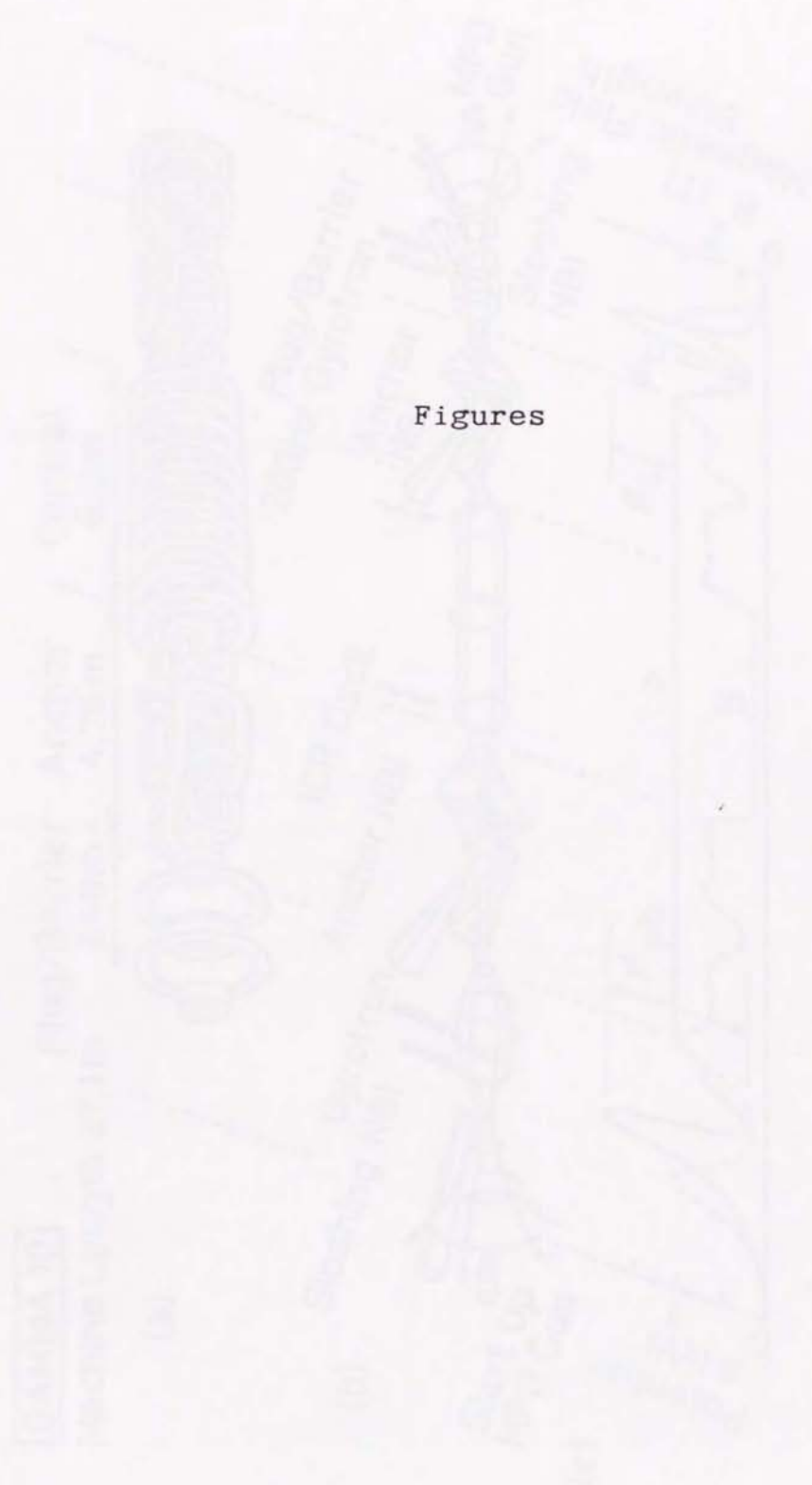
Fig. 6-8 X-ray tomography data ($r = 0$) in the plug (\circ) (see Fig. 6-5) and in the central cell (\bullet) are compared during the thermal barrier period. Here, $h\nu \geq 80$ eV. The plug data are fitted by the calculated results from the plateau electron distribution function having $2\phi_{pb} = 5.4$ kV (solid curve). The central cell data are fitted by the 0.15-keV Maxwellian bulk electrons along with high energy electrons (4 keV and 5% to the total n_e)

(dashed curve). Dotted curve is calculated from the 1 keV Maxwellian electrons.

Fig. 6-9 Temporal evolution of (a) the central cell line density, nl_c , (b) the ion end loss current observed with the ELAs, $I_{ELA-ion}$, (c) T_{ec} , (d) $\langle T_{ep} \rangle$, (e) ϕ_c , (f) ϕ_b , and (g) ϕ_{pb} under the thermal barrier operational conditions.

Fig. 6-10 Data comparison between the cases with (\circ) and without (\bullet) the ϕ_b -formation for (a) radial profiles of T_{ec} . When ϕ_b is formed, (b) the electron end loss current observed with the ELAs, I_{ELA-e} , as well as (c) ϕ_{pb} and ϕ_b are presented. (ϕ_b is estimated using the relation between ϕ_c vs ϕ_b (see Fig. 6-1).) The data are mapped into the central cell radius, r_c , along the magnetic lines of force.

Fig. 6-11 Temporal evolution of (a) nl_c , (b) $I_{ELA-ion}$, (c) T_{ec} , (d) T_{ep} , (e) ϕ_c , and (f) ϕ_b under non-thermal barrier (unplugged) operational conditions (except the short thermal barrier period during $t = 10-14$ ms).



Figures

Fig. 3-1

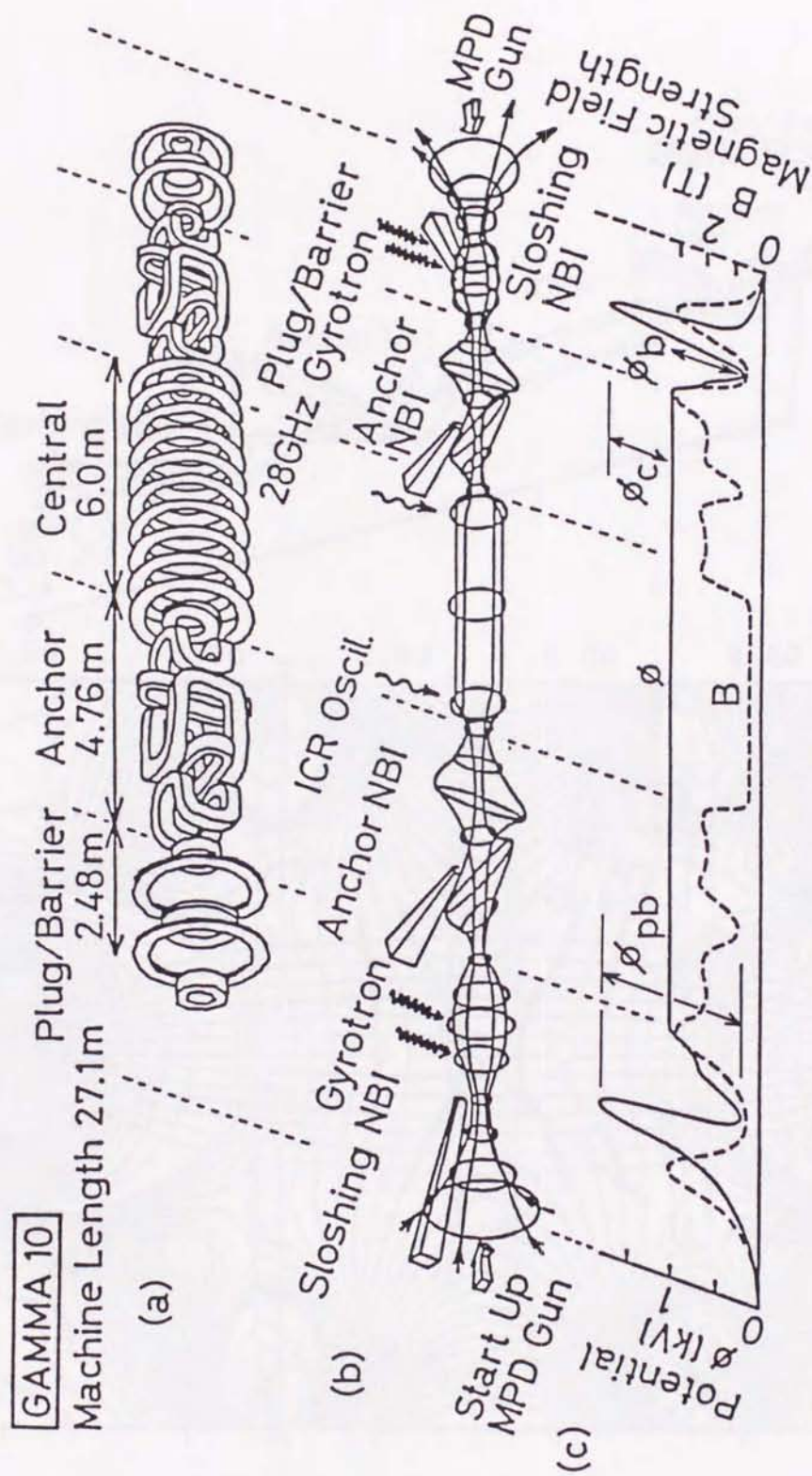


Fig. 3-1

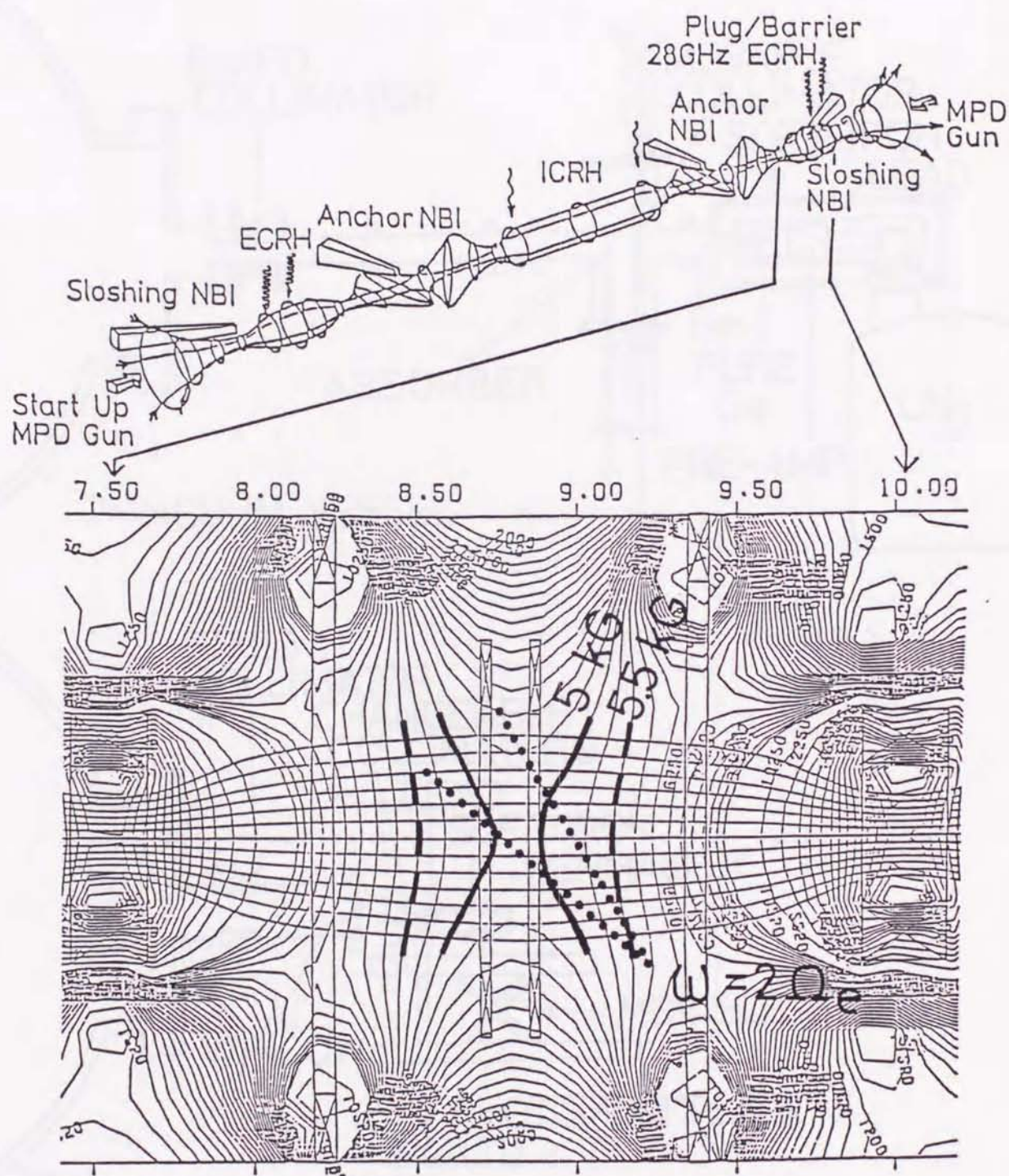


Fig. 3-2

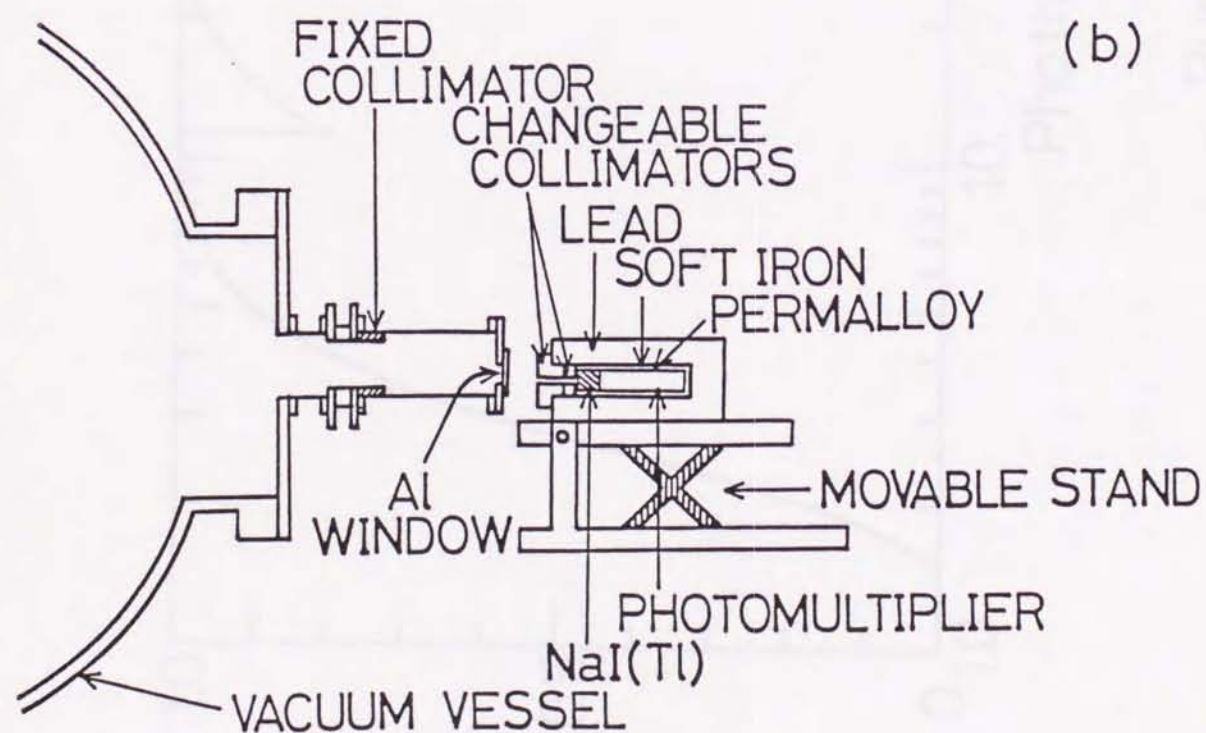
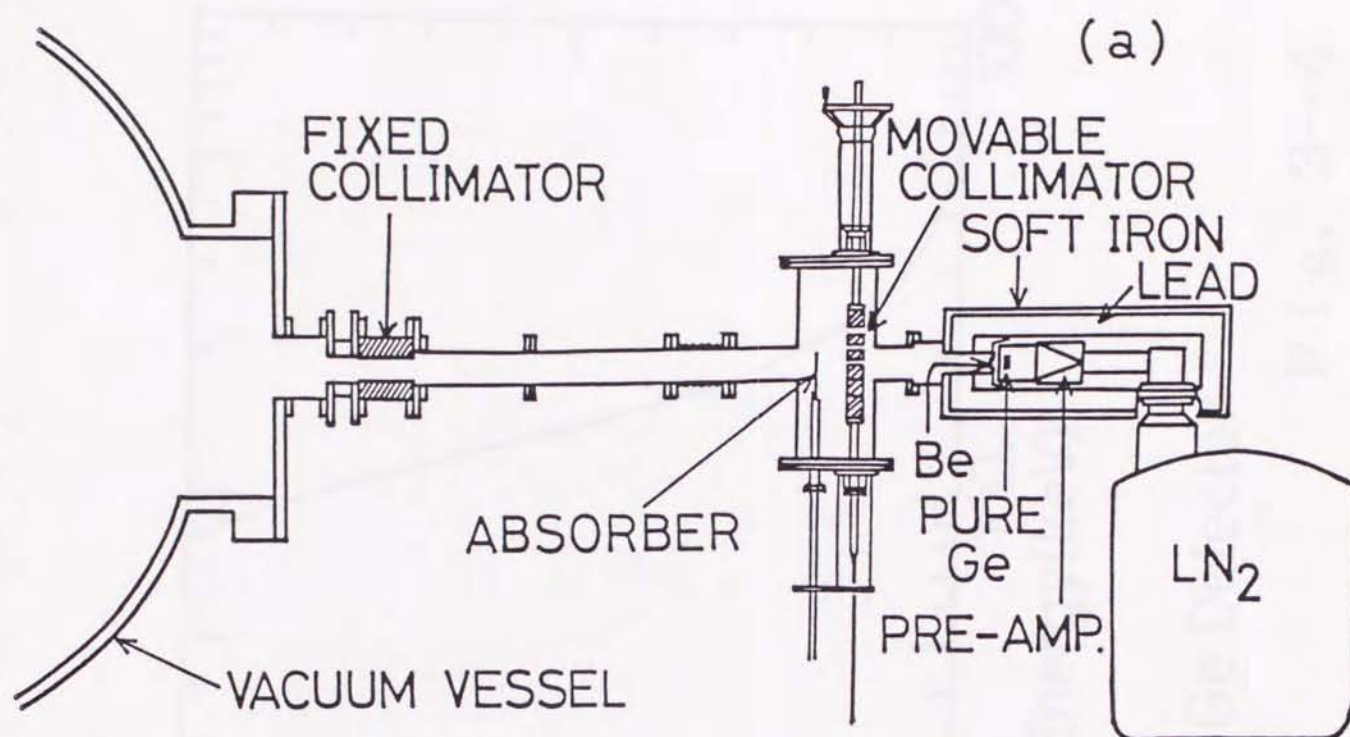
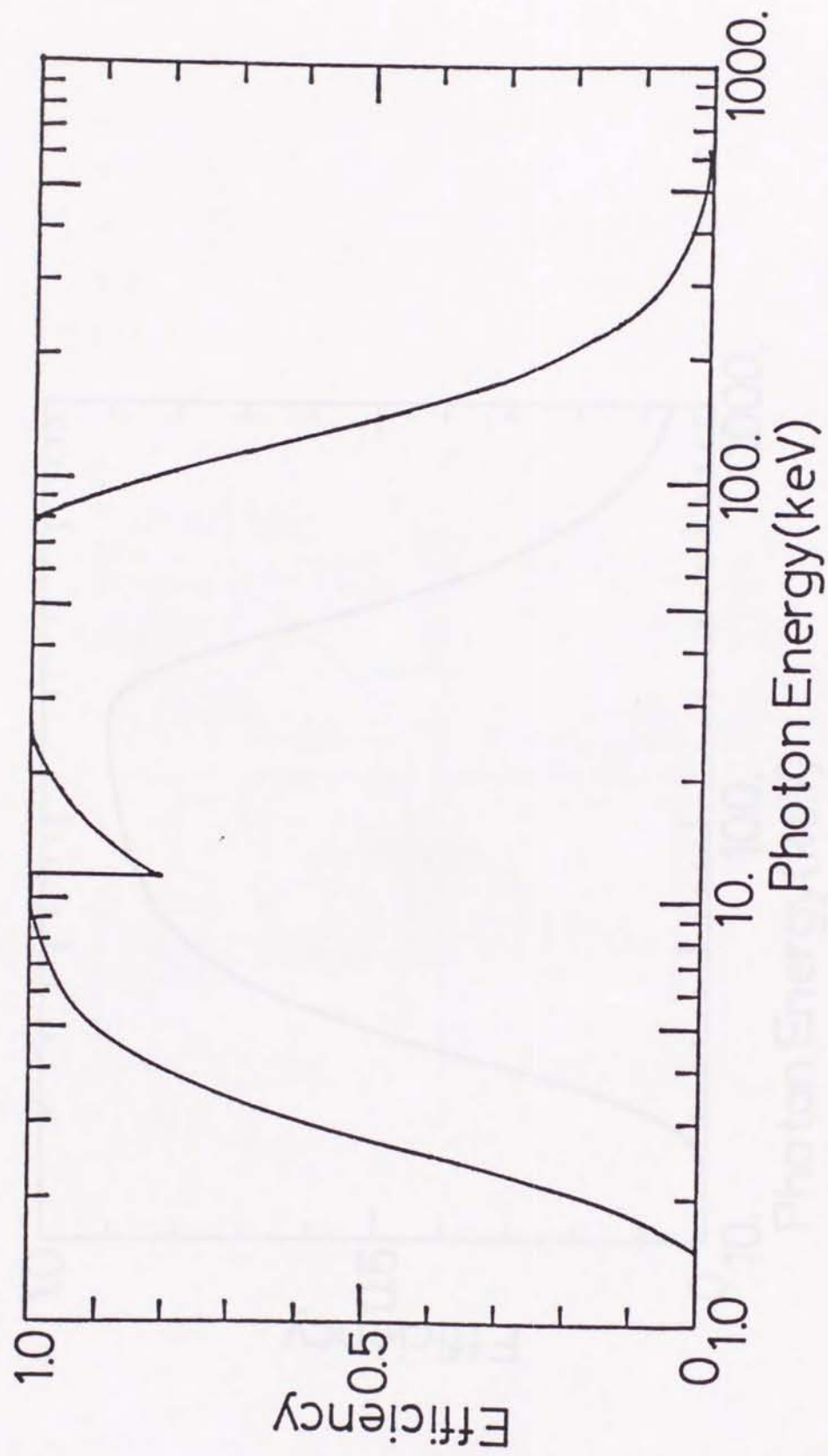


Fig. 3-3



Pure-Ge Detector

Fig. 3-4

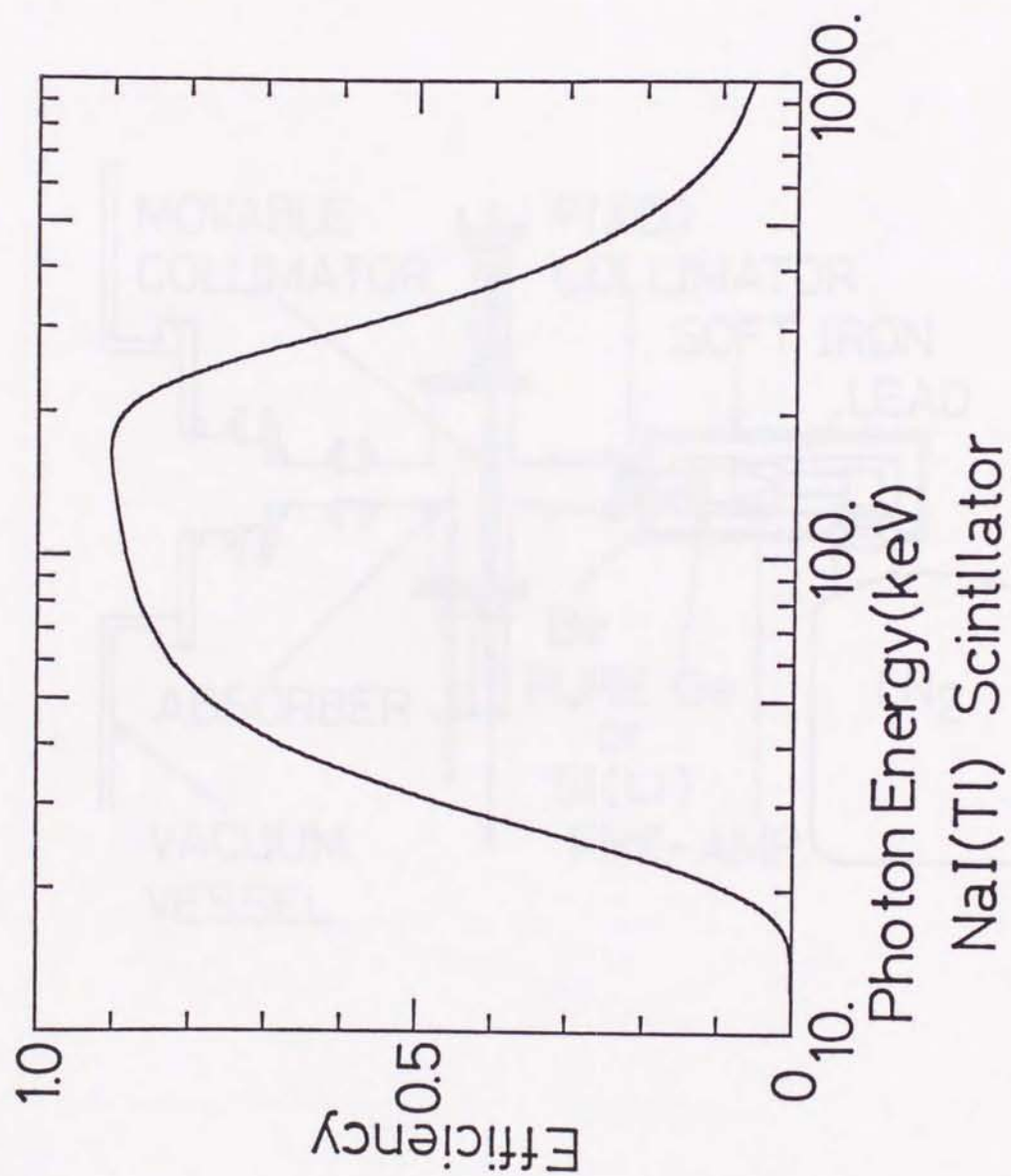


Fig. 3-5

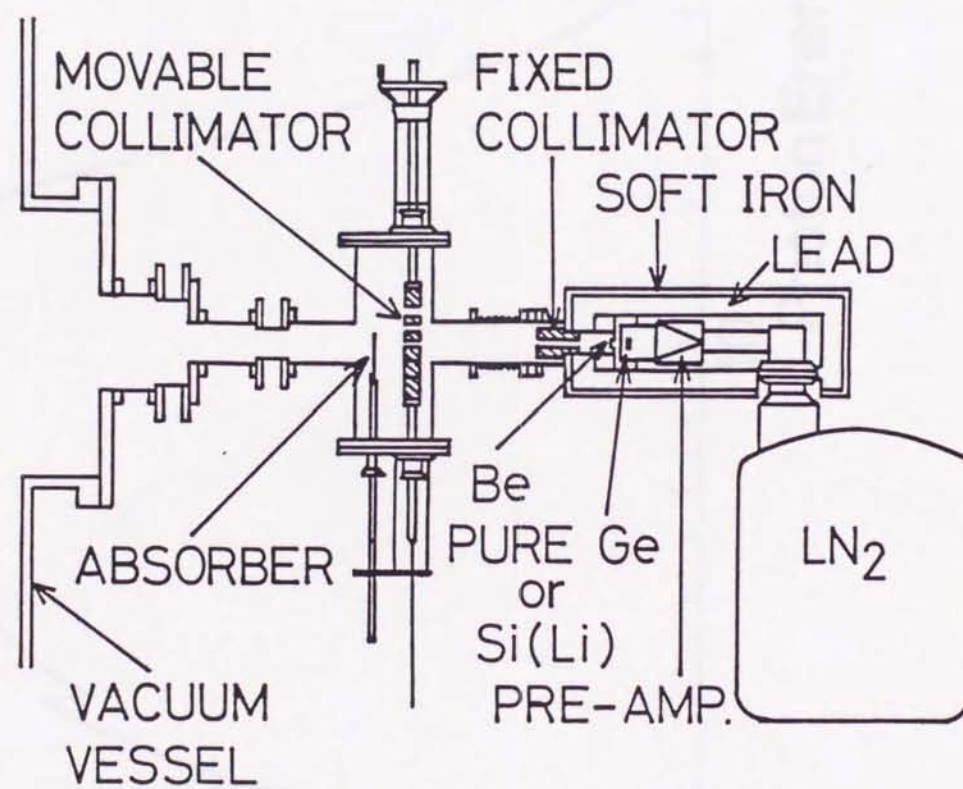
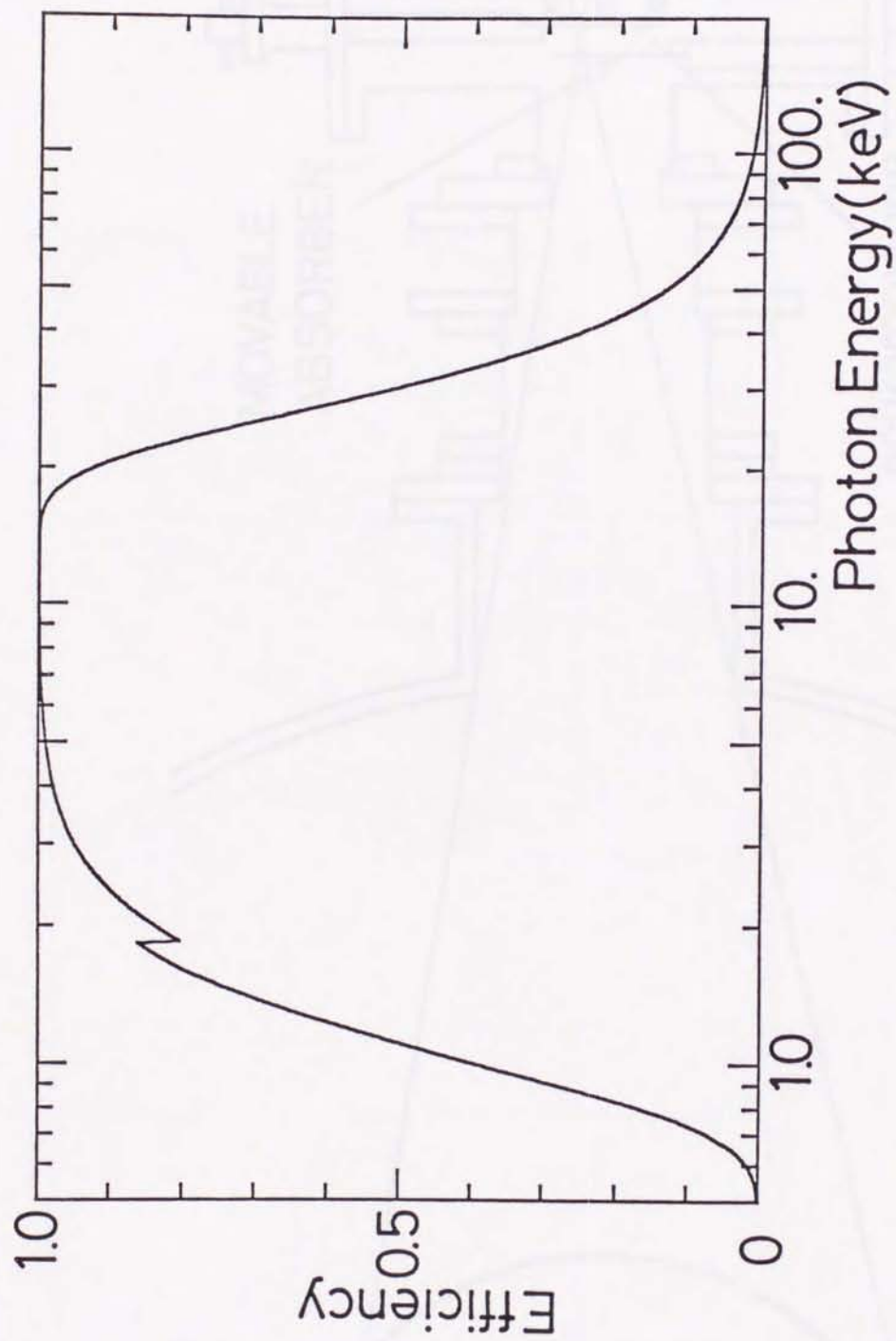


Fig. 3-6



Si(Li) Detector

Fig. 3-7

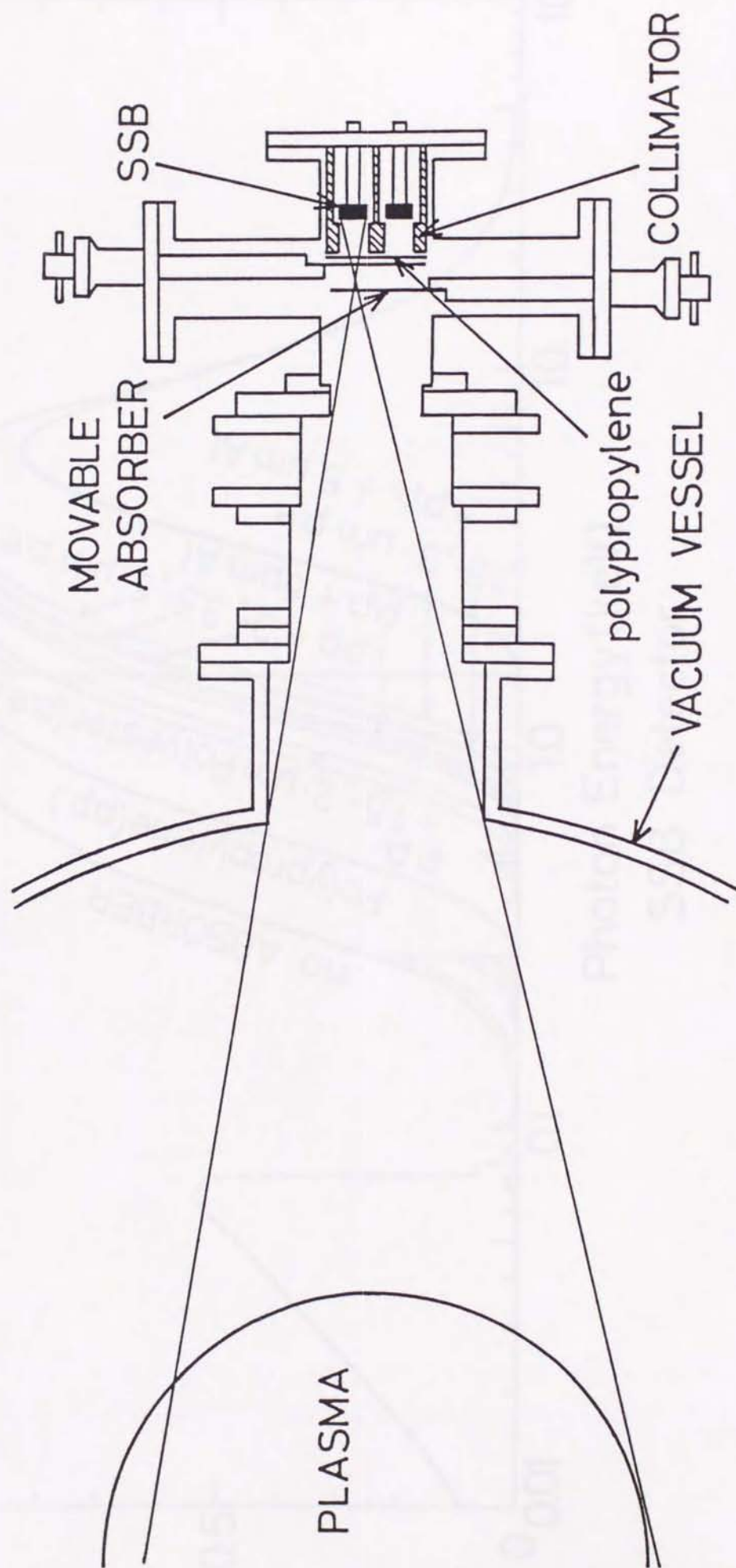


Fig. 3-8

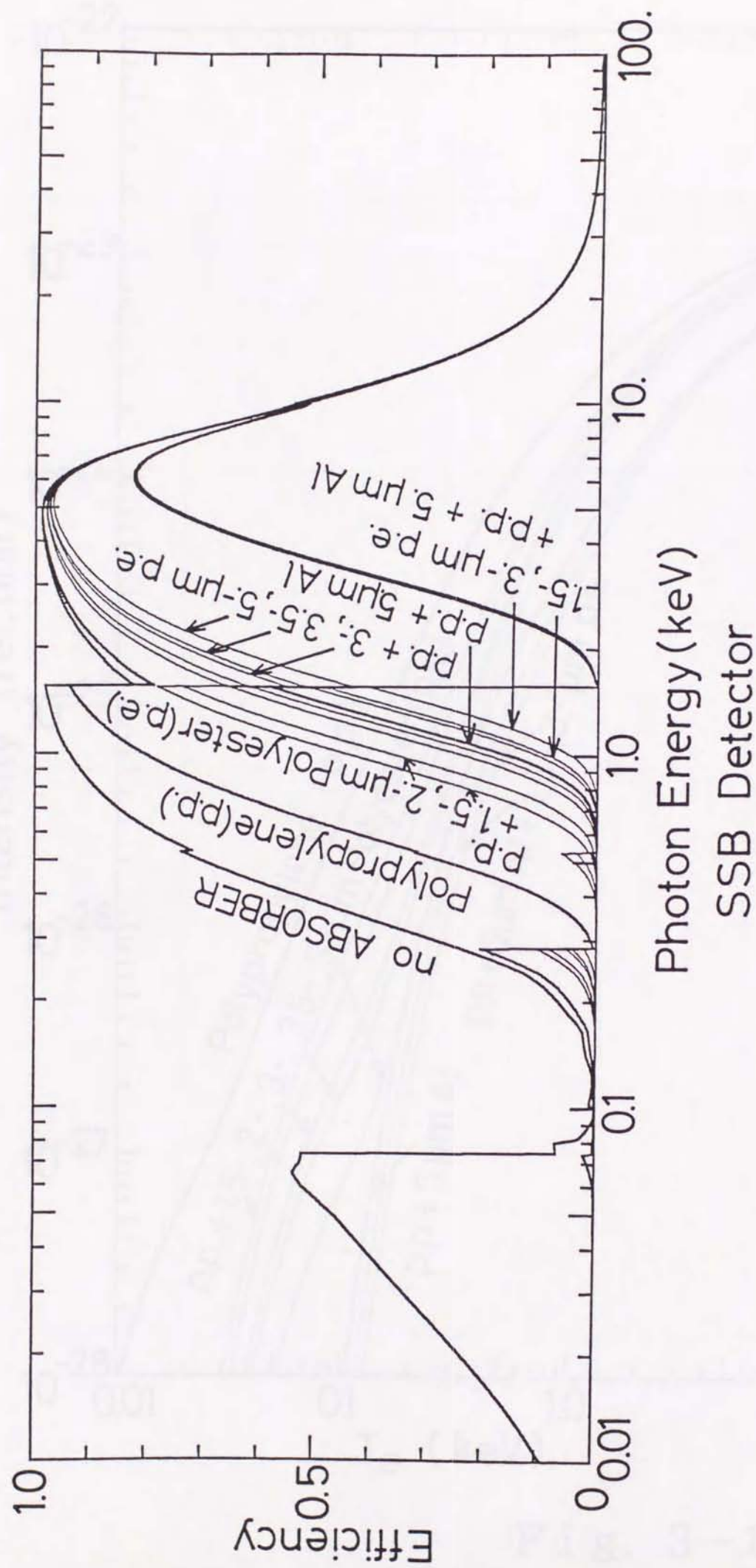


Fig. 3-9

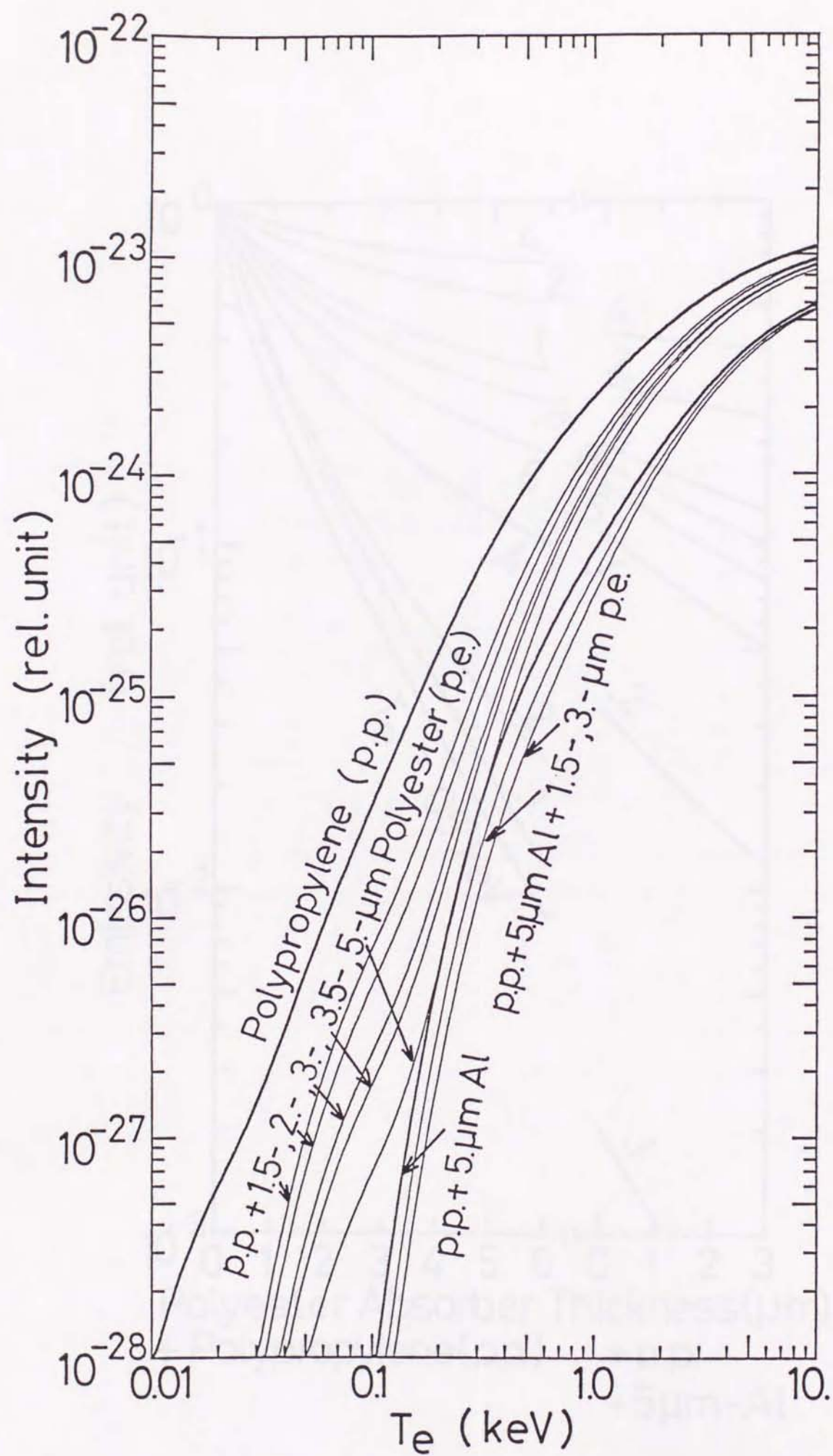
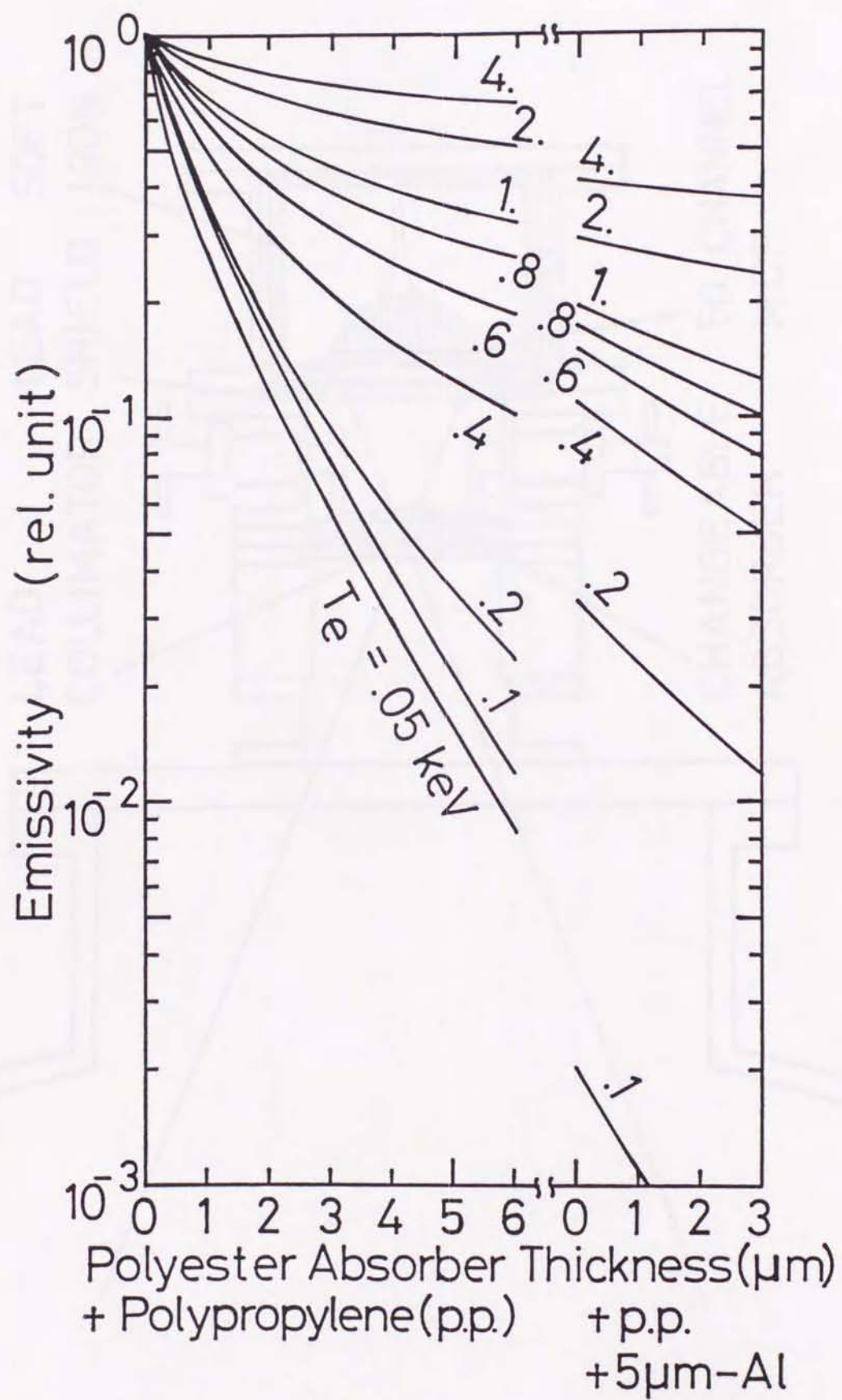


Fig. 3-10



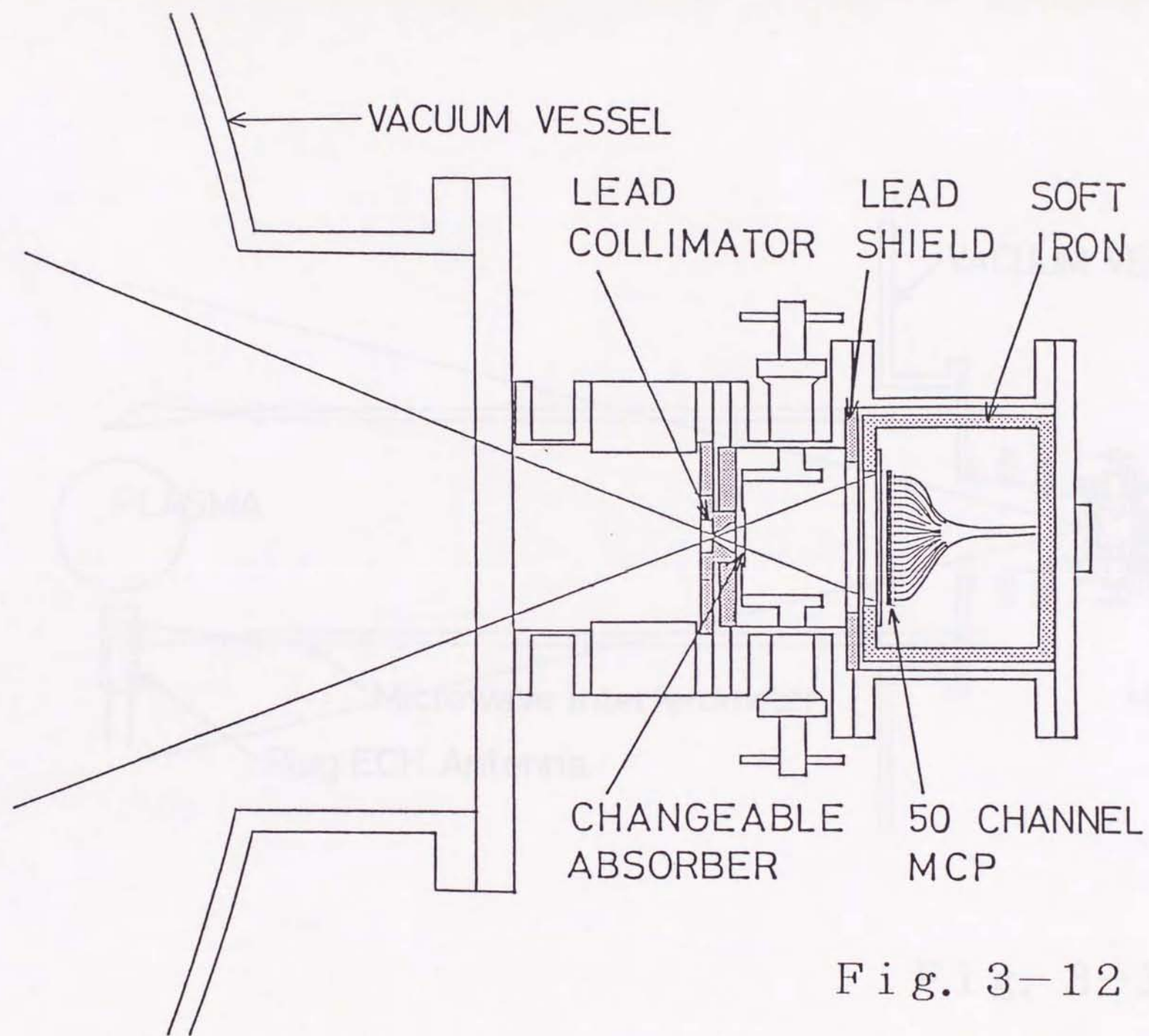


Fig. 3-12

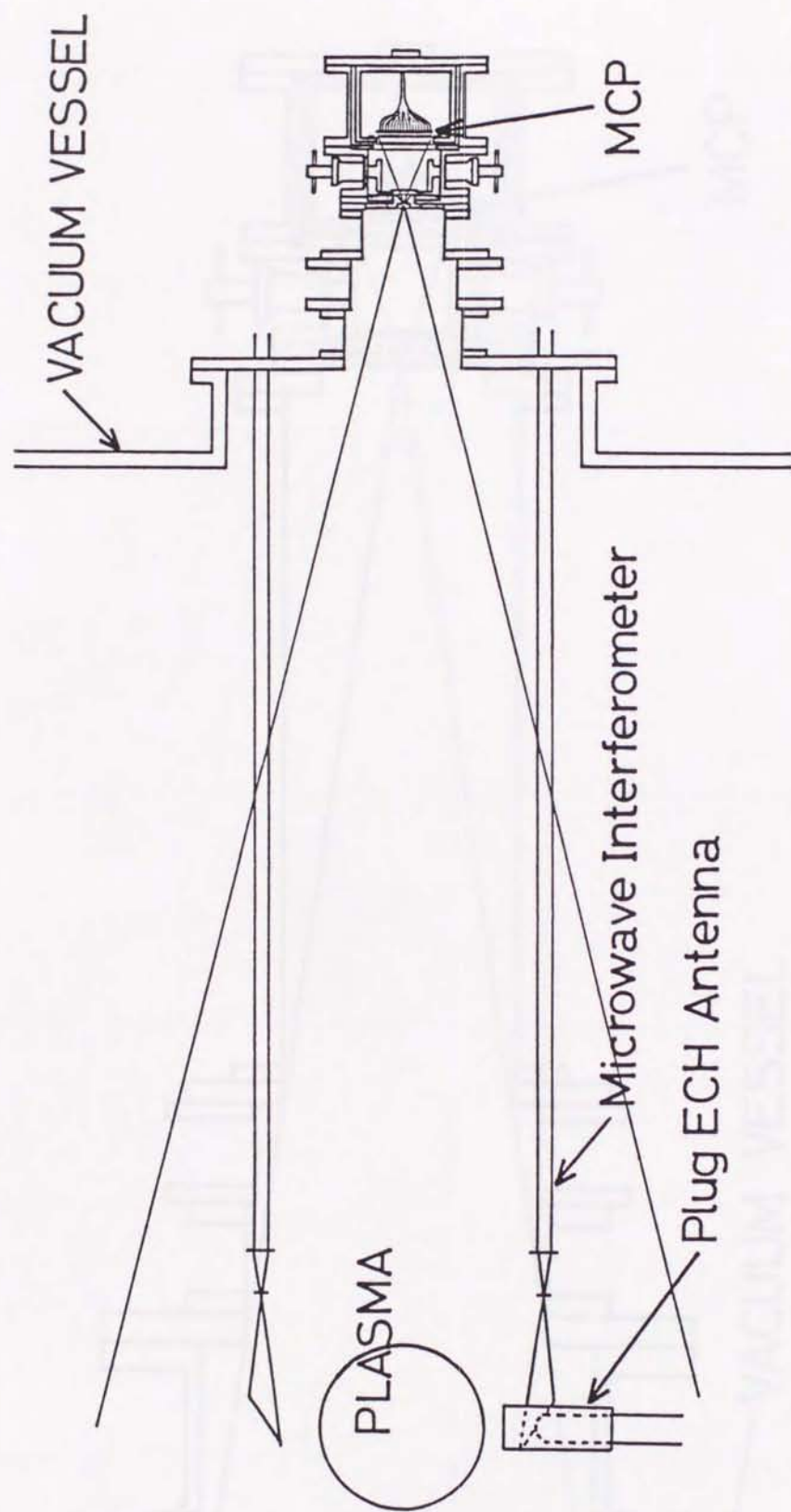


Fig. 3-13

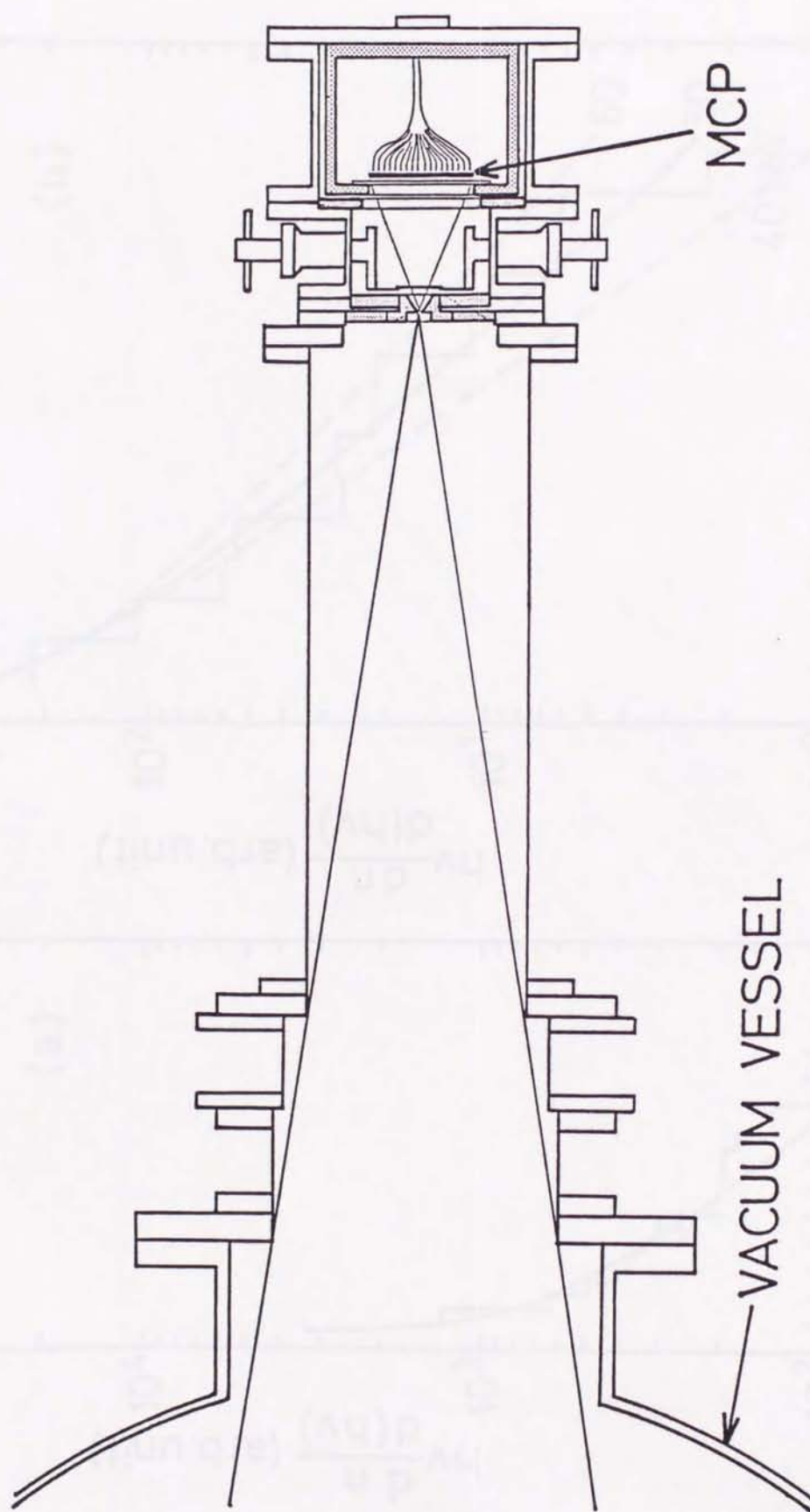


Fig. 3-14

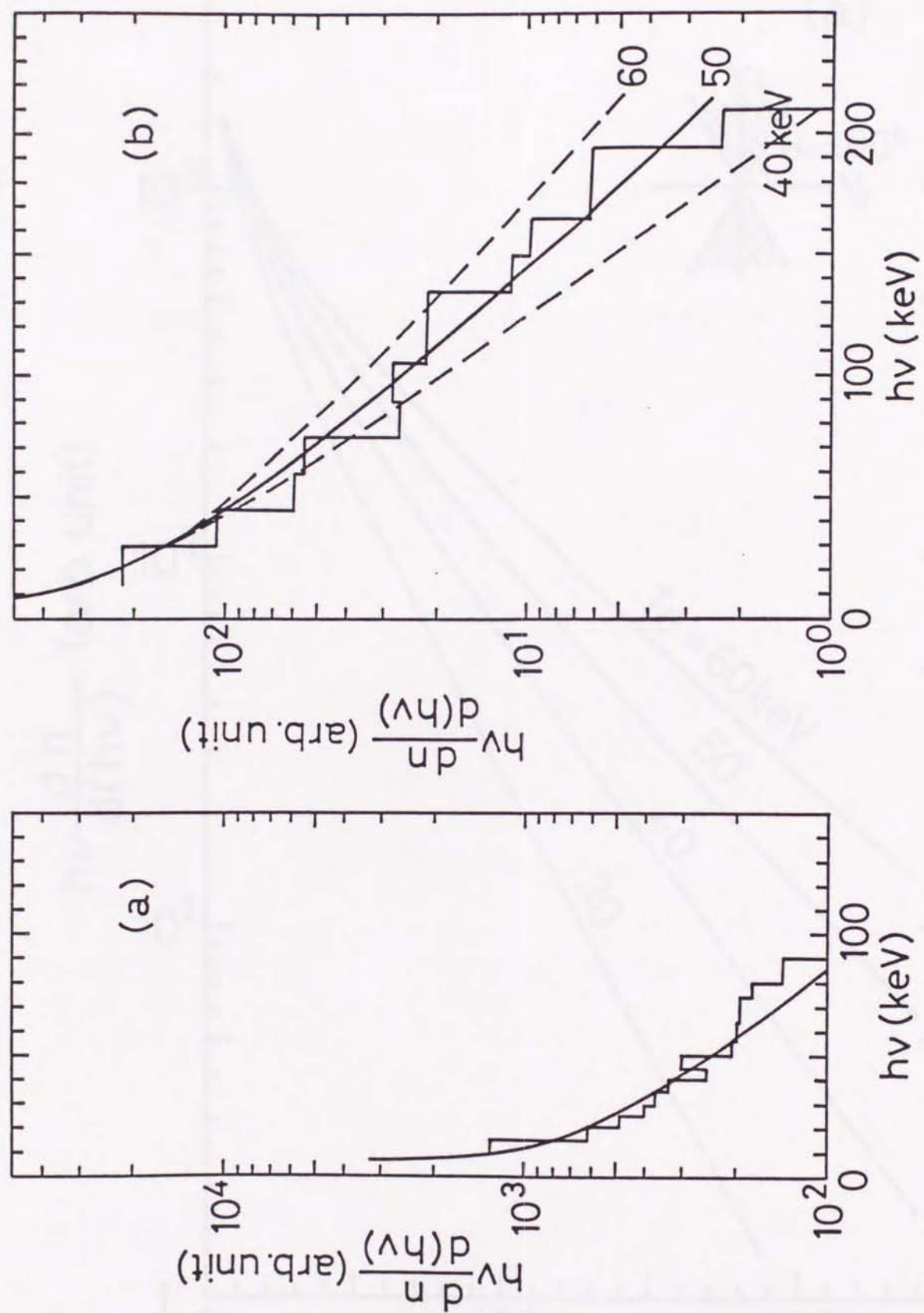


Fig. 4-1

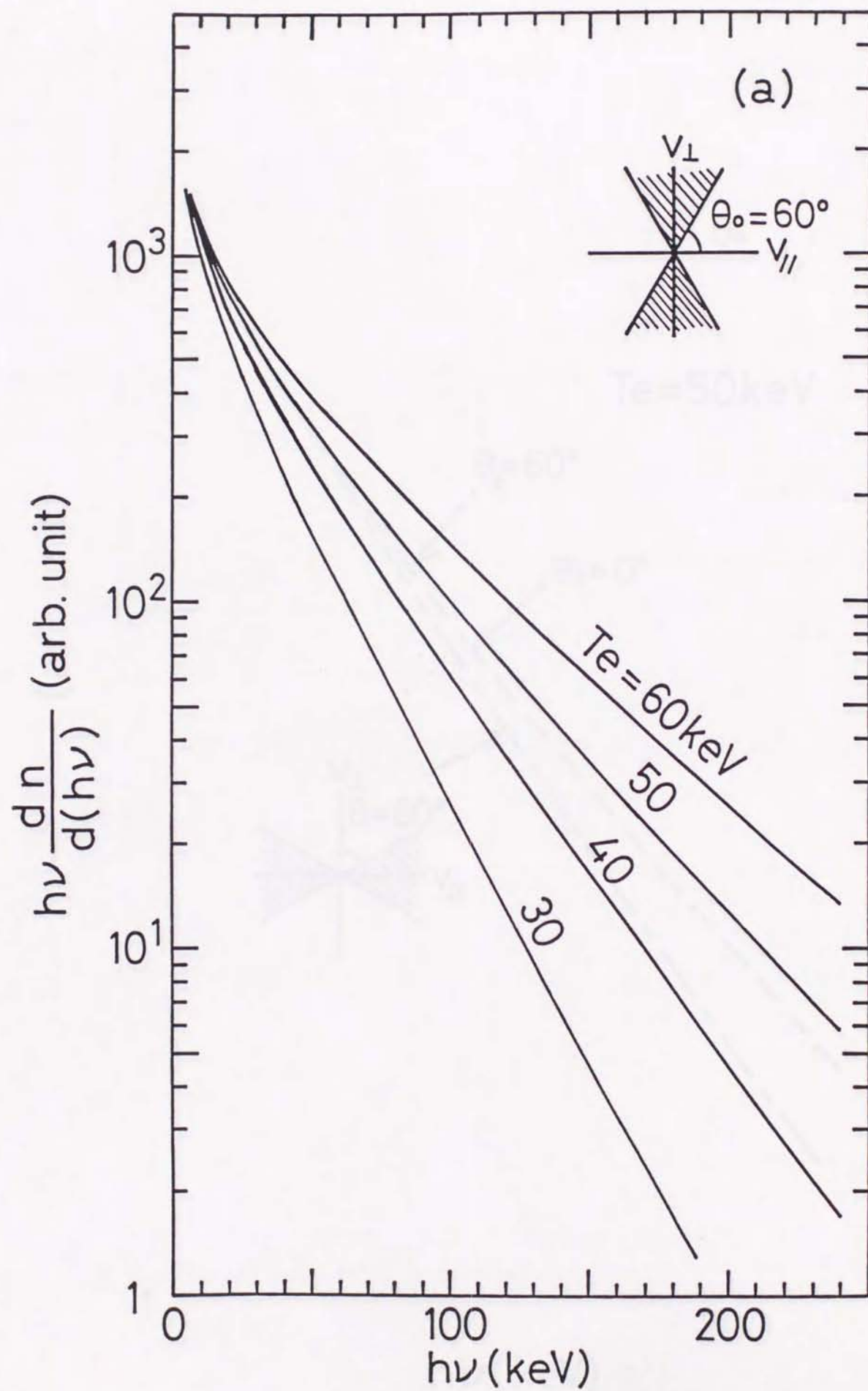


Fig. 4-2 (a)

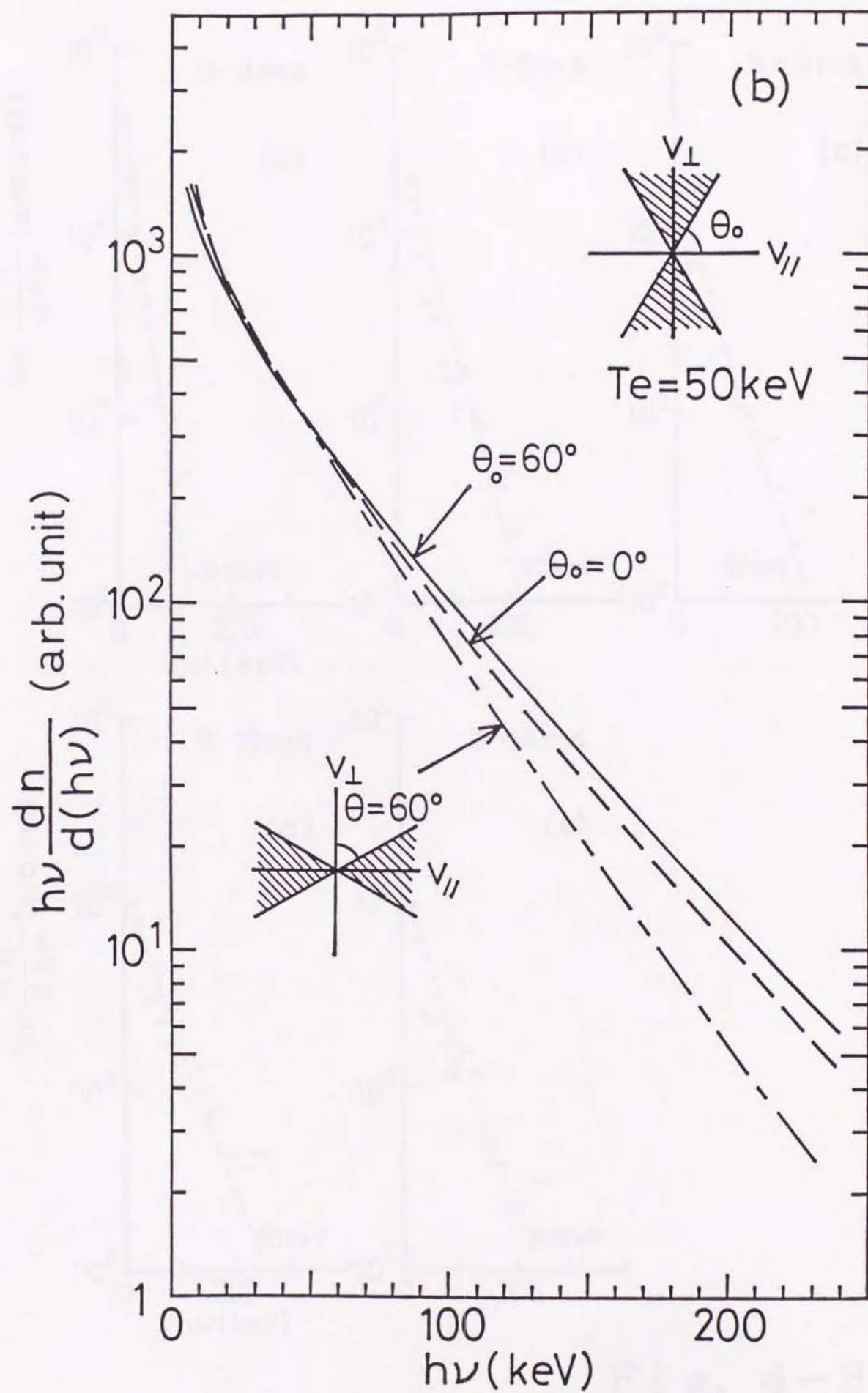


Fig. 4-2 (b)

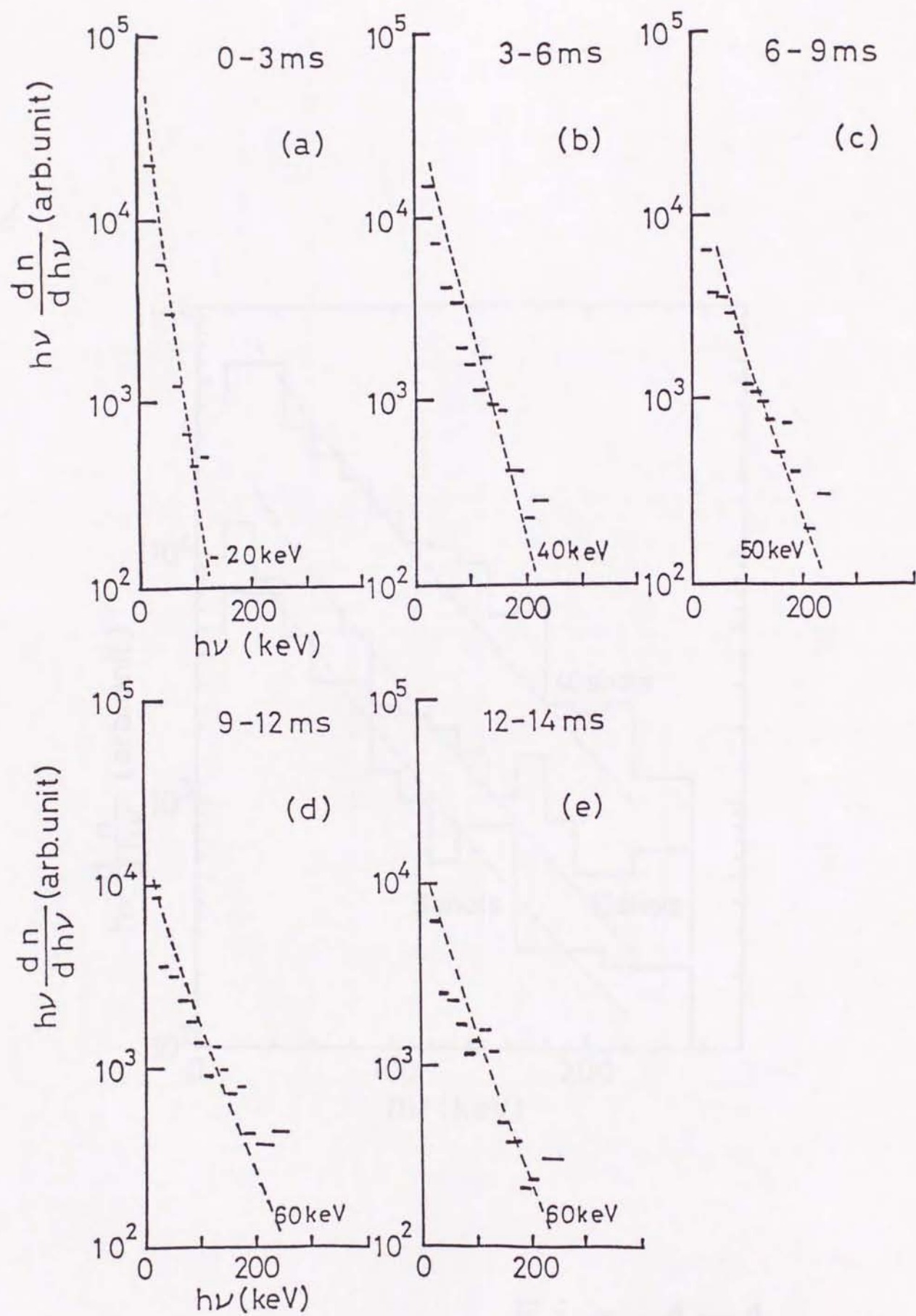


Fig. 4-3

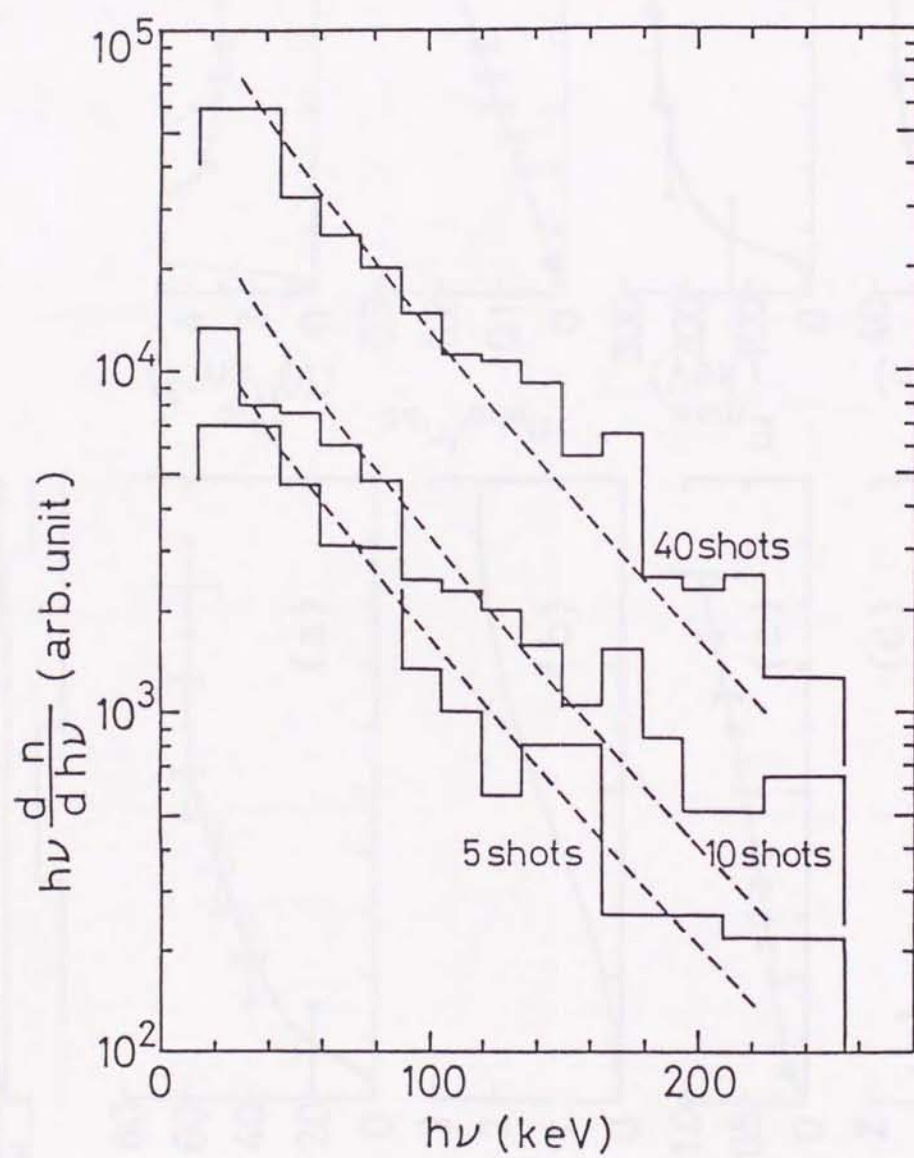


Fig. 4-4

Plasma Gun
Anchor NBI
Sloshing NBI
Barrier ECH
Plug ECH

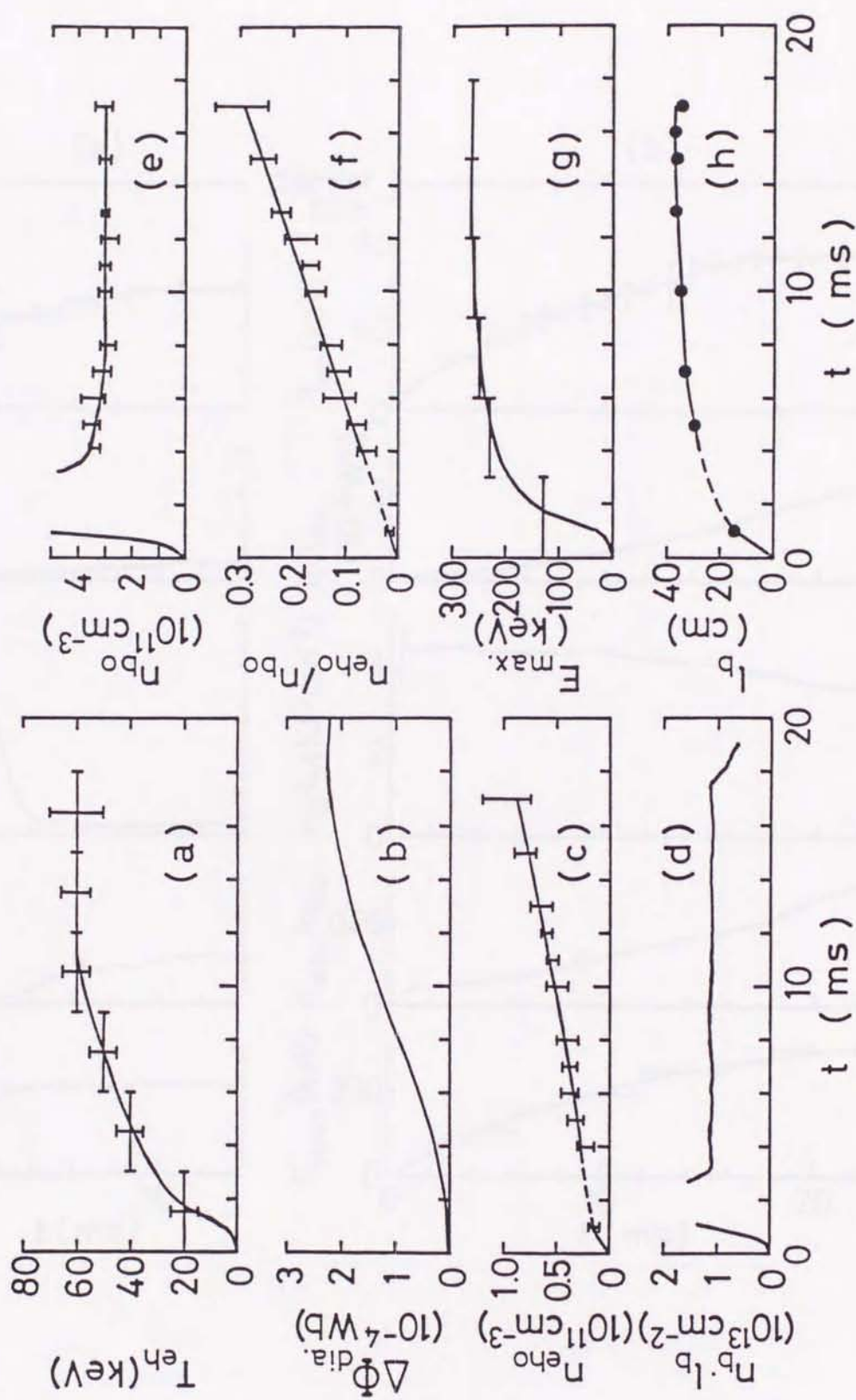


Fig. 4-5

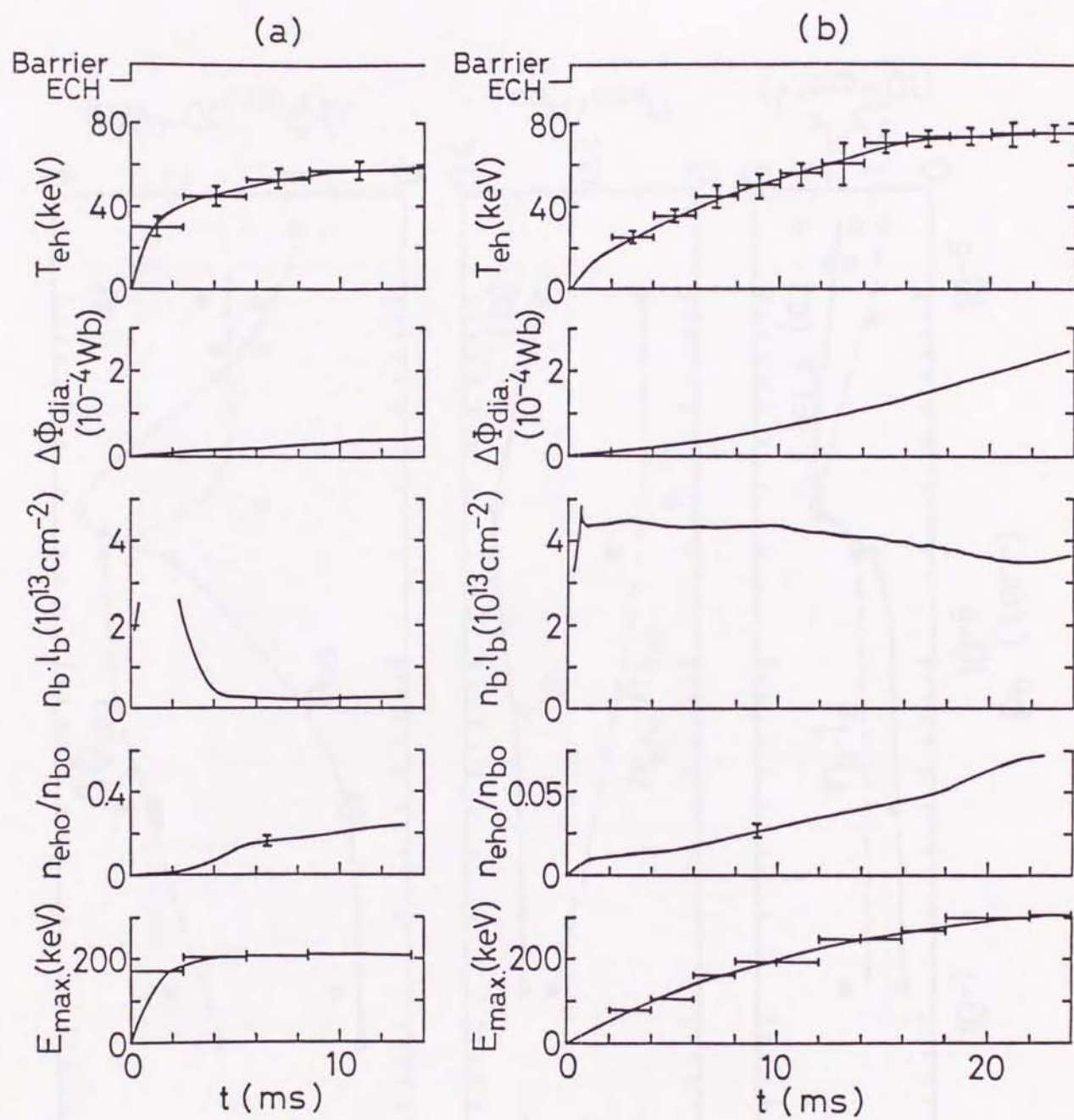


Fig. 4-6

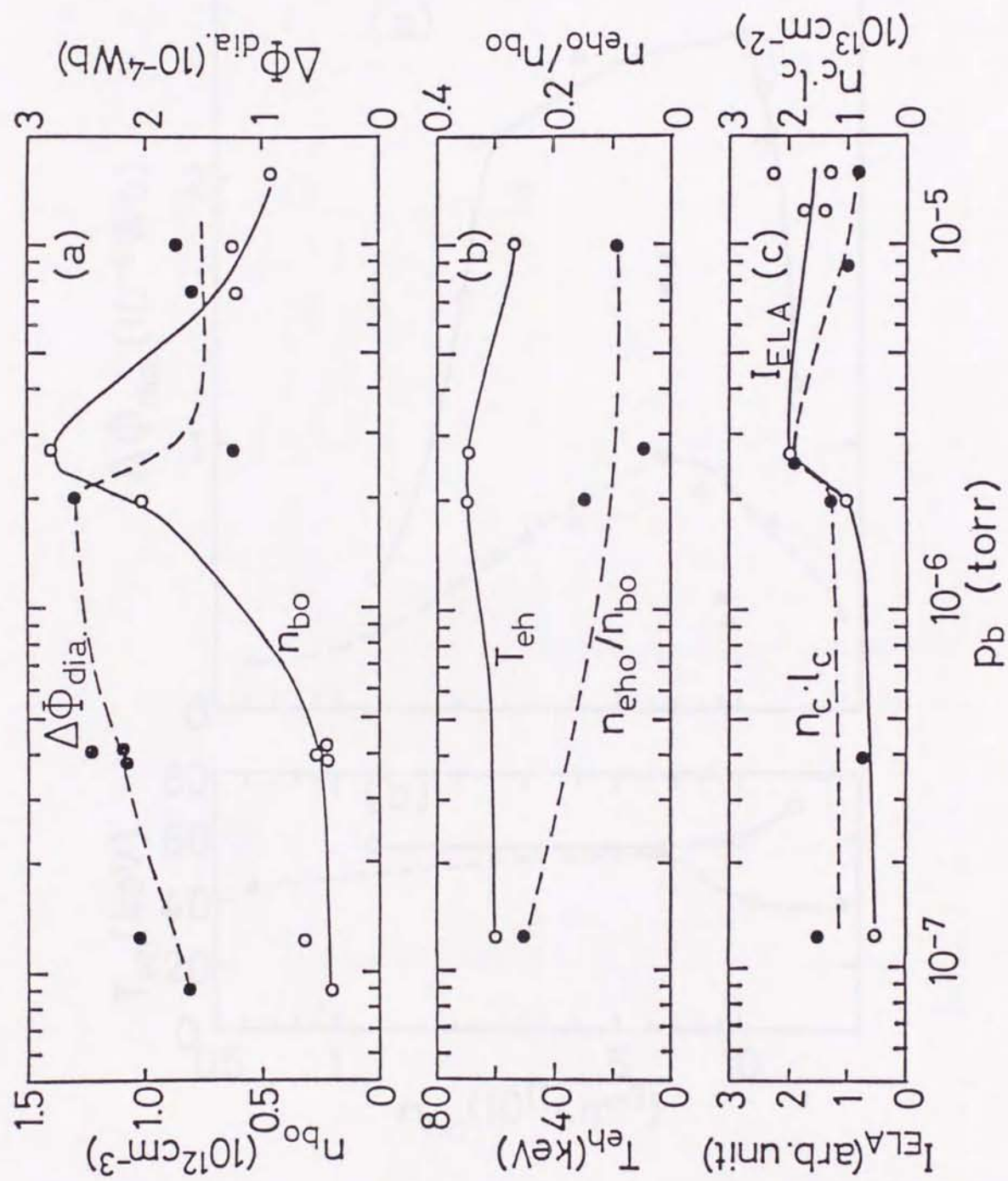


Fig. 4-7

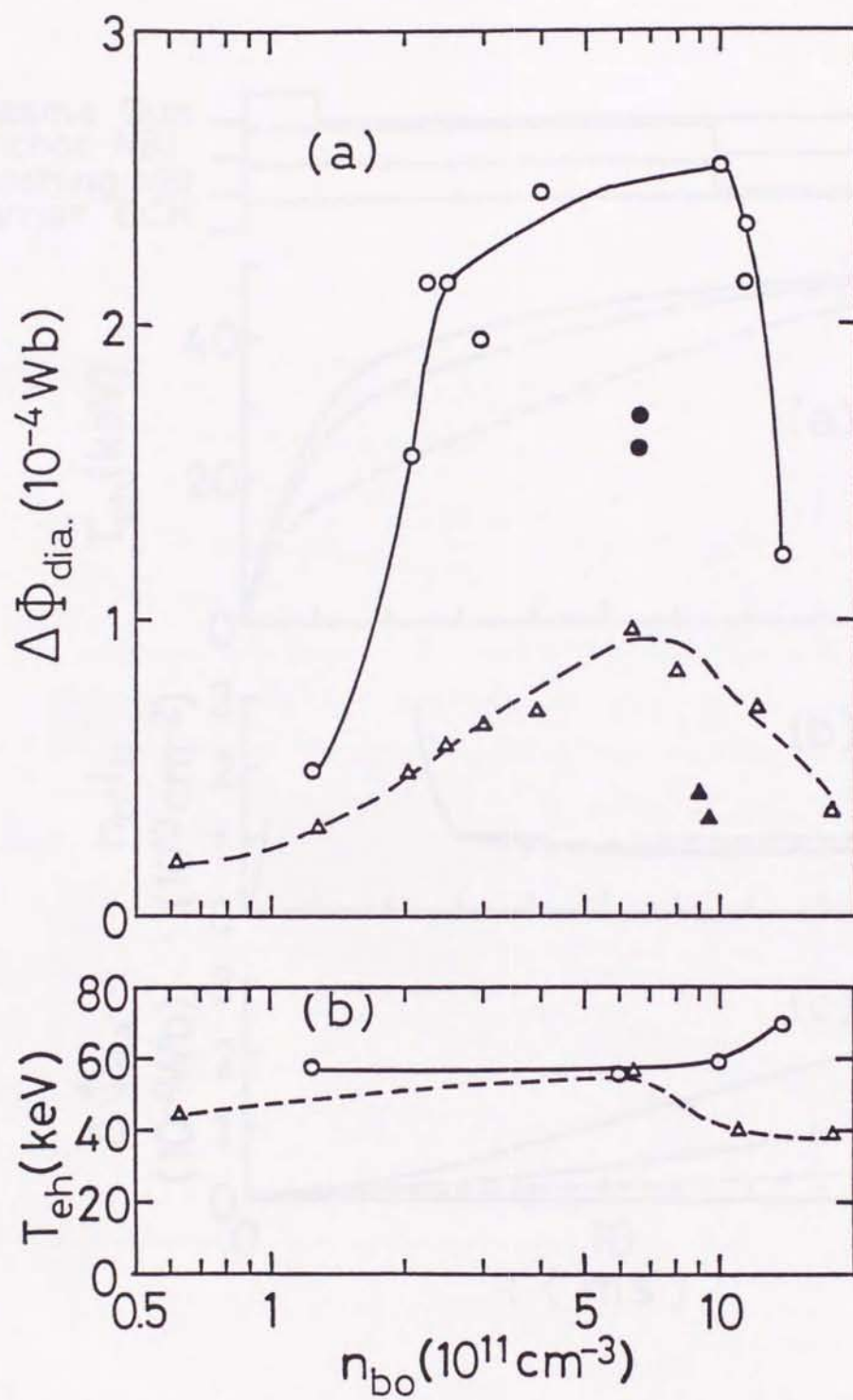


Fig. 4-8

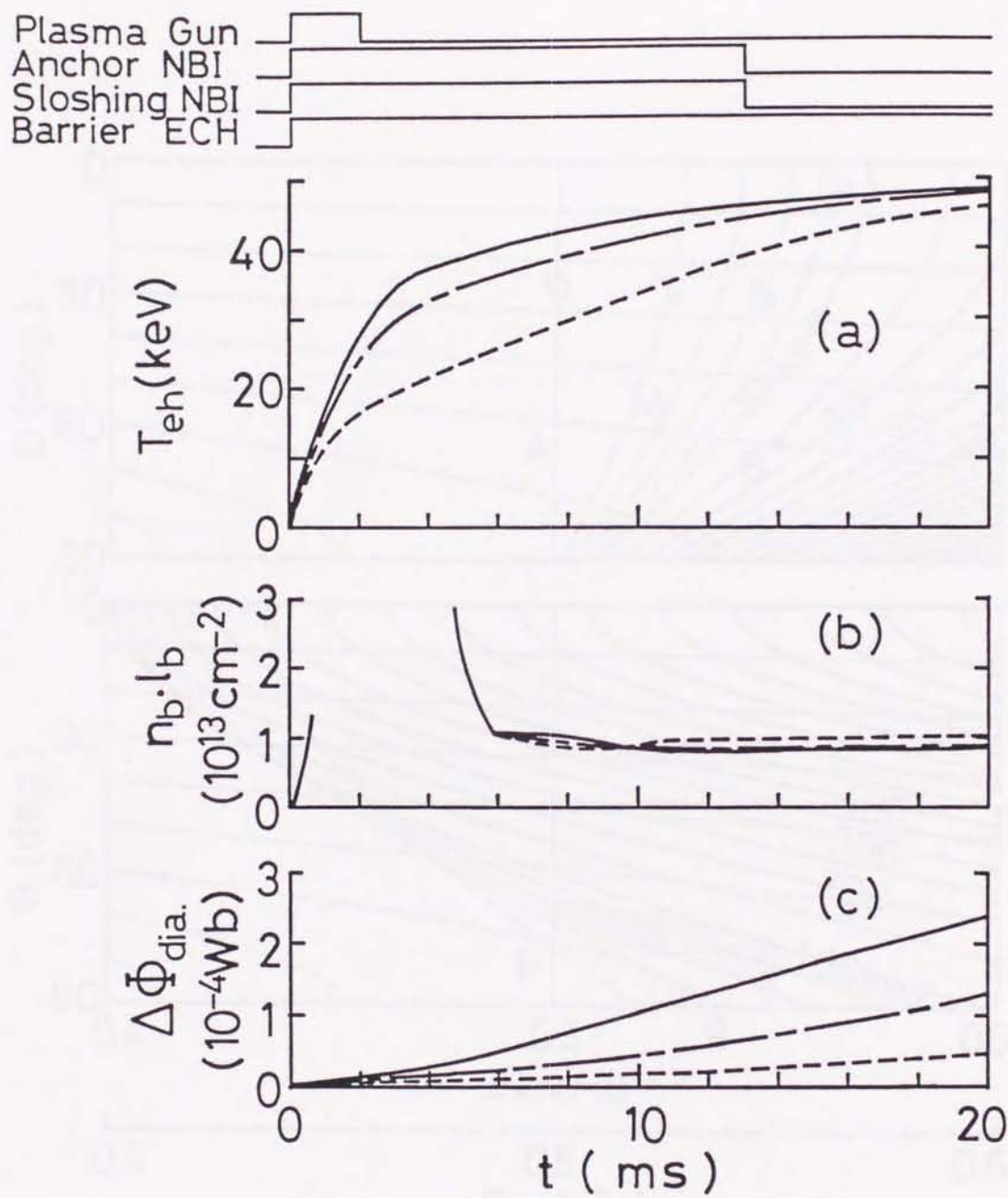


Fig. 4-9

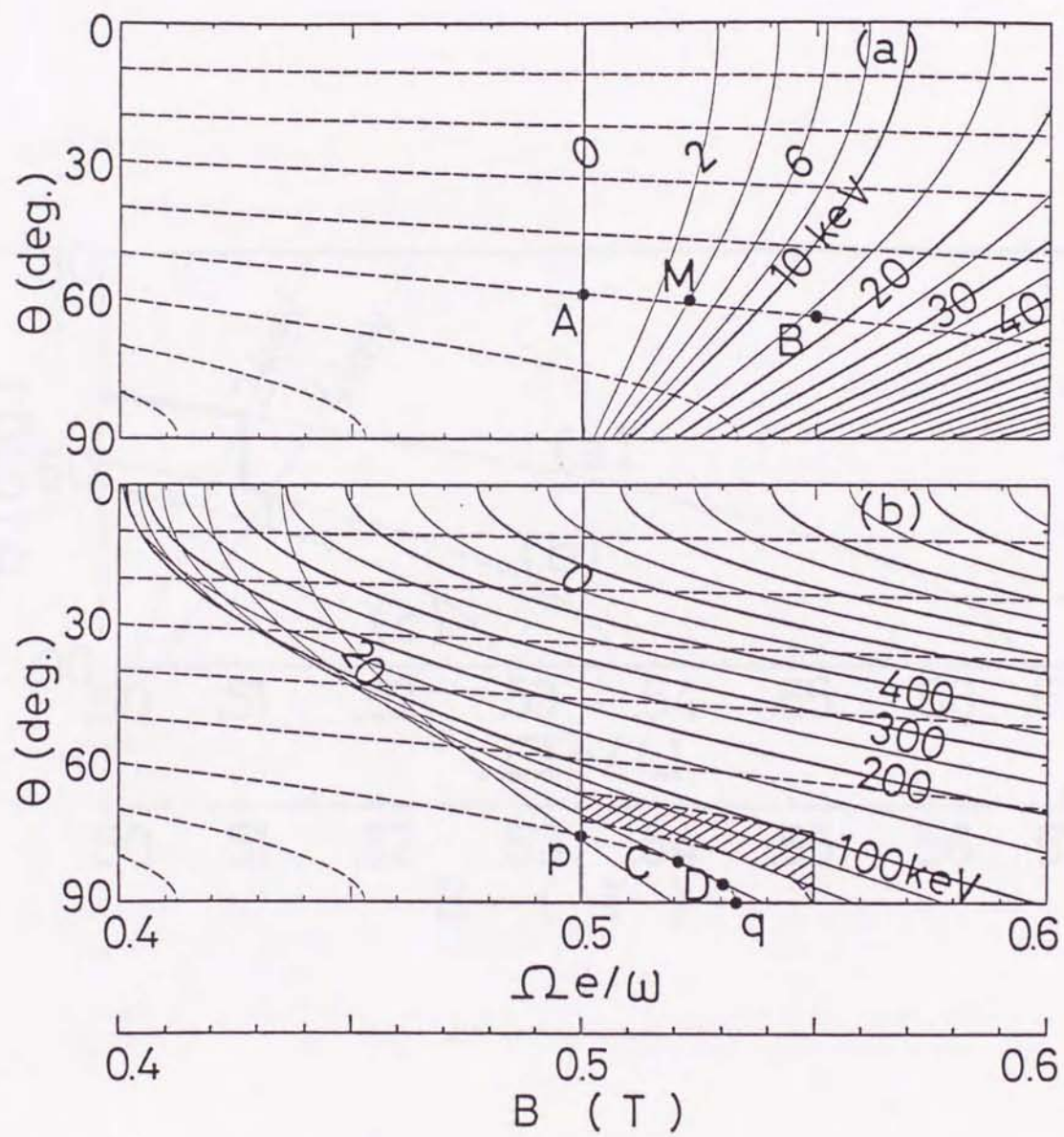


Fig. 4-10

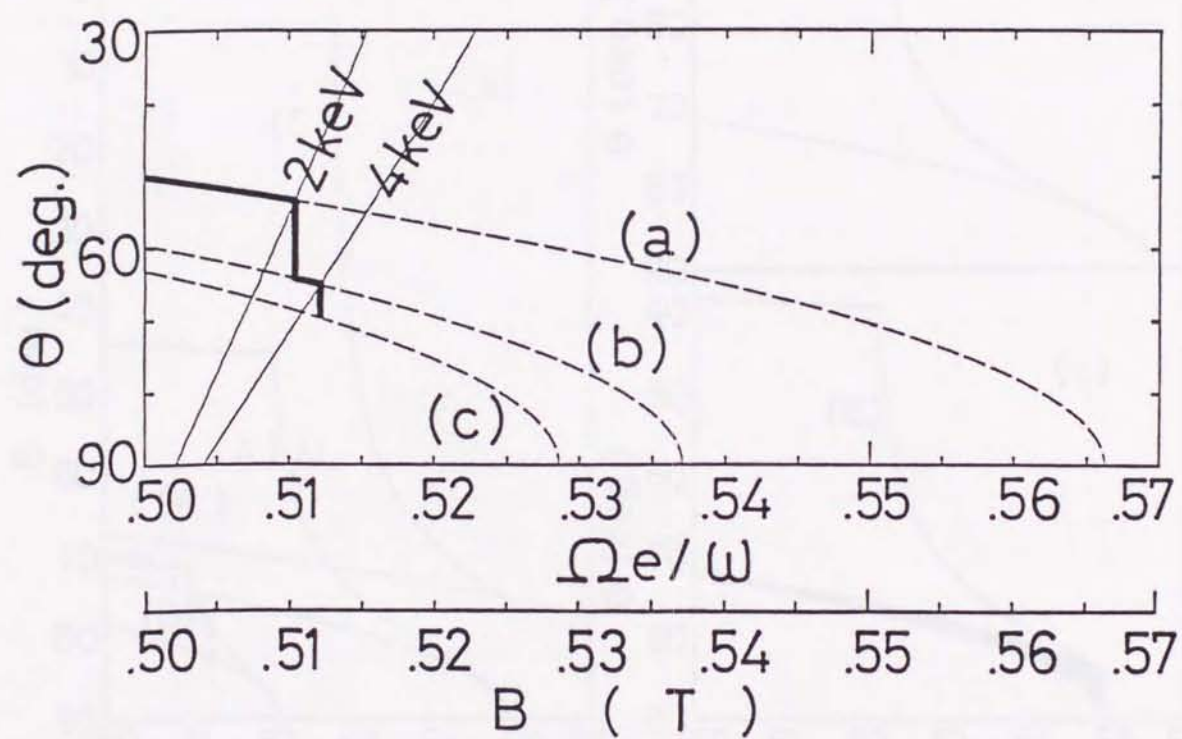


Fig. 4-11

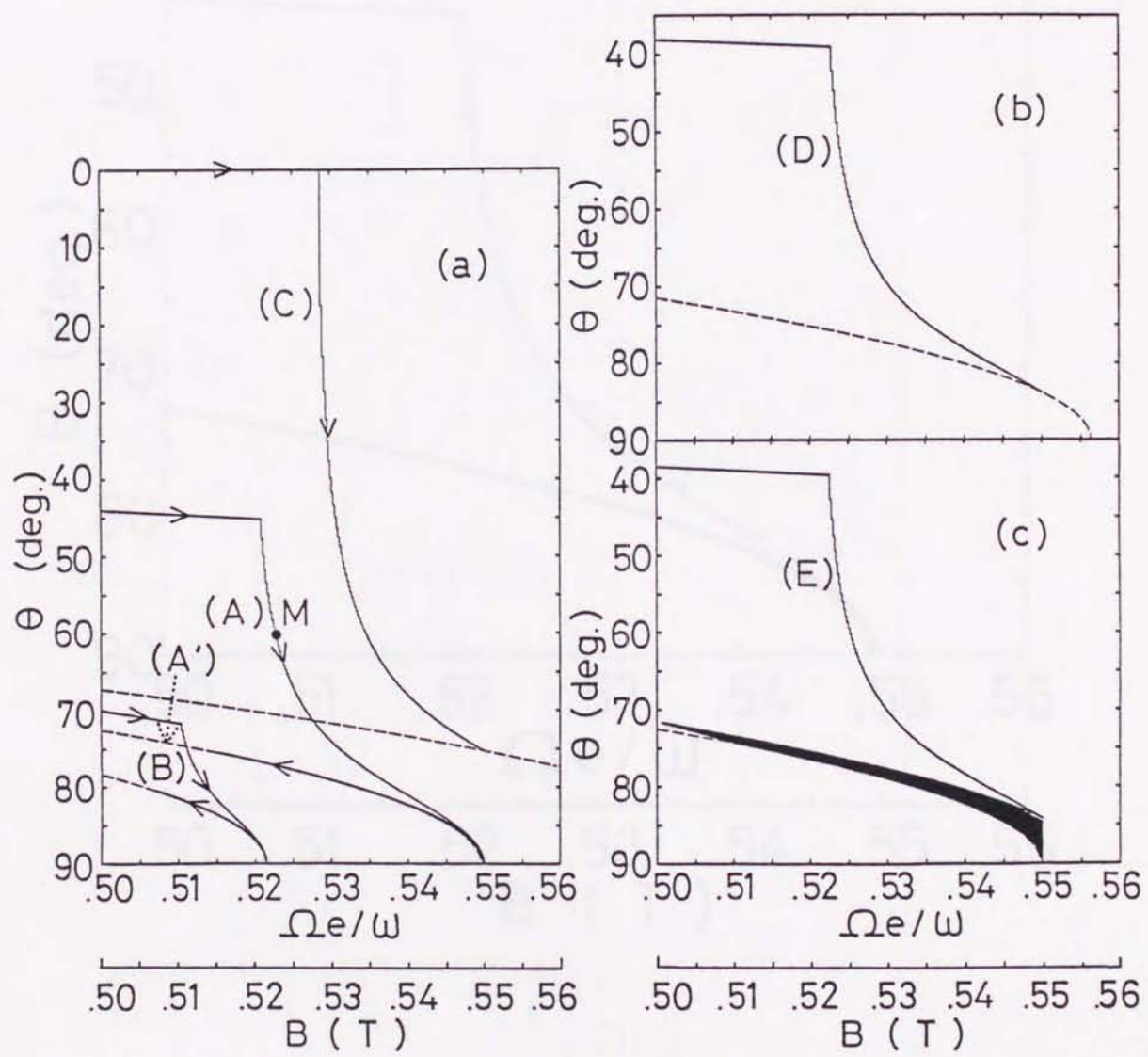


Fig. 4-12

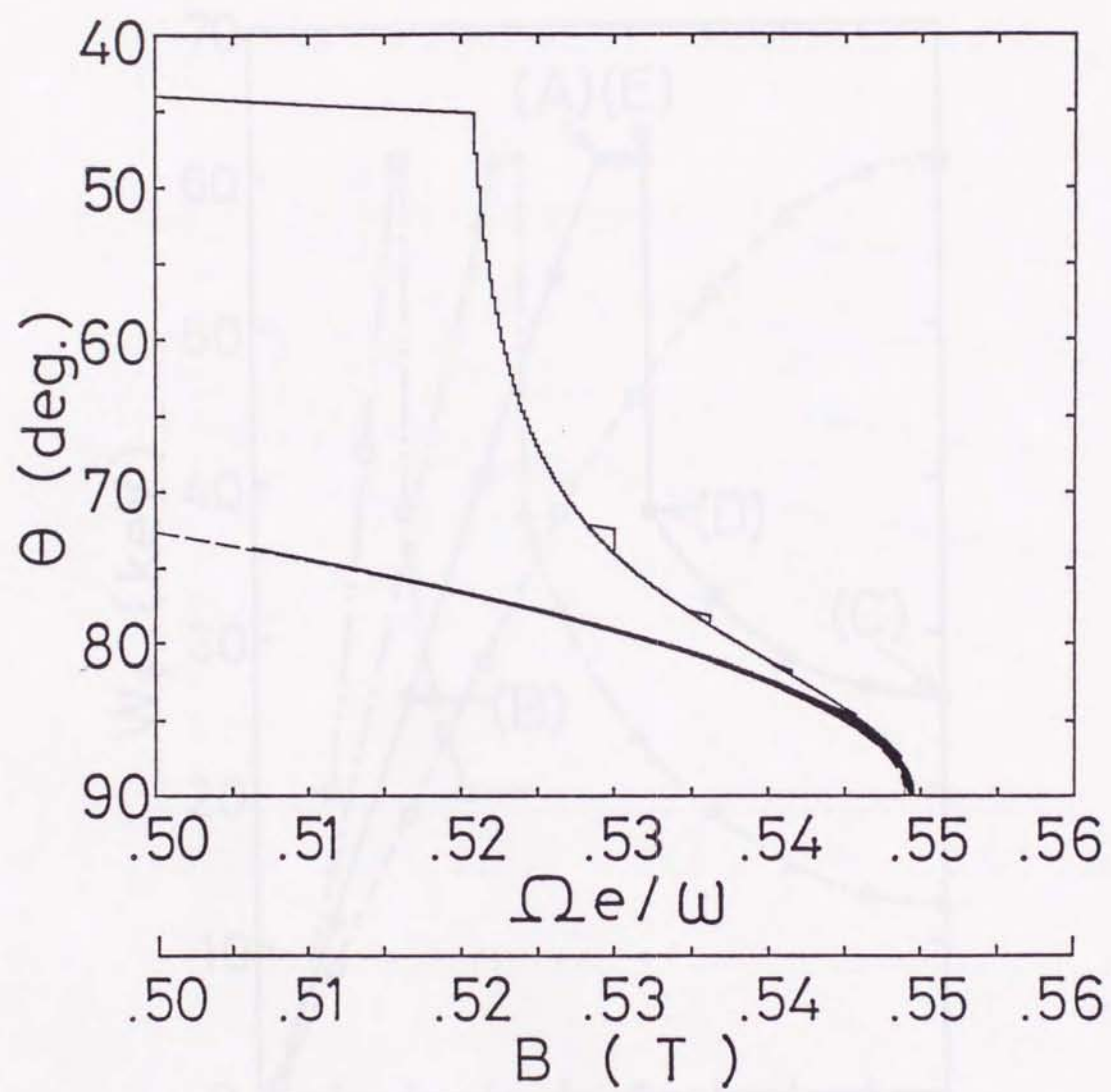


Fig. 4-13

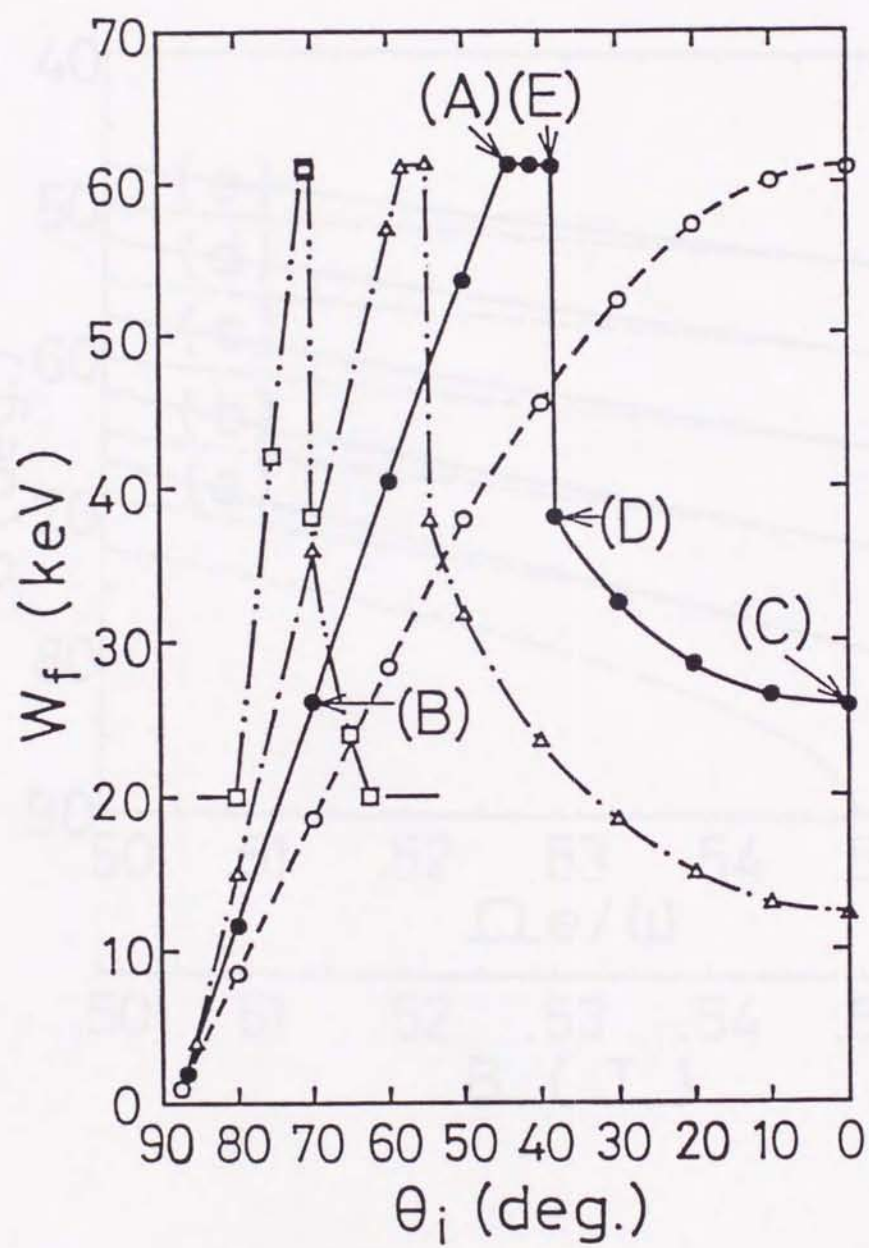


Fig. 4-14

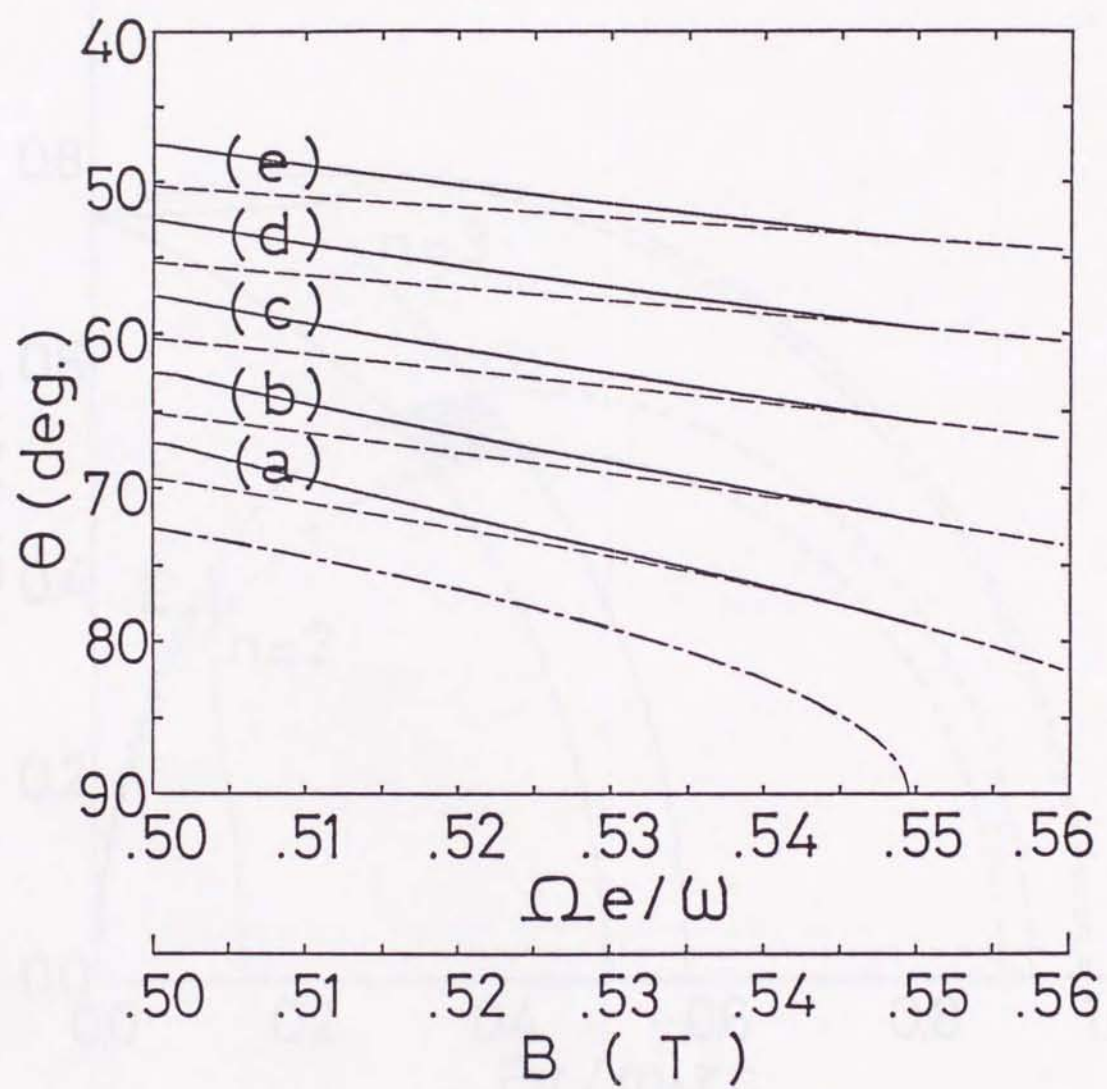


Fig. 4-15

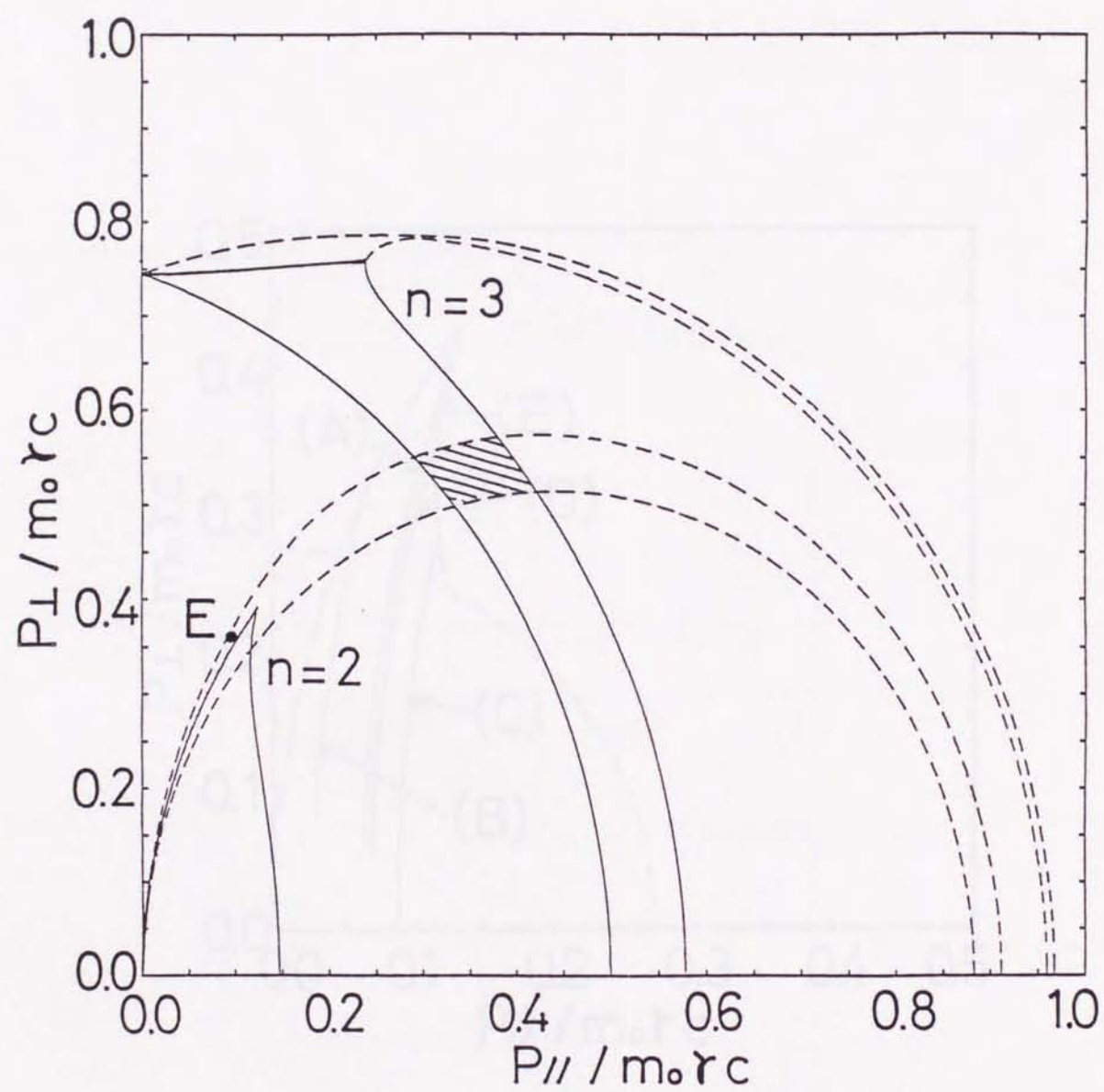


Fig. 4-16

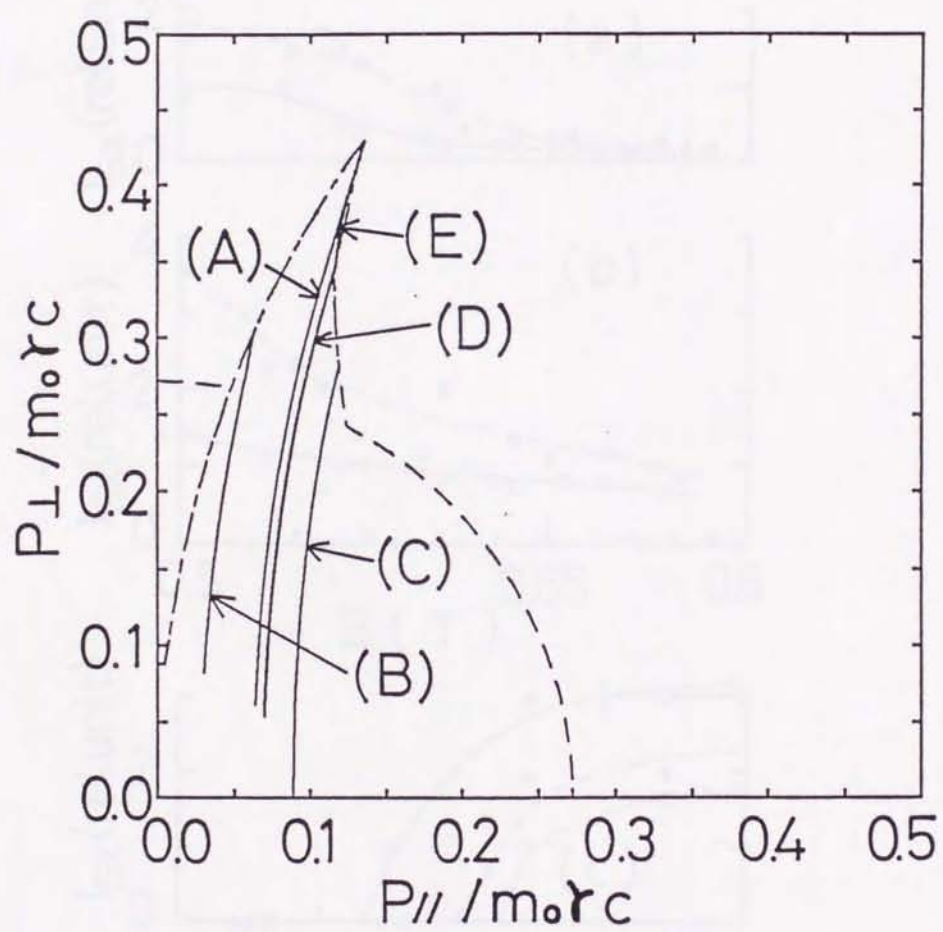


Fig. 4-17

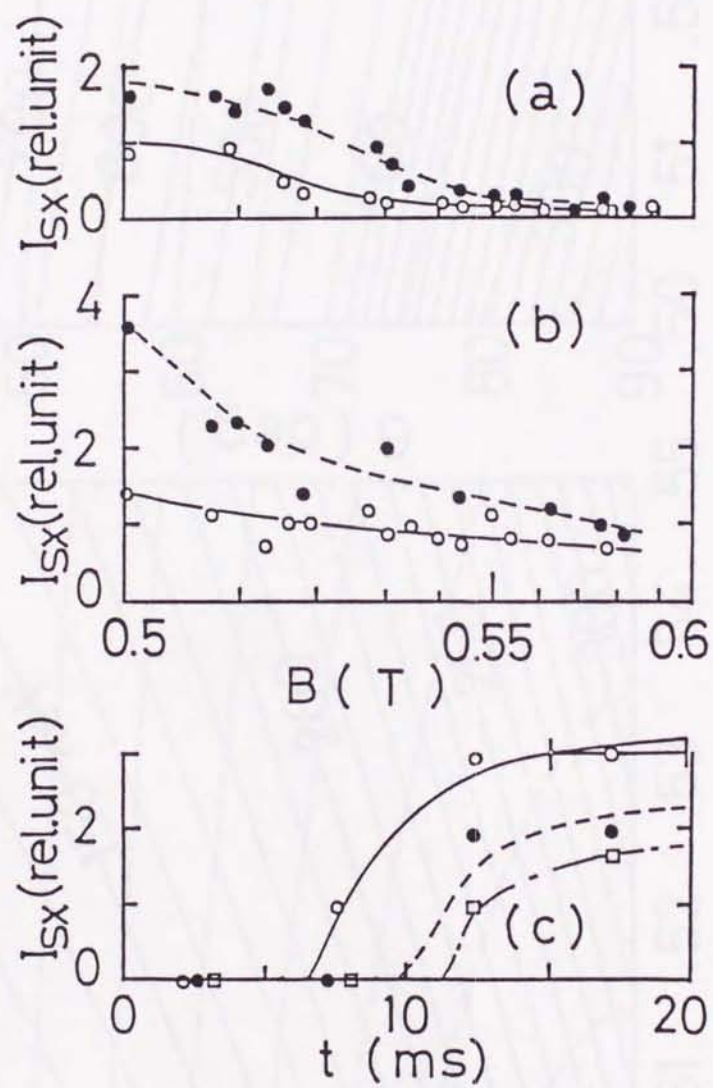


Fig. 4-18

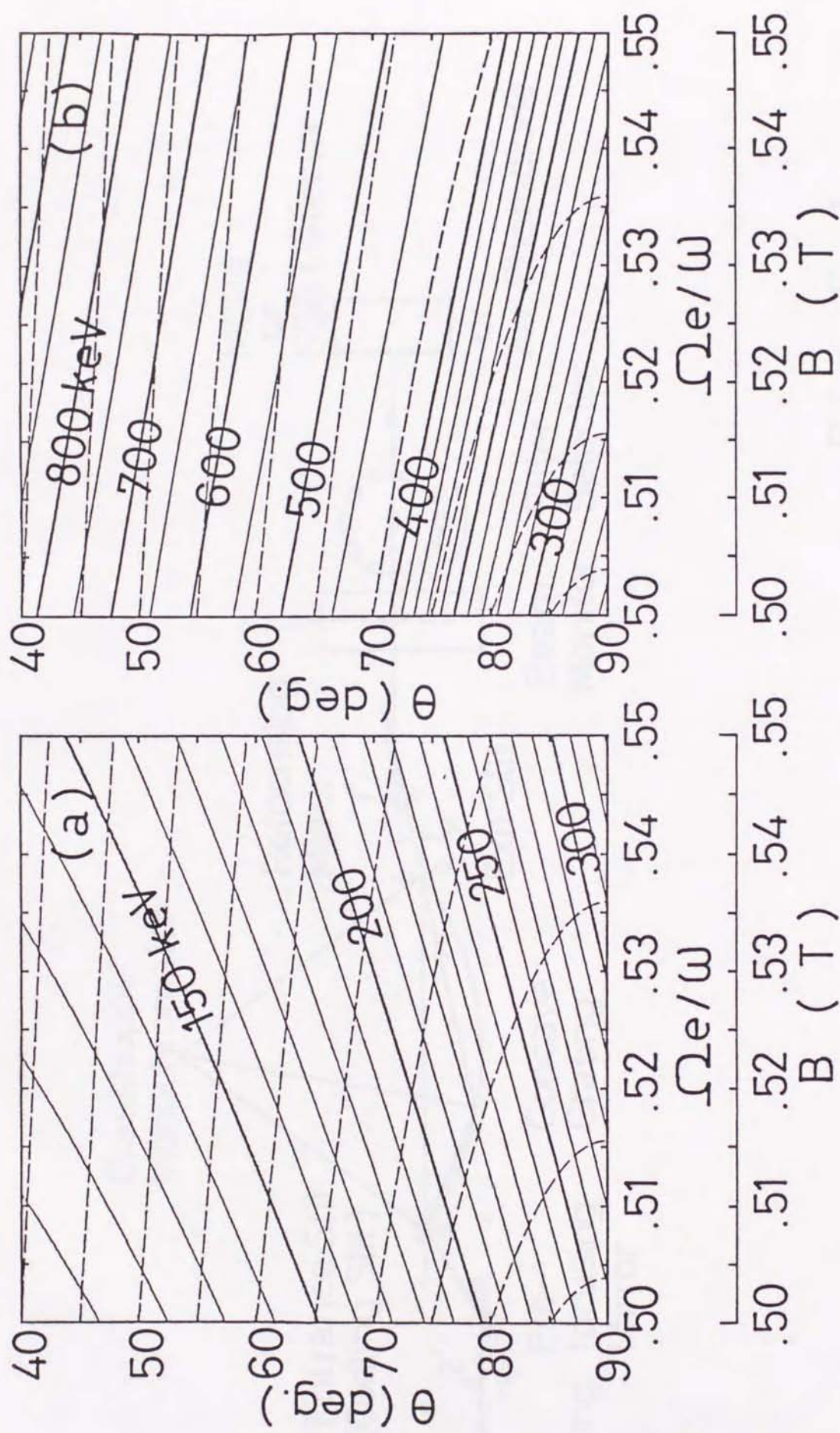


Fig. 4-19

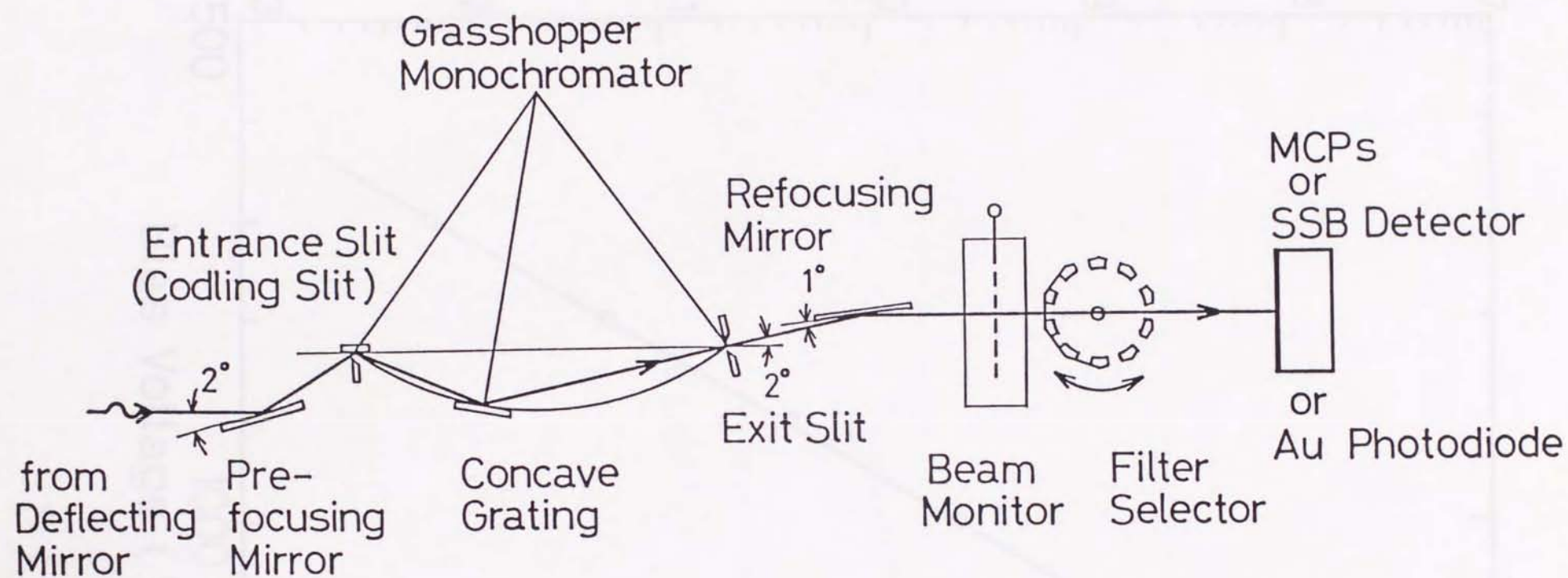


Fig. 5-1

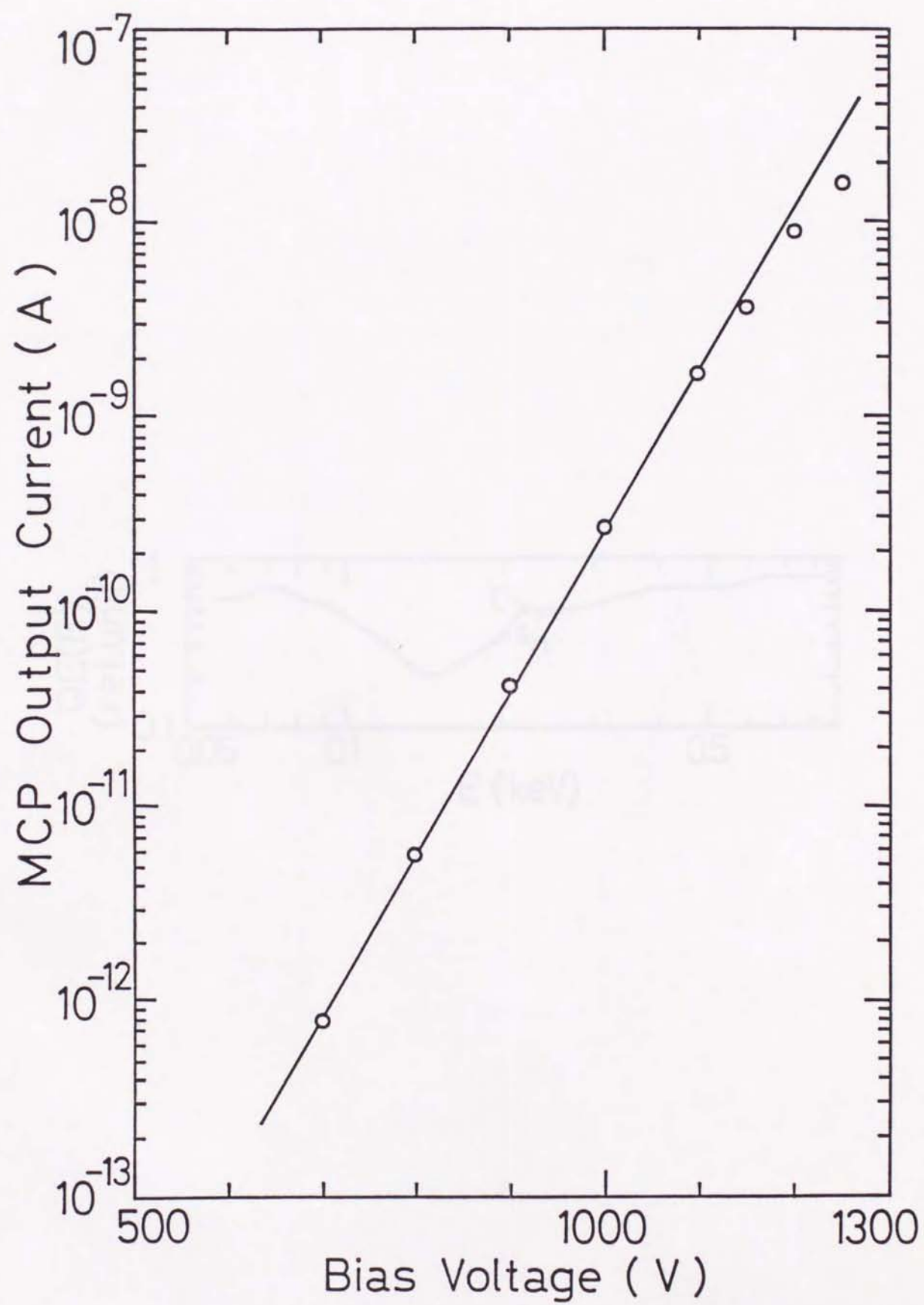


Fig. 5-2

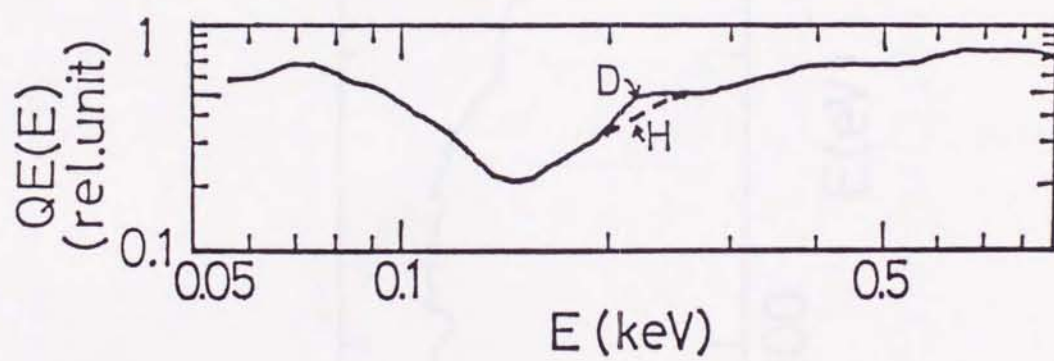


Fig. 5-3

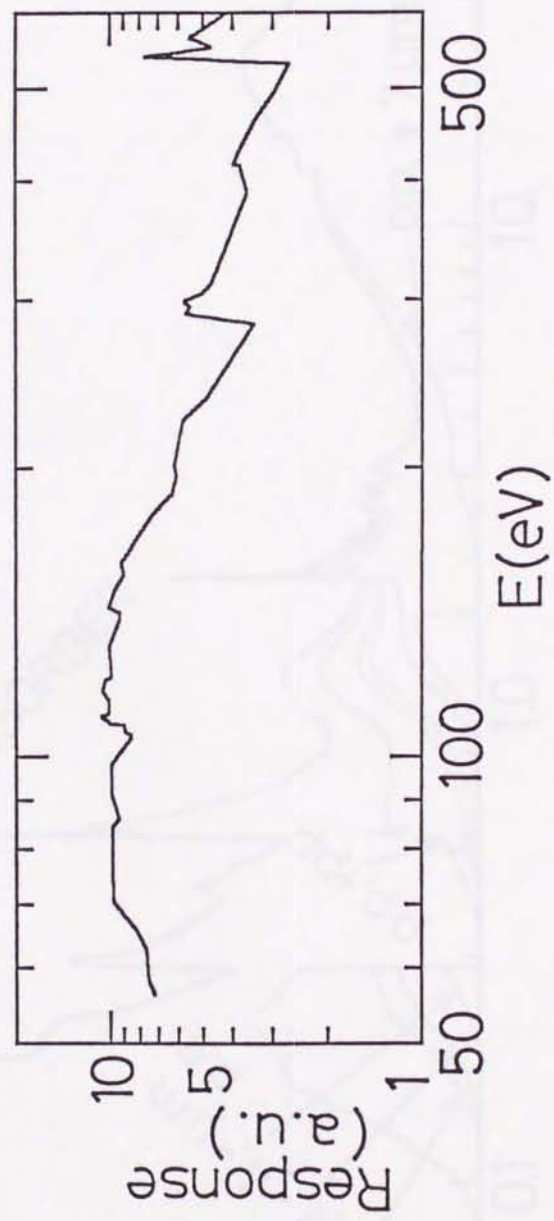
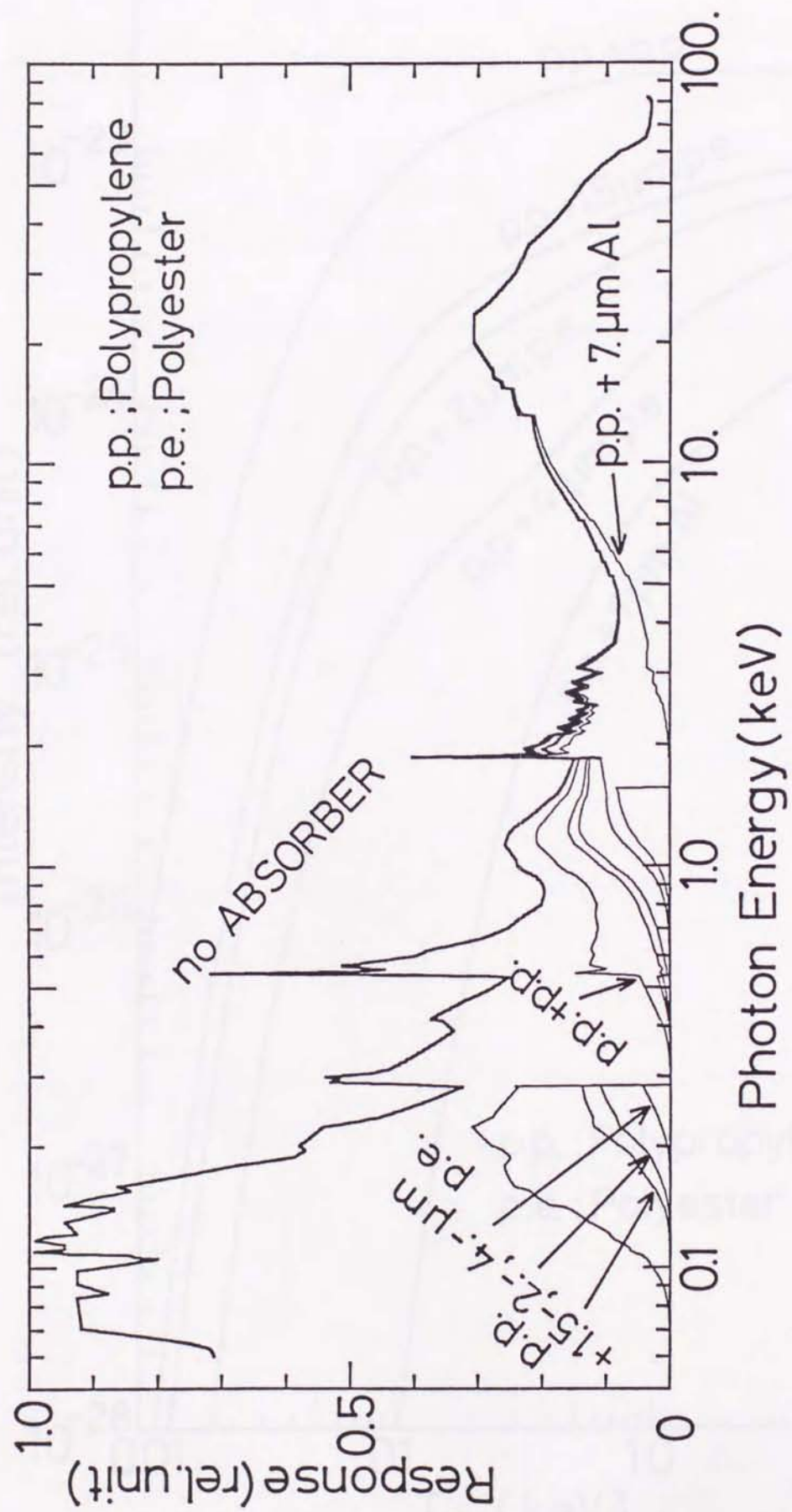


Fig. 5-4



MCPs

Fig. 5-5

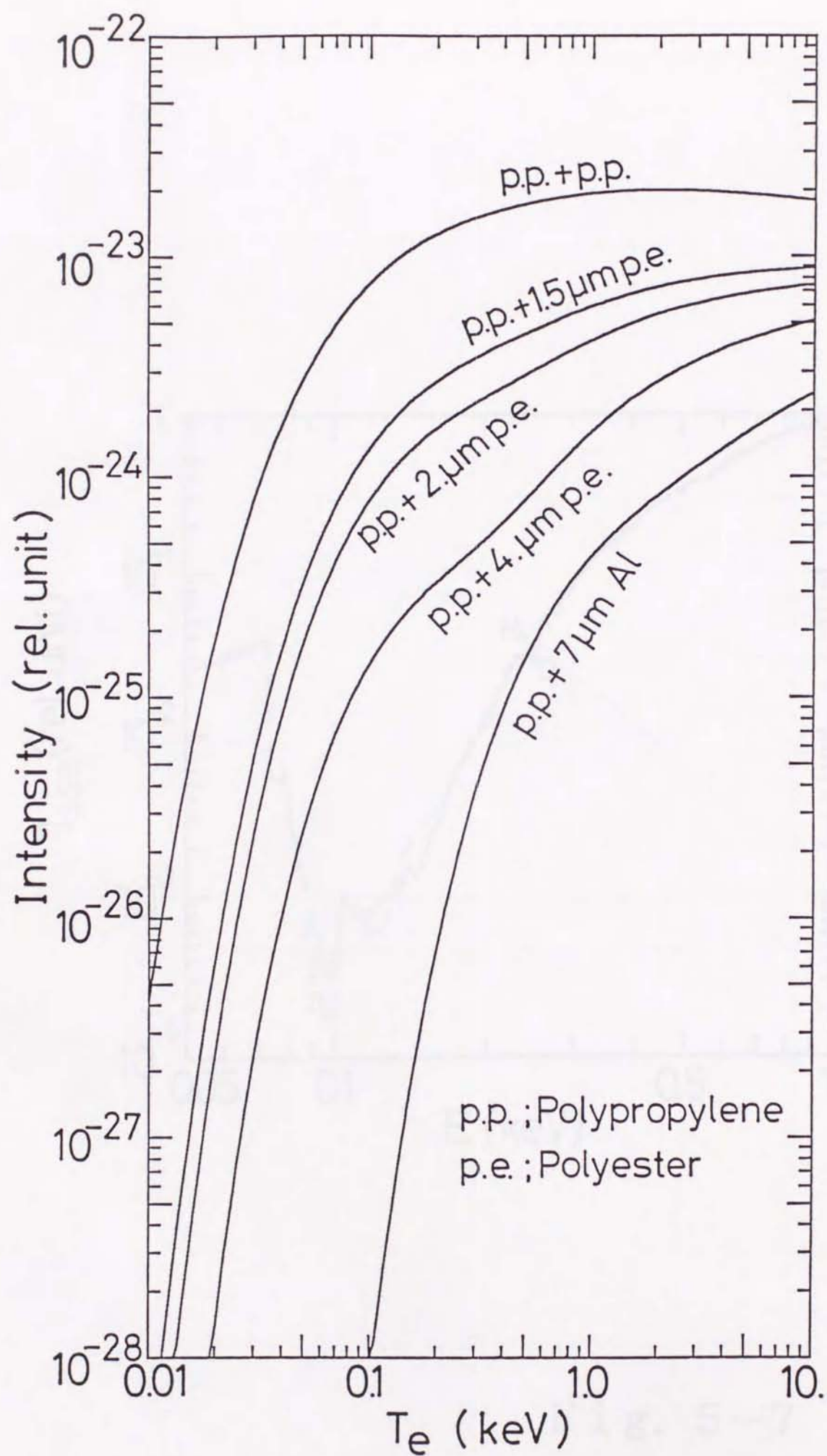


Fig. 5-6

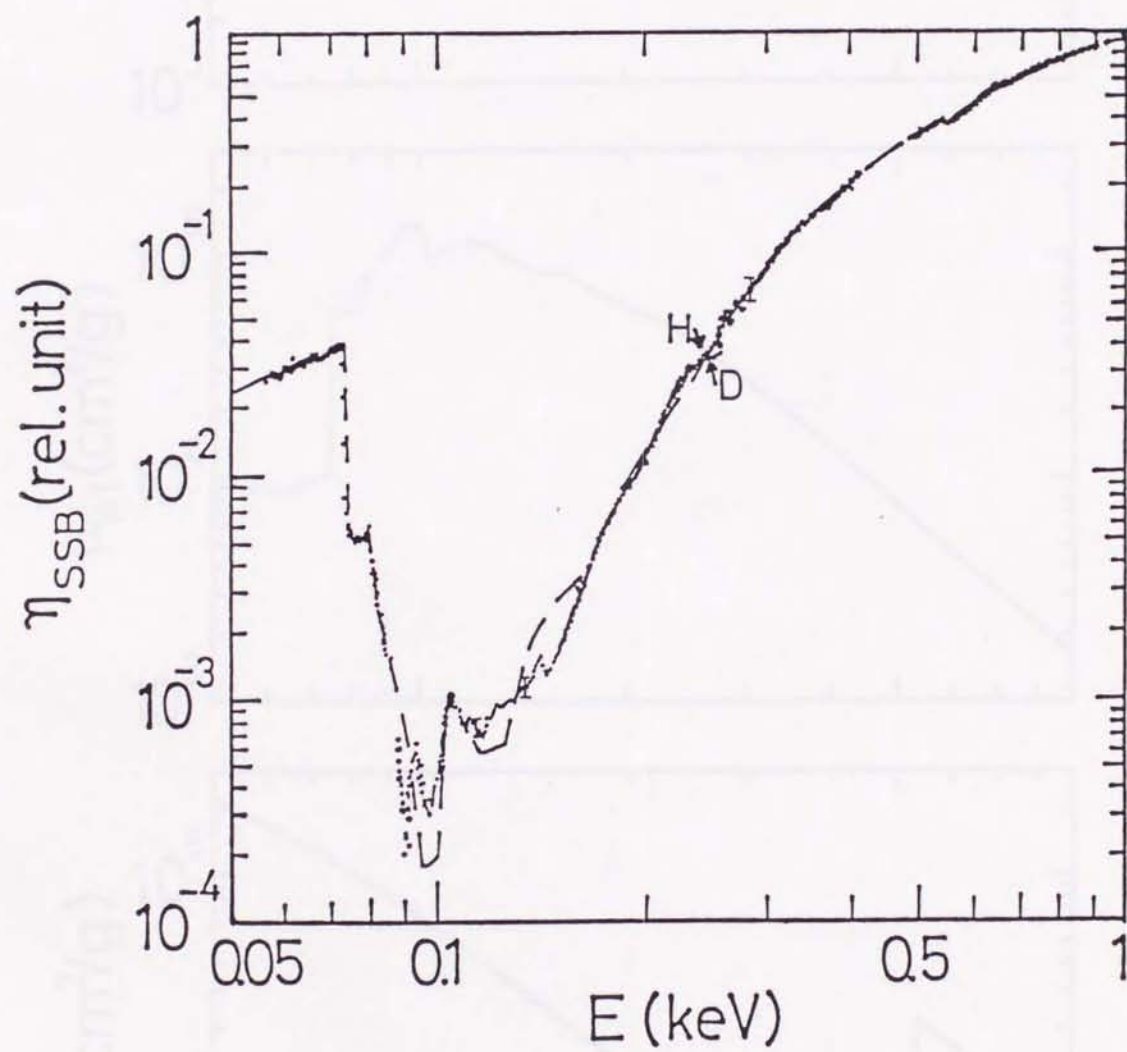


Fig. 5-7

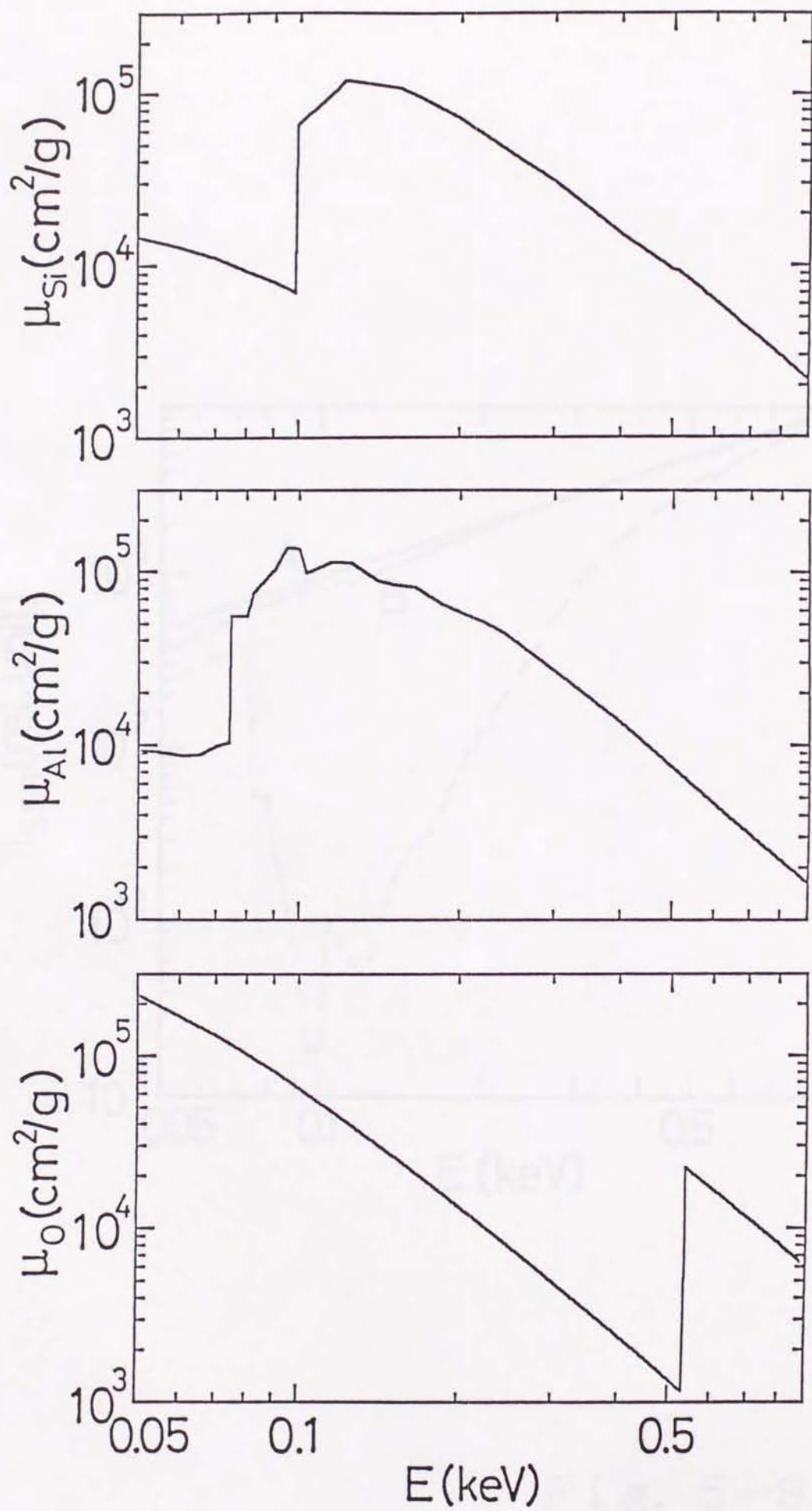


Fig. 5-8

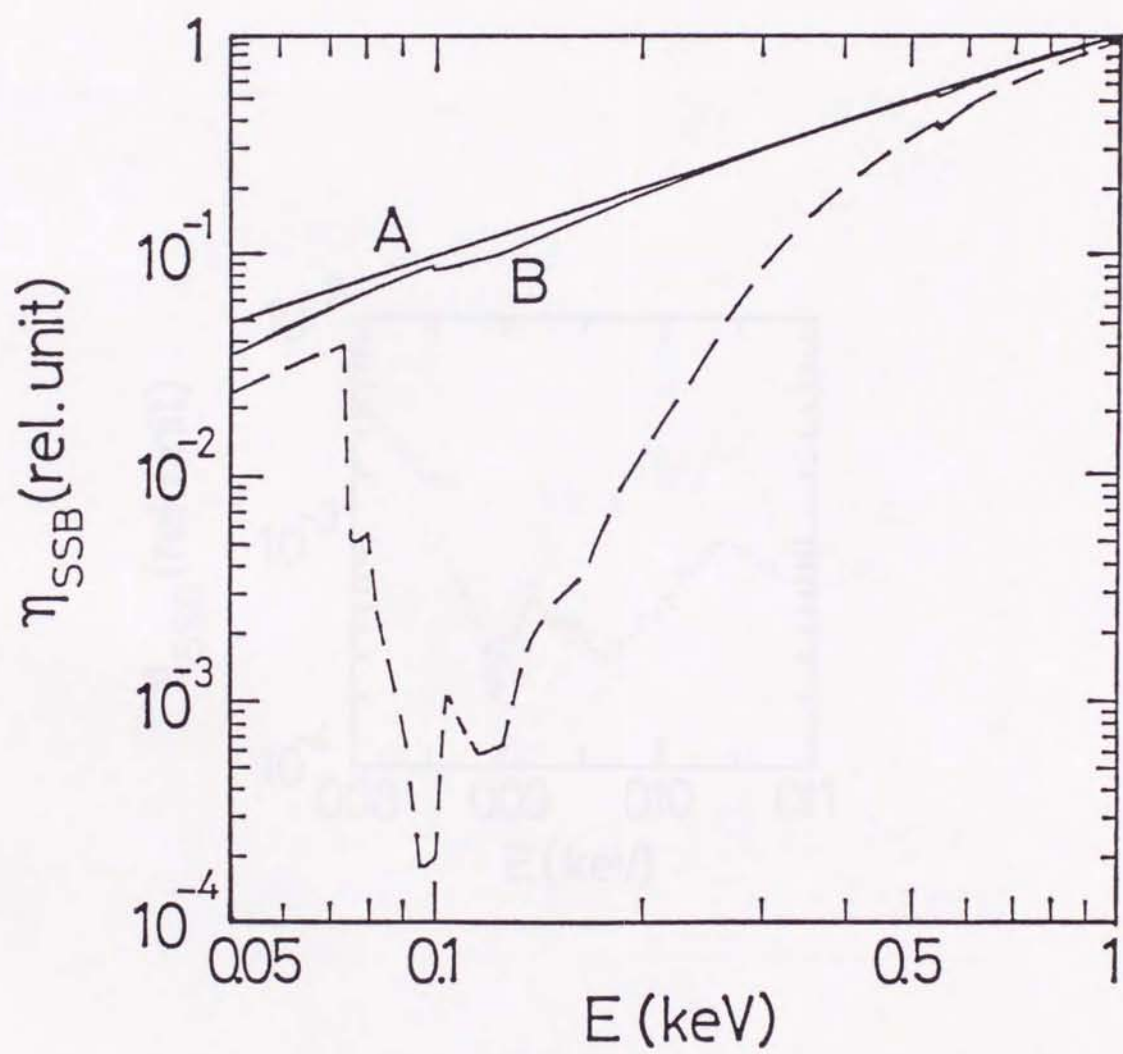


Fig. 5-9

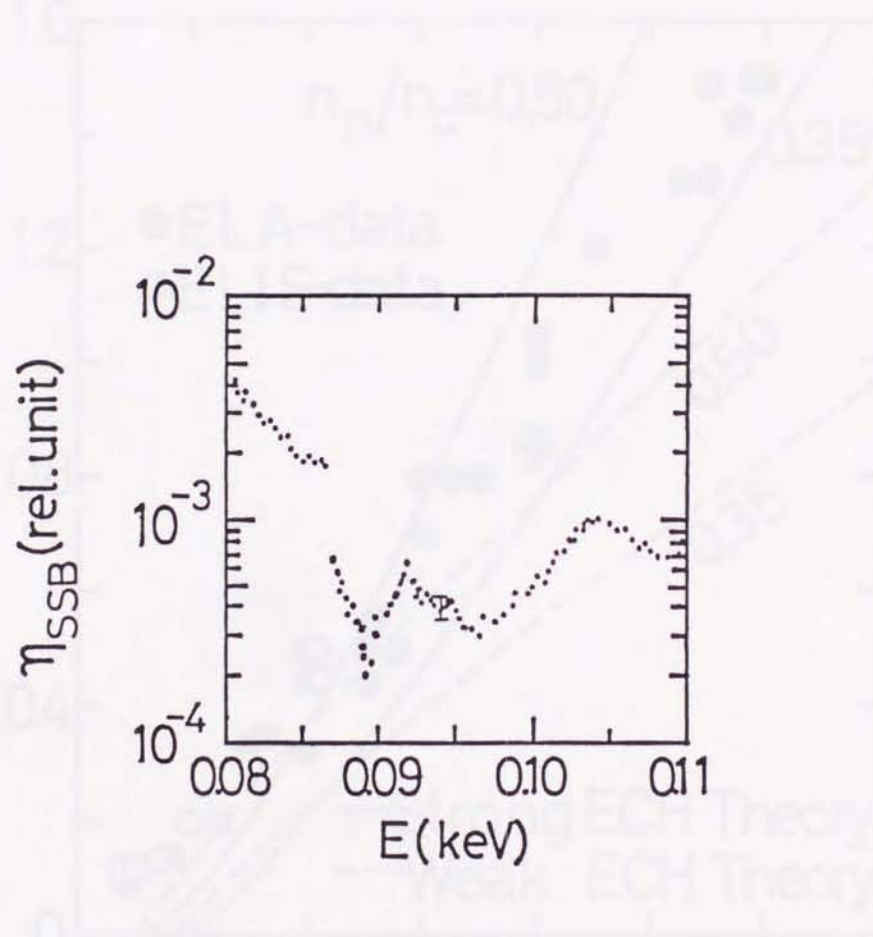
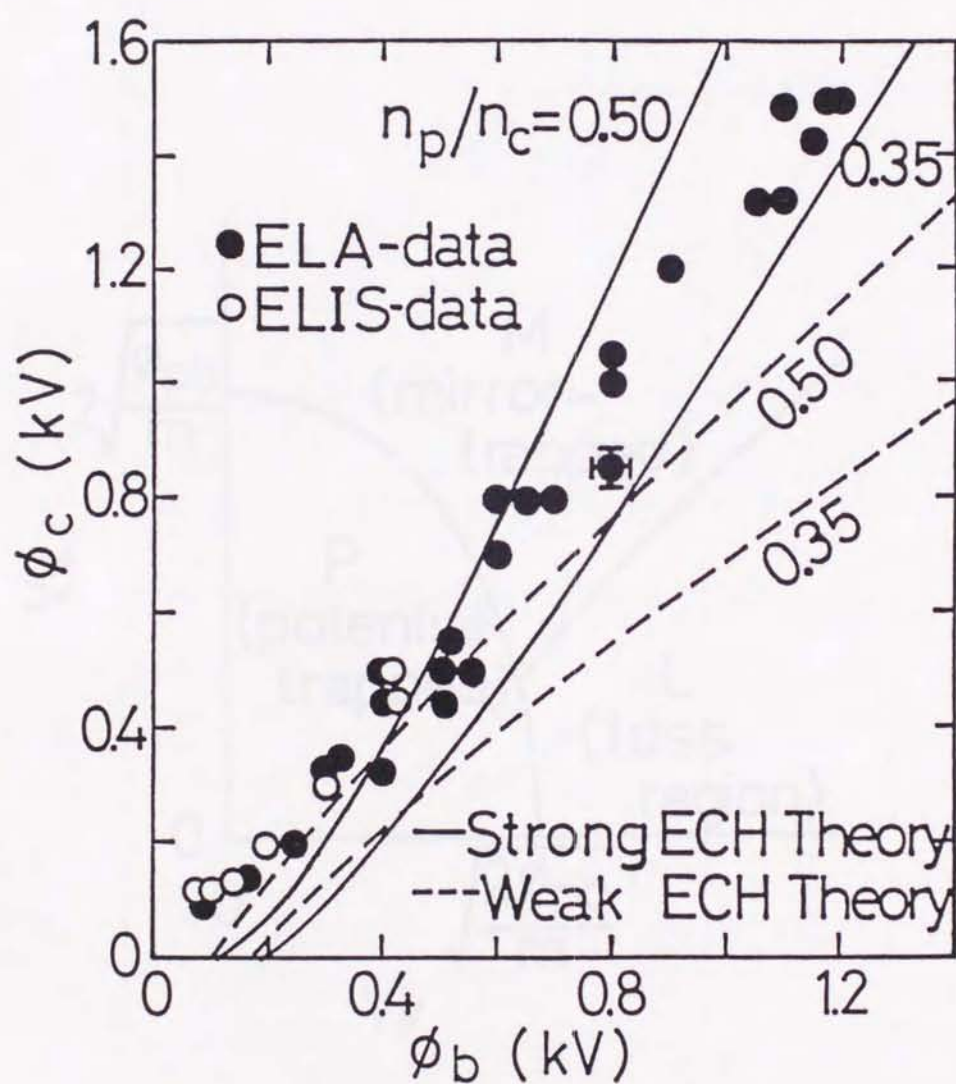


Fig. 5-10



Data from the ELA and
the beam-probe groups

Fig. 6-1

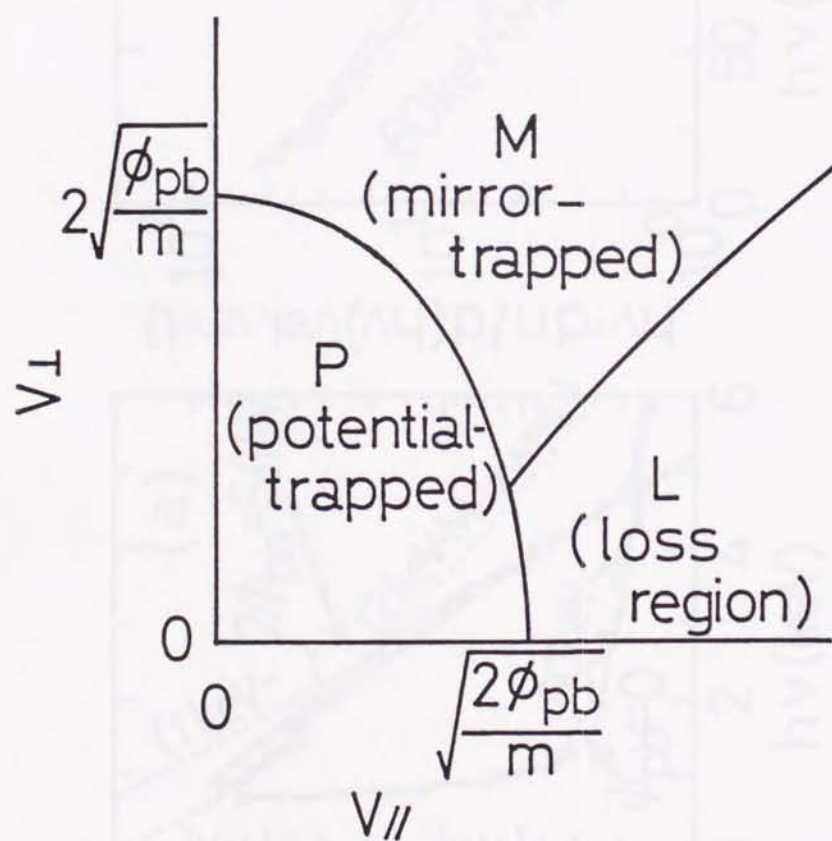


Fig. 6-2

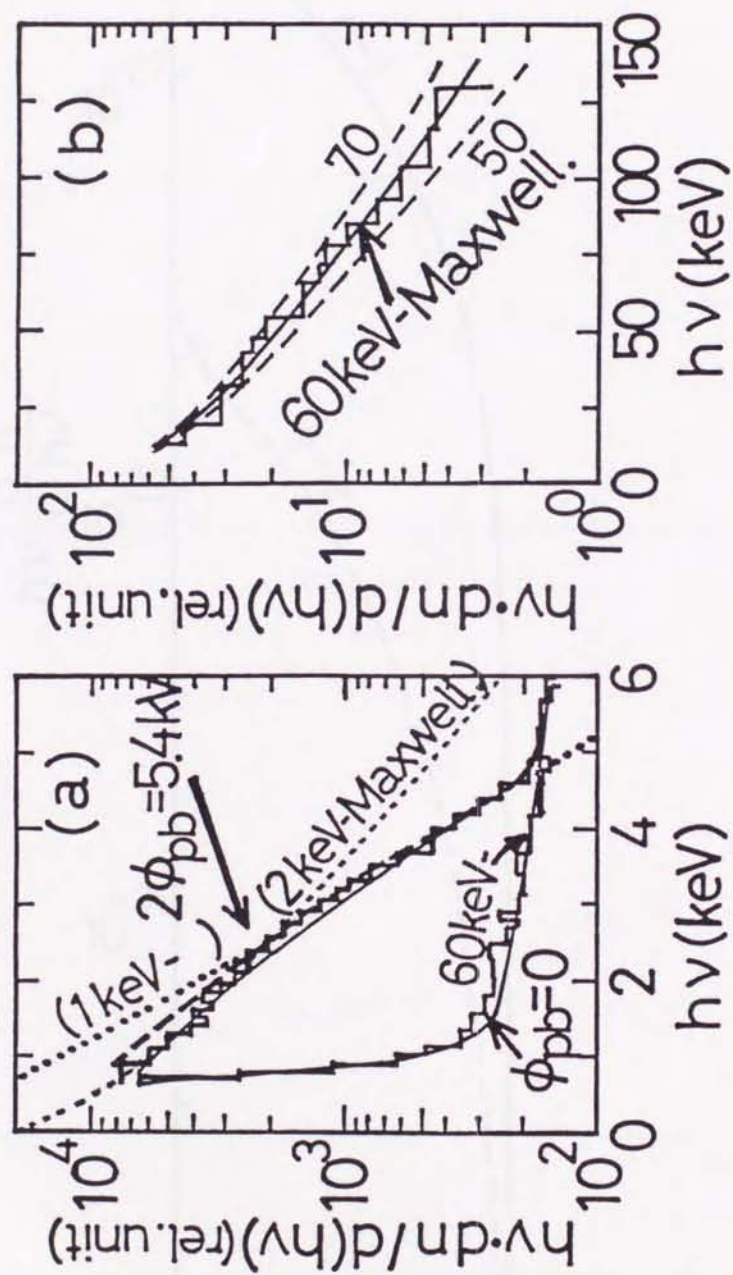


Fig. 6-3

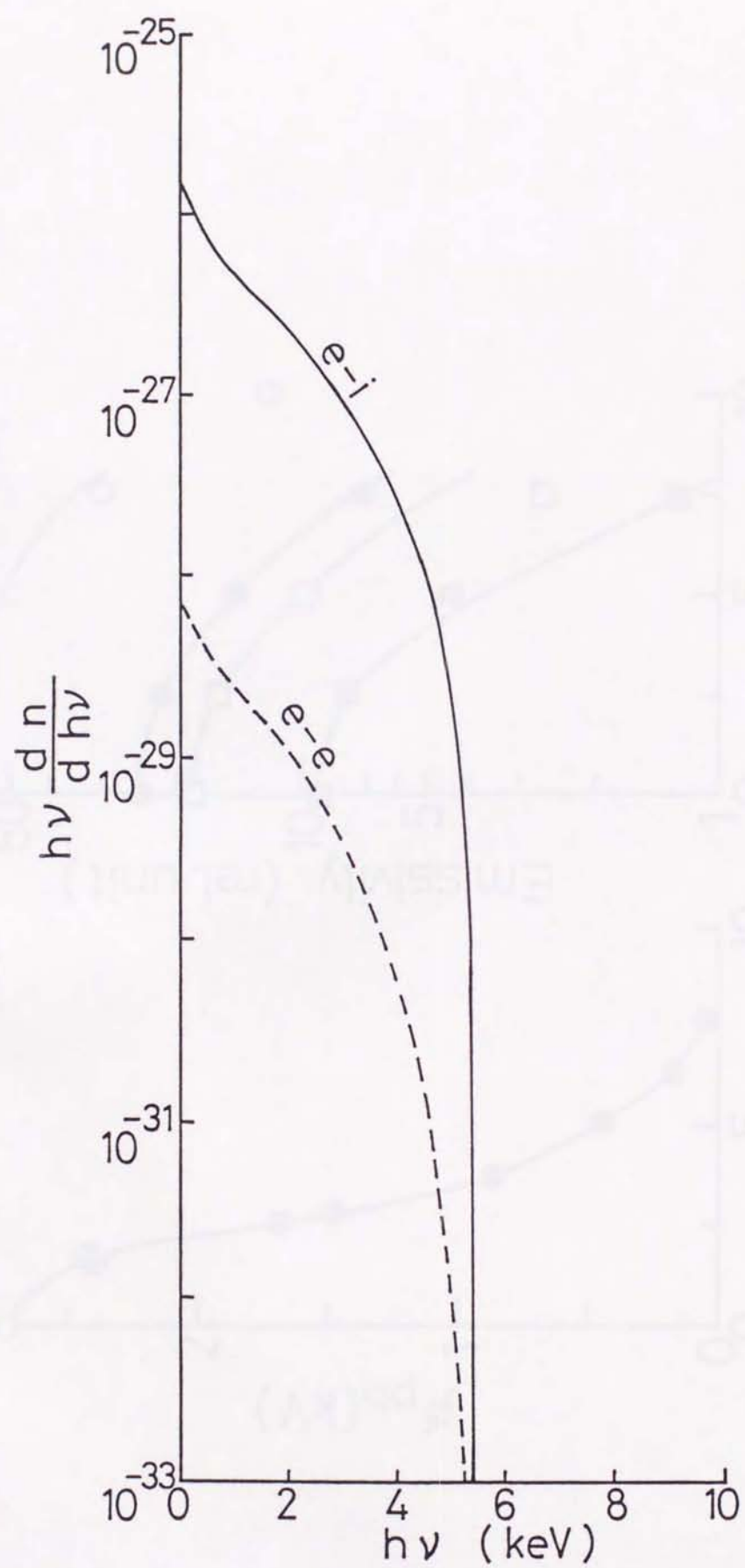


Fig. 6-4

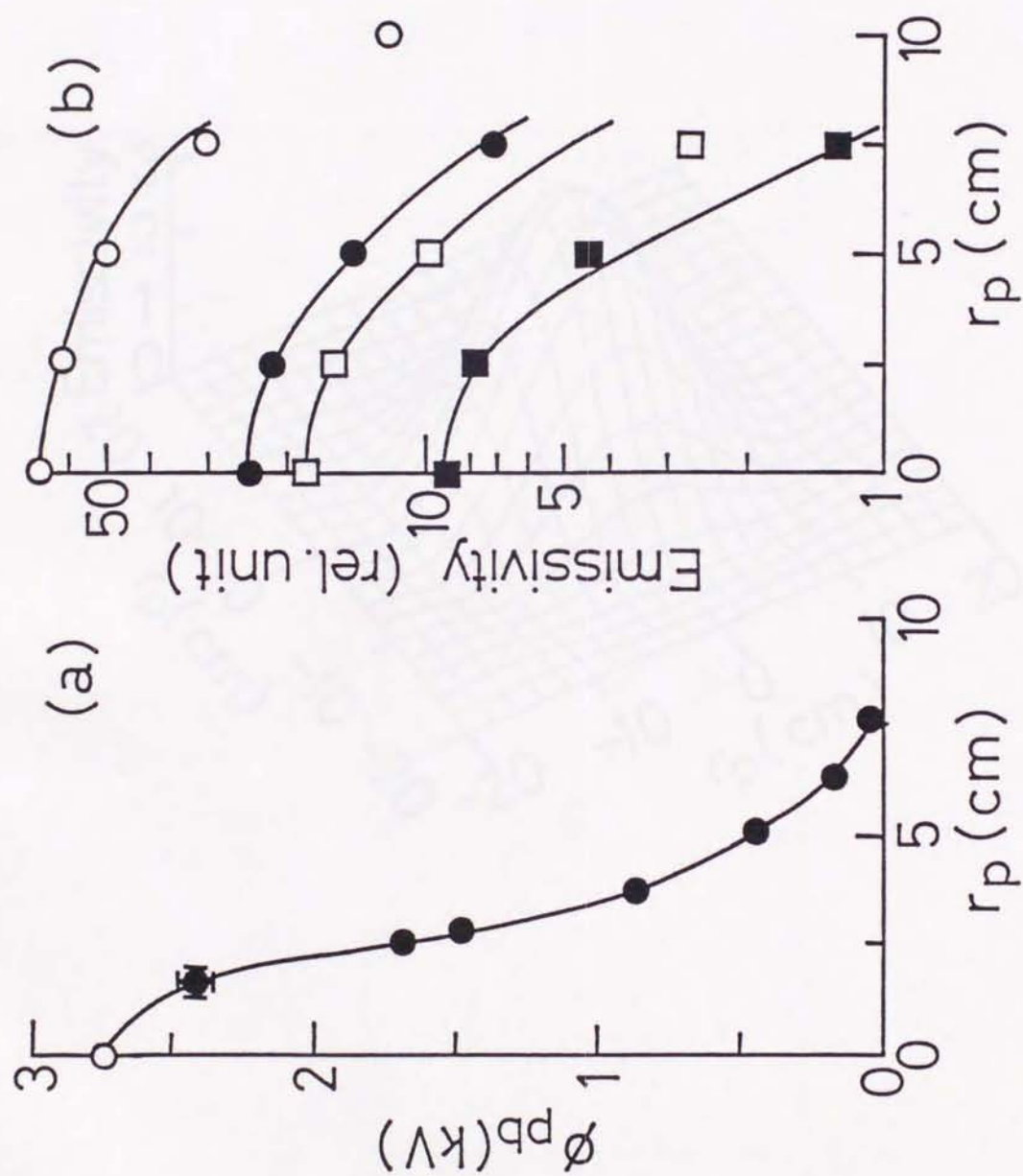


Fig. 6-5

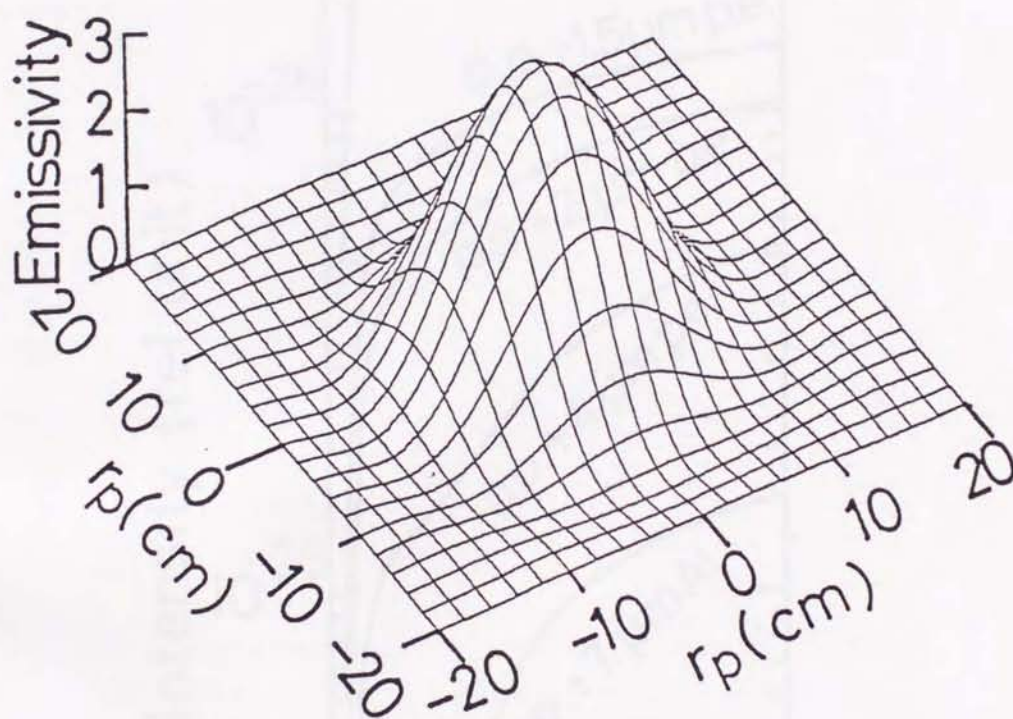


Fig. 6-6

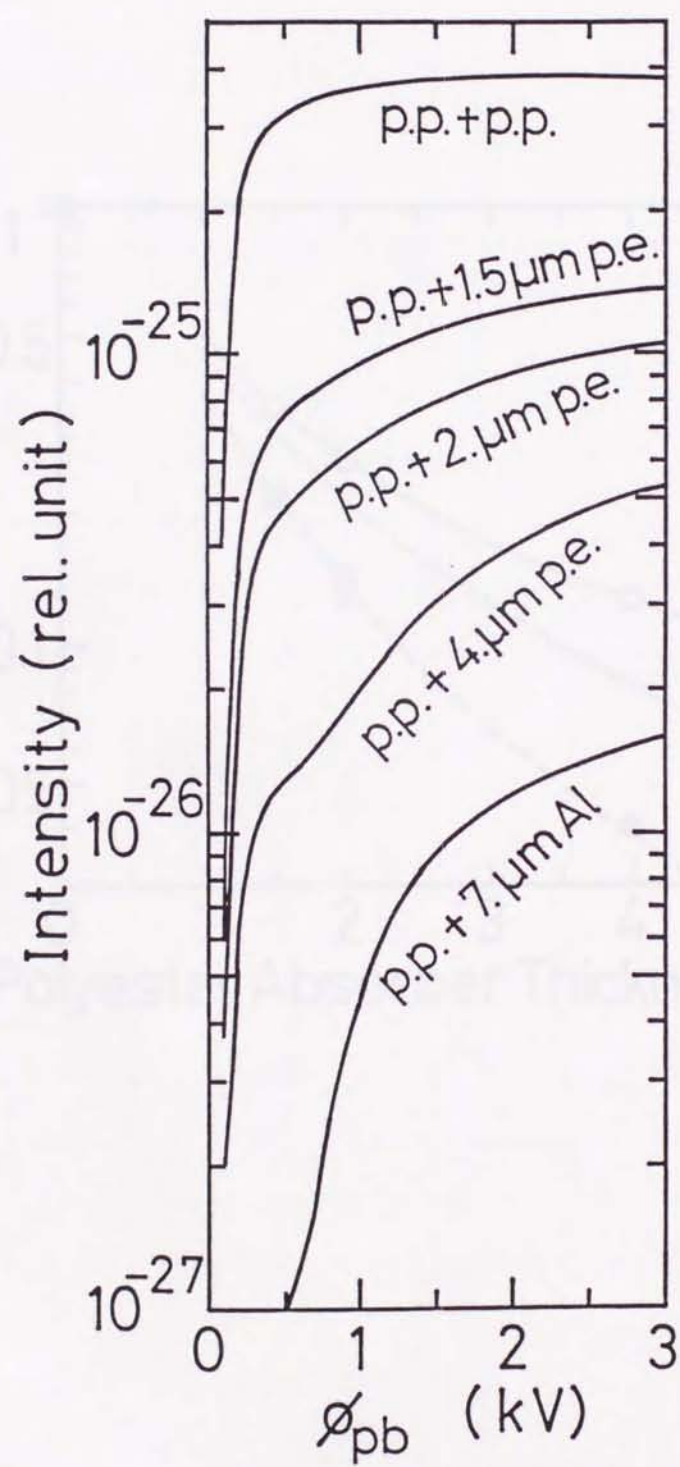


Fig. 6-7

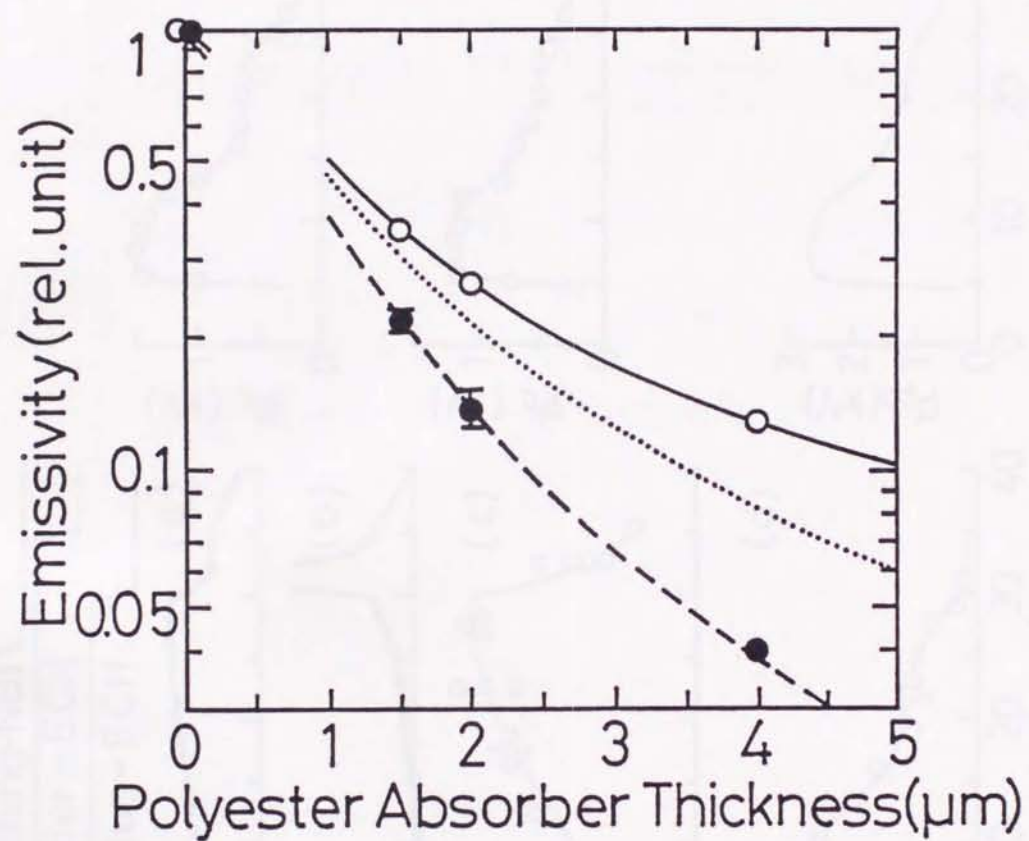


Fig. 6-8

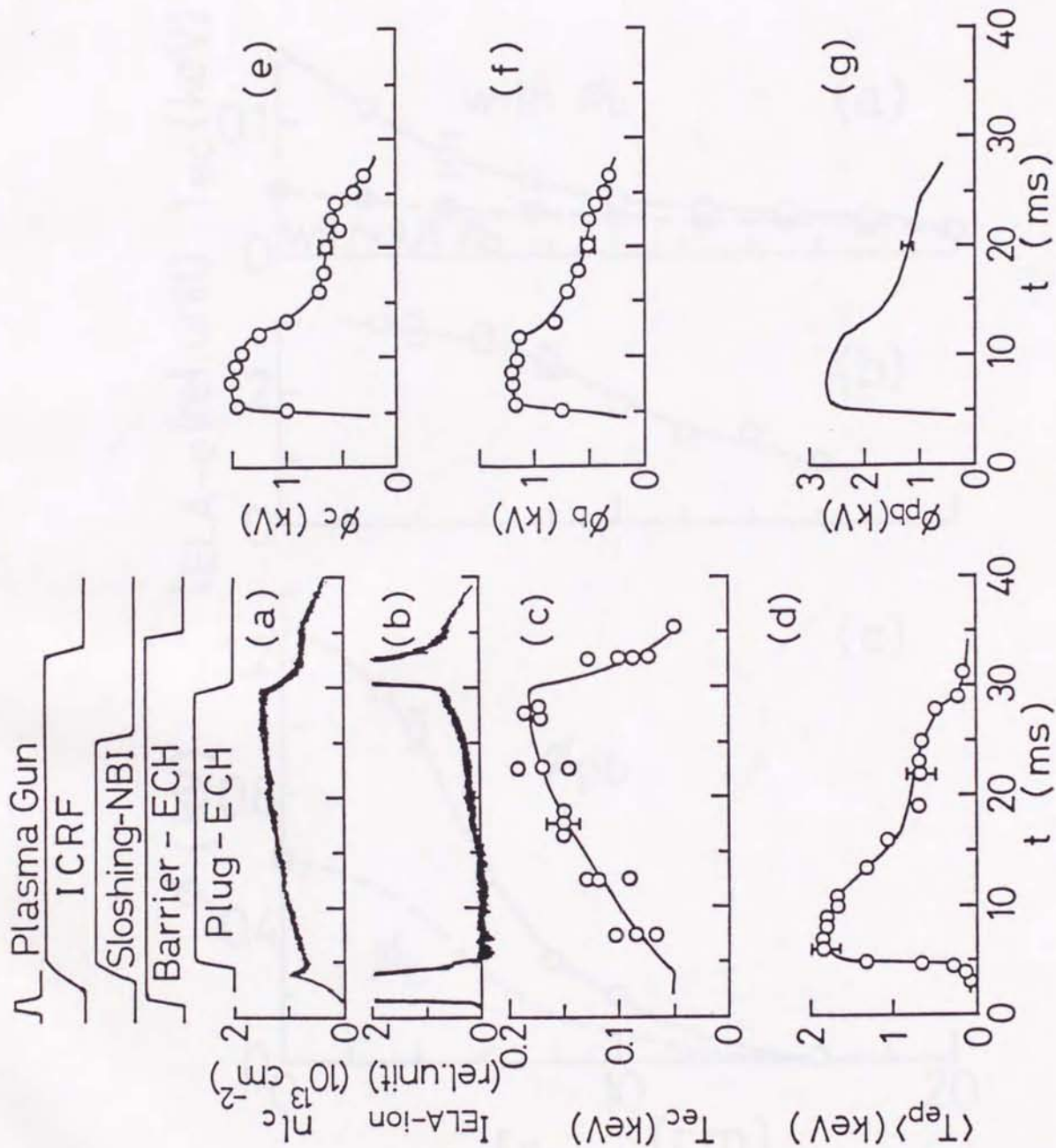


Fig. 6-9

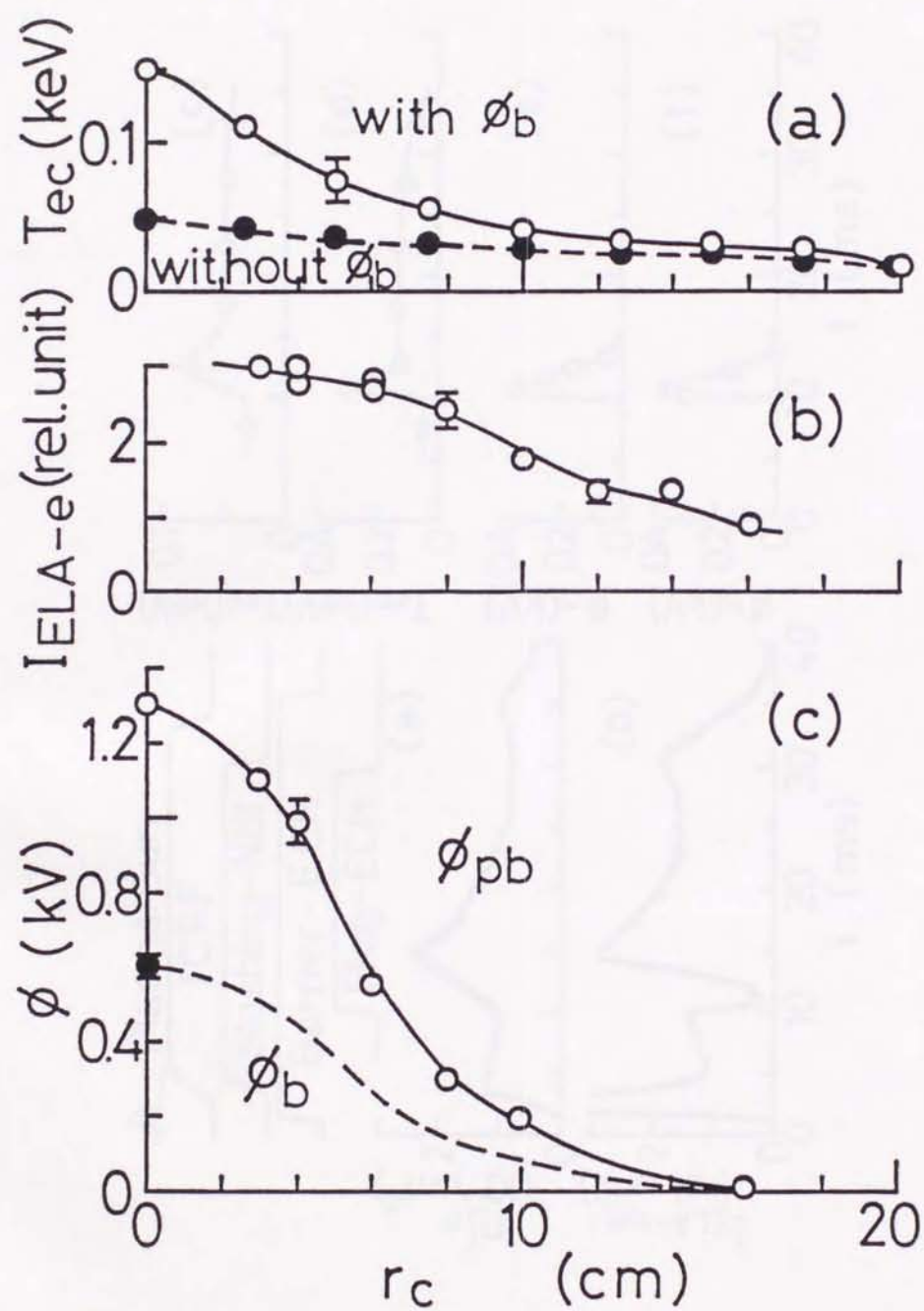


Fig. 6-10

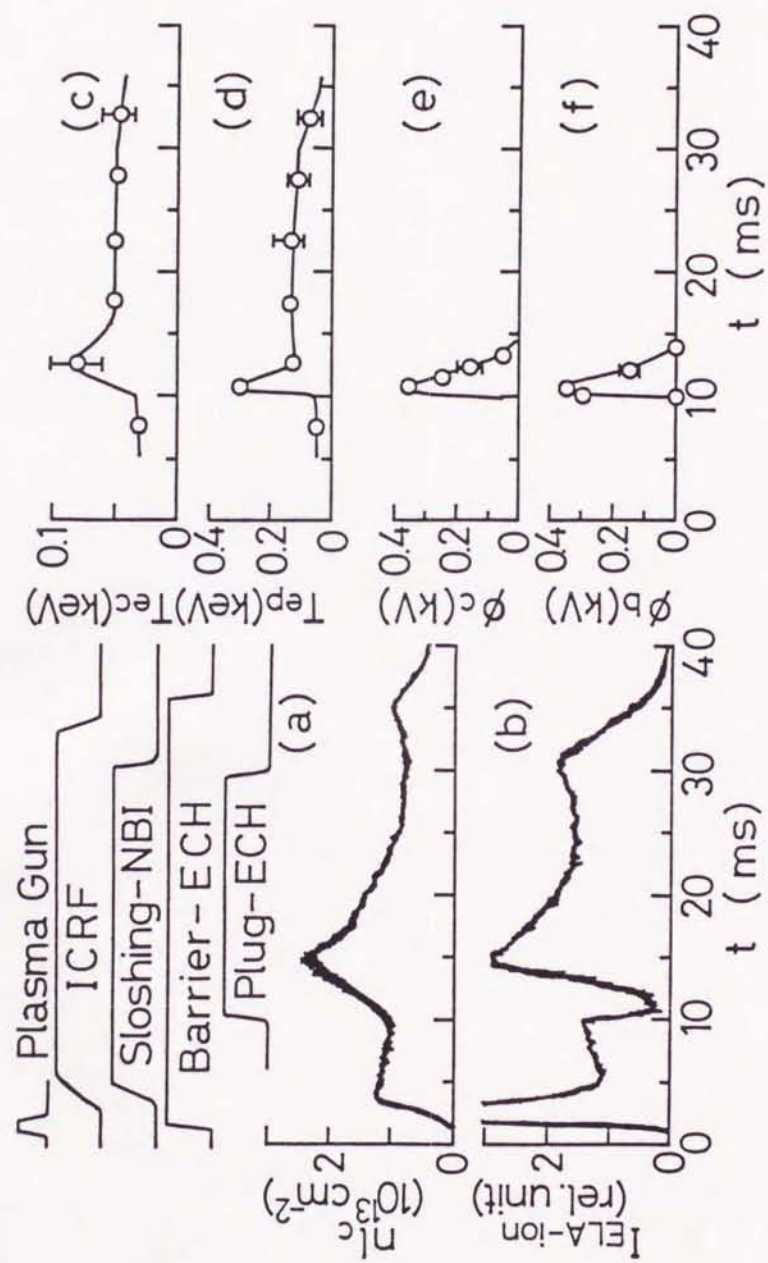


Fig. 6-11

